Czech Technical University in Prague
Faculty of Electrical Engineering
Department of Physics

High Density Plasma Experimental Diagnostics

Doctoral Thesis

Ing. Balzhima Cikhardtová

Prague, March 2019

Study Programme: Electrical Engineering and Information Technology (P 2612)

Branch of Study: Plasma Physics (1701V011)

Supervisor: prof. RNDr. Pavel Kubeš, CSc.

Acknowledgements

I would like to thank very much to my supervisor professor Pavel Kubeš for support, very extensive help and opportunity to participate in his project and internships in the Institute of Plasma Physics and Laser Microfusion in Warsaw. I want to express my deep appreciation to my colleage and husband Jakub Cikhardt from the hot plasma physics experimental group at the Department of Physics at the Faculty of Electrical Engineering CTU in Prague for his huge support to me.

My great gratitude goes to all members of the hot plasma physics experimental group at the Department of Physics at the Faculty of Electrical Engineering CTU in Prague, especially to Daniel Klír for valuable advices and opportunity of experimental internship in Institute of High Current Electronics in Tomsk.

A special thanks also goes to Marian Paduch, Ewa Zielińska, and the whole PF-1000 team from the Institute of Plasma Physics and Laser Microfusion in Warsaw, for implementation of the 16-frame Mach–Zehnder interferometer and experiments on plasma focus PF-1000.

Last but not least, I would like to thank to Krzysztof Tomaszewski from ACS Laboratories, Warsaw, for implementation of the 4-frame MCP pinhole camera.

This work was supported by the GACR 19-02545S, MEYS LTAUSA17084, LTT 17015, 8JPL19014, CZ.02.1.01/0.0/0.0/16_019/0000778 and CTU SGS19/167OHK3/T3/13, Ministry of Education, Youth, and Sports of the Czech Republic No. LTT 17015, Ministry of Education, Youth, and Sports of the Czech Republic No. CZ.02.1.01/0.0/0.0/16_019/0000778.

Declaration

I hereby declare that I have completed this thesis independently and that I have listed all the literature and publications used.
I have no objection to usage of this work in compliance with the act §60 Zákon č. 121/2000Sb. (copyright law), and with the rights connected with the copyright act including the changes in the act.

In Prague on March 28, 2019 ....

Abstract

This doctoral thesis is devoted to the experimental research on the megaampere PF-1000 plasma focus at the Institute of Plasma Physics and Laser Microfusion in Warsaw. The plasma foci are pulsed-power high-current discharge devices in which the hot dense plasma is formed. The plasma focus discharge is compressed by the pinch effect. In the pinched plasma an acceleration of charged particles to relatively high energies occurs. Using deuterium as the working gas, DD nuclear fusion reactions are achieved and intensive neutron pulses are emitted. Notwithstanding that the plasma focus research began in the 1960s, many fundamental principles of the particle acceleration have not been fully explained. The modern diagnostics methods with a high spatial and temporal resolution could help with the explanation of these principles and shift the knowledge in the hot dense plasma physics.

In this thesis, results from the experiments with novel configurations of the electrode system (anode gas-puff and anode cone) are presented. In this experiments, the plasma probing by 16-frame optical interferometer, 4-frame fast soft x-ray microchannel plate camera, and hard x-ray and neutron diagnostics are used to evaluate the plasma dynamics, electron densities, and other plasma-characterizing parameters. At the shots with the anode gas-puff numerous organized long-lived plasma structures of a fiber or ball form are observed. Such plasma structures have not been observed earlier in the classical plasma focus experiments. As far as the experiments with the anode cone are concerned, using such an electrode configuration, an significant increase in the neutron yield was reached. By the experimental data, the general plasma characterizing parameters, which could help with a further theoretical considerations, are approximated.

Keywords: Plasma focus, plasma diagnostics, interferometric diagnostics

Abstrakt

Tato doktorská práce je věnována experimentálnímu výzkumu na megaampérovém plasmatickém fokusu PF-1000 v Institutu fyziky plazmatu a laserové mikrosyntézy ve Varšavě. Plasmatické fokusy jsou impulsní silnoproudá výbojová zařízení, ve kterých dochází ke vzniku horkého hustého plazmatu. V plazmatickém fokusu je využíváno pinčového jevu, který silově působí na výboj a stlačuje ho. Ve stlačeném plazmatu dochází k urychlování nabitých částic na poměrně vysoké energie. Pokud je jako pracovní plyn použito deuterium, nastávají v horkém hustém plazmatu DD jaderné fúzní reakce, které produkují intenzivní neutronové impulzy. Přestože výzkum plazmatických fokusů začal již v 60. létech 20. století, řada základních mechanizmů, které vedou k urychlování částic, není stále plně vysvětlena. Moderní diagnostické nástroje s vysokým prostorovým a časovým rozlišením mohou pomoci tyto mechanizmy vysvětlit a posunout poznání v oblasti fyziky horkého hustého plazmatu.

V této doktorské práce jsou prezentovány výsledky experimentů s novými konfiguracemi elektrod (anoda s plynovou tryskou – tzv. gas-puffem a anodovým kuželem). V těchto experimentech je dynamika plazmatu, elektronová hustota a další parametry charakterizující plazma studována pomocí 16-ti snímkového interferometru, 4-snímkové rychlé Roentgenové kamery s mikrokanálovou destičkou a scintilačních detektorů tvrdého Roentgenova záření a neutronů. Ve výstřelech s anodovým gas-puffem byly pozorovány četné kulové a vláknovité struktury s dlouhou dobou života, jaké nebyly dříve, při klasických experimentech, pozorovány. Co se týče experimentů s anodovým kuželem, ve srovnání s klasickou plochou anodou došlo k významnému navýšení neutronového zisku. Experimentální data umožnila určení obecných parametrů charakterizujících plazma, pro navazující teoretické úvahy.

Klíčová slova: Plazmatický fokus, diagnostika plazmatu, interferometrie

Contents

List of Figures

List of Tables

List of Abbreviations

Abbreviation	Meaning
AASC	Alameda Applied Sciences Corporation
AFRL	Air Force Research Laboratory
API	Associated Particle Imaging
CAS	Czech Academy of Sciences
CCD	Charge-Coupled Device
CEA	Commissariat à l'énergie atomique et aux énergies alternatives (Alternative Energies and Atomic Energy Commission)
CESTA	Centre d'études scientifiques et techniques d'Aquitaine (Center for scientific and technical study of Aquitaine)
CTU	Czech Technical University
DFW	Double Forged Wolfram (Tungsten)
ELM	Edge Localized Mode
ENEA	Italian National Agency for New Technologies, Energy and Sustainable Economic Development
EUV	Extreme Ultraviolet radiation
FWHM	Full Width at Half Maximum
FEE	Faculty of Electrical Engineering
FNSA	Fast Neutron Scattering Analysis
HXR	Hard X-Ray
ICTP	International Centre for Theoretical Physics
IFJ	Instytut Fizyki Jadrowej (Institute of Nuclear Physics)
IFP	Institute of Fluid Physics
IHCE	Institute of High Current Electronics

Abbreviation	Meaning
IPPLM	Institute of Plasma Physics and Laser Microfusion
ITER	International Thermonuclear Experimental Reactor
KI	Kurchatov Institute
KIPT	Kharkov Institute of Physics and Technology
LANL	Los Alamos National Laboratory
LPPL	Lawrenceville Plasma Physic Laboratory
MagLIF	Magnetized Liner Inertial Fusion
MCNP	Monte Carlo N-Particle transport code
MCP	Micro Channel Plate
MPS	Moscow Physical Society
NCBJ	Narodowe Centrum Badań Jadrowych (National Centre for Nuclear Research)
Nd:YLF	Neodymium-doped Yttrium Lithium Fluoride
NDSE	Neutron-Diagnosed Subcritical Experiment
NNSS	Nevada National Security Site
NRC	National Research Center
NRL	Naval Research Laboratories
NSC	National Science Center
NSTec	National Security Technologies
nToF	Neutron Time-of-Flight
PAN	Polish Academy of Sciences
PF	Plasma Focus
PFNA	Pulsed Fast Neuron Analysis
PFNTS	Pulsed Fast Neutron Transmission Spectroscopy
PFTNA	Pulsed Fast-Thermal Neutron Analysis
PINS	Portable Isotopic Neutron Spectroscopy
PMT	Photomultiplier Tube
PPPP	Center for Research and Applications in Plasma Physics and Pulsed Power
PTS	Primary Test Stand
QSPA	Quasi-Stationary Plasma Accelerator
SAC	Silver Activation Counter
SNM	Special Nuclear Material
SEM	Scanning Electron Microscopy
TNA	Thermal Nutron Analysis
FNA	Fast Neutron Analysis
ToF	Time-of-Flight

Chapter 1

Introduction

This doctoral thesis deals with the experimental fundamental research of plasma in megaampere-current discharges on plasma foci. Plasma foci are pulsed power devices in which the plasma is compressed by so called “pinch effect”. In dependence on the experimental settings, for such a plasma, a relatively high densities of $(10^{23} - 10^{27})$ m^{-3} and temperatures 100 eV$-$4 keV, are typical [1]. Therefore, this plasma is usually categorized as the hot dense plasma. As far as the lifetime of this hot dense plasma is concerned, it could vary from several ns, on fast devices, up to several µs, on long-pulse devices.

The plasma focus experiments are usually closely related to the fundamental plasma physics research, nuclear fusion research, laboratory astrophysics, development of neutron sources, and material engineering.

The experiments presented in this thesis are performed on the PF-1000 plasma focus device in the Institute of Plasma Physics and Laser Microfusion in Warsaw.

The PF-1000 device with the maximum load current of above 2 MA, maximum stored electrical energy of above 1 MJ, and rise-time of about 5 µs is currently the largest plasma focus device in the European Union and one of the largest plasma focus devices in the world.

1.1 Goals of Thesis

The main goal of this thesis is to characterize the dynamic hot dense plasma in the PF-1000 plasma focus experiments using 16-frame optical interferometer, 4-frame microchannel plate soft x-ray camera, and neutron and hard x-ray diagnostics. Using the interferometry and microchannel plate camera, it is possible to investigate the plasma structures and dynamics. The interferometry methods also allows the evaluation of the spatial distribution of electron density. Knowing the plasma dynamics and electron density distributions, it is possible to approximate various fundamental plasma characterizing parameters which could be used to further theoretical considerations and plasma scaling, for example in laboratory astrophysics.

In this thesis, the emphasis was put on the organized plasma structures, especially the ball-like structures which have been observed in the experiments with the dynamic gas injecting into the plasma focus, so called “gas-puff”.

1.2 Structure of Thesis

Structure of this thesis is as follows. The plasma focus device is introduced in chapter 2 Plasma focus devices. In this thesis, the brief history of plasma focus research, principle of plasma focus, and the state of the art and applications are presented.

In chapter 3 Apparatus and diagnostics we found the description of PF-1000 device and experimental diagnostics used in the experiments reported in this thesis. This chapter includes description and parameters of the pulsed power generator and electrode system of the PF-1000 device, description and arrangement of the scintillation detectors, silver activation neutron counters, microchannel plate camera, and optical interferometer.

In the following chapters, the individual experimental setups, results, and particular conclusions are presented. Chapter 4 Experiments with deuterium gas filling is devoted to the classical plasma focus experiments. Chapter 5 Experiments with central electrode gas-puff describes the plasma focus experiments with the dynamic gas injecting from the central anode. Chapter 6 Experiments with central electrode cone presents the recent experiments in which the central anode was extended by a cone placed in the z-axis.

The overall results summary and approximation of the general parameters of the plasma is discussed in chapter 7.

In the conclusions in chapter 8, we found recapitulation of the most interesting results, perspective of the pinched plasma research, and future prospects.

Authors personal contribution to the experiments is reported in appendix A, list of the author's papers and conference contributions is presented in appendix B and appendix C, respectively. Appendix D includes list of the author's internships with an active experimental contribution.

As far as the units are concerned, in this thesis the SI units are used. For practical reasons, in some equations, units with metric prefixes are considered e.g. cm, keV, etc. In all such cases the units are specified.

Chapter 2

Plasma Focus Devices

Plasma focus is a pulsed power device in which an electric discharge occurs in a gas. The gas pressure is typically tens or hundreds of pascals. Current of the discharge could achieve from tens of kA up to several MA at the maximum of the pulse. Such relatively high current generates a magnetic field which accelerates and compress the discharge plasma. The plasma could be compressed up to density on the order of 10^{25} m^{-3} and heated up to temperature on the order of keV [2]. In such a high-density and high-temperature plasma, electrons and ions are accelerated by various mechanisms. Such a plasma is a source of characteristic radiation in ultraviolet (UV) and soft x-ray (SXR) spectral region. At the same time, hard x-rays (HXR) are generated by interactions of the accelerated electrons with the electrode system and other hardware close to the discharge. Similarly, the accelerated ions could generate other kinds of radiation. For example interactions of accelerated deuterons with a deuterium plasma or deuterated solid target could lead to neutron emission by the $\mathrm{D(d,n)^3He}$ nuclear fusion reaction.

2.1 Brief History of Plasma Foci

Historically, the plasma foci are connected with the nuclear fusion research. In the late 1940s, it was founded, that in the deuterium discharges with current of about a hundred kiloamperes, the DD nuclear reactions occurs. It seemed that is possible to relatively easily achieve a thermonuclear source of energy using a pulsed power gas discharge device [3]. Therefore, in the 1950s, the high-current pulsed discharges were intensively investigated in many world-class laboratories, especially in USA and

USSR [3, 4]. In the early 1960s, Nikolai V. Filippov[1] in USSR and independently Joseph W. Mather in USA invented the plasma focus device [5, 6]. For illustration, photo of Nikolai V. Filippov with his plasma focus device is displayed in fig. 2.1. The plasma foci seemed to be more efficient source of the deuterium fusion (DD) neutrons than other pulsed discharge devices, therefore they were also promising candidate to the nuclear fusion source of energy[2]. During 1970s, many experiments on plasma foci with discharge currents above 1 MA were performed in Los Alamos National Laboratories in USA and in Limeil Laboratories in France [8, 9]. The DD neutron yield per single experimental shot Y_n was significantly increasing with the discharge current I. At the currents bellow 2 MA, the neutron yield scaling power

Figure 2.1: Nikolai Vasilievich Filippov with his plasma focus device in Kurchatov Institute of Atomic Energy, Moscow, Russia [7].

---

[1] To the invention of the plasma focus significantly contribute also Tatiana I. Filippova [5].

[2] Most of the DD reactions are not achieved by the thermonuclear processes but by beam-target mechanism [4].

law up to $Y_n \propto I^4$ was experimentally found [10]. Later, in 1980s, the experiments on PF-360 device in Swierk and Poseidon device in Stuttgart led to suspicion that at the higher currents, the neutron yield could be saturated [11, 12]. However, since at the currents 1-2 MA the neutron yields achieve relatively high values $10^{10} - 10^{11}$, they are very efficient and cheap pulsed neutron sources [9, 10, 11, 13, 14]. Currently, plasma foci found application in many research fields, for example, in fundamental plasma physics and nuclear fusion research [15, 16], laboratory astrophysics [17, 18], material research [19, 20], radiobiology [21], development of portable neutron sources [34] and many others [10]. The current state of the plasma focus research and applications are presented in the following section.

2.2 Plasma focus principle

The plasma foci are pulsed power dicharge devices with a current from several 10 kA to several MA. Such a high current is achieved using a capacitor bank or Marx generator (for example at the SPEED-2 or Hawk devices [27, 28]). The capacitor bank is more simple and most common type of plasma focus generator. In such a case, the generator is composed of high-voltage capacitors which are connected in parallel. Charging voltage ranges between 10-100 kV in dependence on the used capacitors and on the experimental setup. The electrical energy stored in the capacitor bank varies between few of kJ, at small desktop devices, and few of MJ at the large plasma focus facilities (for example 2.8 MJ at the PF-3 device [29]). To deliver the energy from the capacitors to the electrode system, where the gas discharge occurs, fast electrical switching (> 100kA/µs) must be used. Usually, the fast switching is achieved using gas spark-gaps. However, sometimes we can meet solid-state switching using tyristors or other semiconductor switching elements [8, 9, 23].

As far as the electrode system is concerned, it is composed by an inner cylindrical electrode (usually anode) and several cathode rods placed on a circle which is concentric with the cathode, see fig. 2.2. The electrode system is usually made of copper or stainless steel, but we can meet also tungsten electrodes or beryllium electrodes [16]. In fig. 2.2 we can see two designs of plasma focus which are different in a ratio of diameter and length of the electrode system. These two designs are named by their inventors: Mather-type (fig. 2.2(a)) and Filippov-type (fig. 2.2(b)). In the case of the Mather-type, the ratio is usually bellow 0.25 and an inner electrode diameter is between 2 – 22 cm [13]. In the case of the Filippov-type, the ratio is greater than 5 and the diameter of the inner electrode is typically between 50 – 250 cm [13]. We note, that the Mather type is the more common case of the plasma focus.

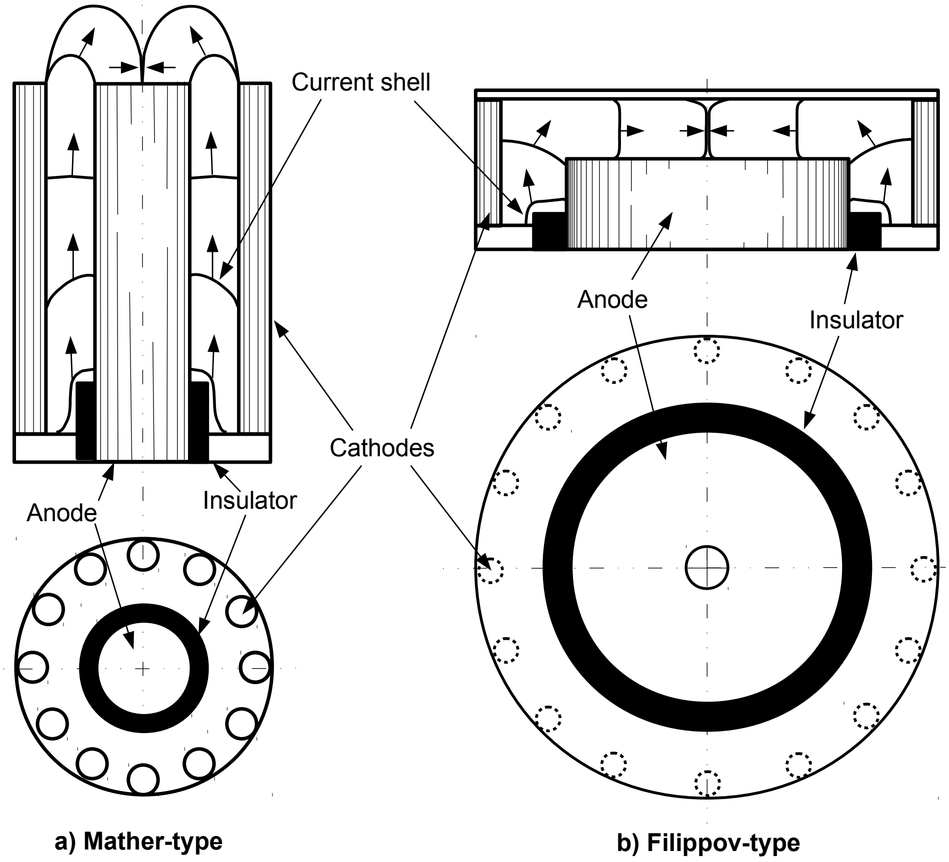

Figure 2.2: Plasma focus electrode systems: (a) Mather-type, (b) Filippov-type [22]

In the both types of plasma plasma focus, the anode and cathode are separated by an cylindrical insulator which is usually made of Al_2O_3 or borosilicate glass [2, 13]. Whole electrode system is placed in the vacuum chamber. In the vacuum chamber is reached a high vacuum (usually of about 10^{-3} Pa) to avoid influence of air residues on the discharge. After that, the vacuum chamber is filled by a working gas, for example hydrogen, deuterium, neon, etc. A pressure of the gas is usually on the order of $(10^1 - 10^2)$ Pa.

The plasma focus discharge could be divided into several phases.

I. Breakdown phase

The discharge begin after the trigger of the capacitor battery switching. If the initial gas pressure is optimized in accordance with the Pashen law, applying the voltage pulse between the anode and cathode, the sliding discharge is developed along the cylindrical insulator [13]. After some time (50-500) ns, the conductance of the sliding discharge becomes high enough for the discharge to convert into a plasma sheath [13].

II. Axial acceleration phase

The discharge current is growing and formed plasma sheath is accelerated by the Ampere force in axial direction towards to the end of the electrode system. During the propagation, the plasma sheath, as a “magnetic piston”, sweeps the working gas and increase its mass. Dynamics of the plasma sheath can be described by the two-dimensional snowplough model [2, 30]. A duration of the plasma sheath propagation from the beginning to the end of the electrode system is usually a few μs. However, we can meet also fast plasma foci, like SPEED-2, with radial acceleration time below 400 ns [25]. A velocity of the accelerated plasma sheath reaches $(10^4 - 10^5)$ m/s in the case of Mather-type [2]. We should note that the plasma sheath is not a thin and dense plasma, but rather relatively broad and diffuse structure [13].

III. Radial acceleration phase

When the plasma sheath exceed the end of the electrode system (see fig. 2.2), an umbrella-shaped structure is formed above the anode. For better clarity, the experimental image of such a plasma umbrella-shaped structure is displayed in fig. 2.3.

The current flowing from the anode generates a magnetic field. Consequently, the plasma sheath is accelerated by the Ampere force and an implosion occurs. The force acting on the plasma element of length d$\mathbf{l}$ is

$$\mathrm{d}\mathbf{F} = I\mathrm{d}\mathbf{l} \times \mathbf{B}, \tag{2.1}$$

where $\mathbf{B}$ is the magnetic field. This compression is called “pinch effect”. The situation is displayed in fig. 2.4. The implosion velocity is typically on the order

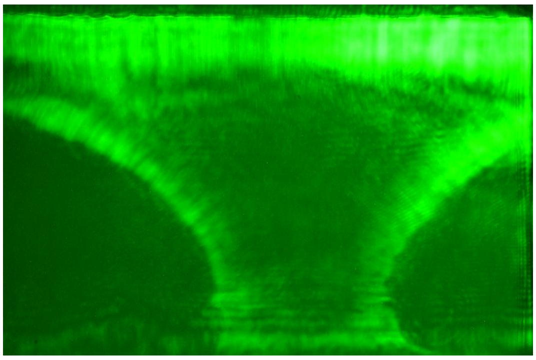

Figure 2.3: Schlieren image of the umbrella-shaped plasma during the radial implosion at the shot on the PFZ-200 [Author's experimental data].

of 10^5 m/s. The dimensions of the plasma focus electrodes should be designed so that the discharge current is near the maximum when the plasma sheath reaches maximum of the implosion.

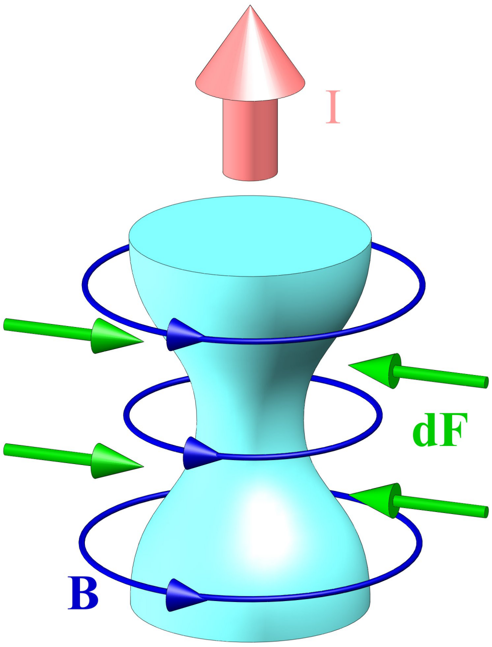

Figure 2.4: The pinch effect.

IV. Stagnation phase

The stagnation phase is the most interesting phase of the plasma focus discharge. This is the final phase of the plasma implosion, when a radius of the plasma column is close to the plasma focus z-axis. An universal radius of the imploded plasma which defines the stagnation phase does not exist. The minimum radius to which the plasma could be compressed is $(1-10)$ mm and a length of the pinched plasma (pinch) is typically $(1-10)$ cm. Both the discharge minimum radius and the length are dependent on the working gas nature, pressure, current, rise time, dimensions of the electrode system etc. As far as the plasma temperature and density are concerned, they reaches up to the order of keV and 10^{25} m^{-3}, respectively [2, 13]. A duration of this phase is typically on the order of ns or tens of ns.

Such a plasma could be an efficient source of soft x-ray pulses[3]. The SXRs are dominantly produced by a line and recombination radiation. For example, in a case of plasma focus neon discharge, the efficiency of conversion of electrical energy into characteristic SXRs is on the order of percents [32]. Obviously, in the case of hydrogen or deuterium, the SXRs are produced only by bremsstrahlung and the SXR yield is much lower than in the case of heavier gases.

In the stagnation phase, a very important role play instabilities. We distinguish between symmetric (m=0) and asymmetric (m=1) instabilities[4]. The asymmetric instabilities (also called kink instabilities) are undesirable. The significant symmetric instabilities are usually associated with a “bad shot” due to, for example, inhomogeneous insulator breakdown, impure or damaged insulator, impure or damaged electrode system, inhomogeneous electric energy distribution from the pulsed power generator, etc. In contrast, the symmetric instabilities (also called sausage instability) accompany every plasma focus discharge and if the discharge is not stabilized by an external magnetic filed, the symmetrical instabilities lead to the disruption of the pinch. During the pinch disruption a high electric field is generated and charged particle acceleration up to energies on the order of hundreds of keV occurs. We note that the detail principles of charged particle acceleration during the instability disruptions are still not explained.

---

[3] In accordance with the classification in [33], we consider soft x-rays (SXR) as photons with energy (0.5-10) keV. However, in some literature a different energy range of SXRs could be found.

[4] The instability mode m represents a dimensionless parameter in the Kruskal-Shafranov Stability limit [31].

The accelerated electrons which strike anode or some other metal causes emission of bremsstrahlung. A photon energy of the bremsstrahlung could exceeds 0.5 MeV [2, 13].

As far as the accelerated ions are concerned, in deuterium plasma, collisions of accelerated deuterons could lead to the deuterium-deuterium (DD) nuclear fusion reactions [6]. In such a case, two reactions with almost the same probability occur: D(d,n)^{3}He ($E_r \doteq 3.27$ MeV) reaction accompanied by neutron emission and D(d,p)T ($E_r \doteq 4.03$ MeV) reaction leading to proton emission. The released energy is divided between the formed nucleon and ejectile particle (2.45 MeV to neutron and 3.02 MeV to proton). We note that in the laboratory system, the ejectile particle energy is depended on the angle of emission and on the projectile particle energy.

The radiation and particle emission and other features of the plasma during the stagnation phase are the main subject of many plasma focus experiment. The state of the art and plasma focus research and applications are presented in the next section.

The physics of the pinched plasma and stagnation phase is precisely described in [38, 39, 40].

2.3 State of the Art and Applications

The plasma foci are experimental devices and it is still impossible to found any plasma focus as a commercial product. However, some of the possible applications seems to be promising. At the same time the plasma focus fundamental research without commercial application is also very important and interesting. In this section, selected plasma focus experiments and applications are presented.

2.3.1 Material Research

Currently, the very often application of plasma foci is the material research. In the modern technologies, a materials which withstand an extreme plasma and radiation exposure are necessary. The typical representative of such technologies is development of plasma-facing materials for tokamaks and stellarators, especially for international projects ITER, Wendelstein 7-X, etc. In such a research, the plasma focus could be used as a source of plasma, fast electrons, or fast ions for testing of material samples. We can mention a few interesting examples.

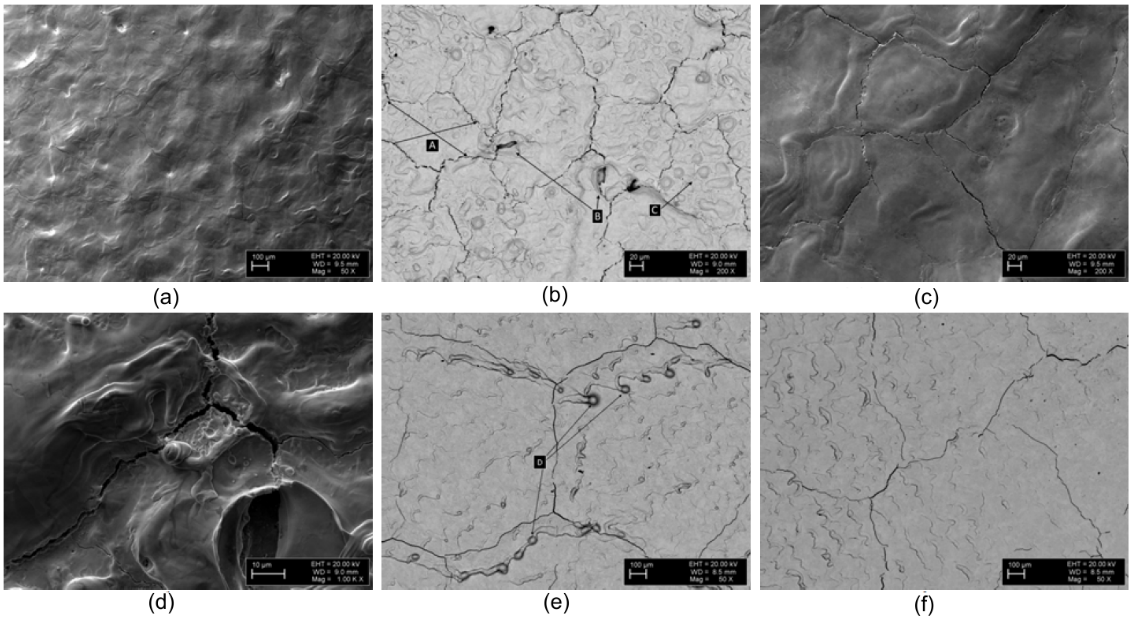

Figure 2.5: Scanning electron microscope images of irradiated double forged tungsten (DFW) samples. (a, b, c, and d) samples irradiated by 100 pulses on the PF-12 device, (e) sample irradiated by 4 pulses on the PF-1000 device, and (f) sample irradiated by 2 pulses on the PF-1000 device. [41].

In cooperation of the Czech Academy of Sciences (CAS) and Institute of Plasma Physics and Laser Microfusion (IPPLM) in Warsaw, the compact high-repetitive PF-6 (6 kJ, 0.4 MA) with shot rate up to 10 Hz [37] and large single-shot PF-1000 (1 MJ, 2 MA) devices were used for irradiation of dispersion strengthened (DS) tungsten materials. In paper [20], Vilemova present testing one of the most relevant candidates for tokamak first wall materials W-1%Y_2O_3 and W-2.5%TiC prepared by consolidation of powders with size of about 1 μm. The samples were placed in the distance of 8 cm from the plasma focus electrode system where a power flux is of about 10^7 W/cm^2 with duration of about 10 ns. Consequently, structural changes of the tested samples are investigated by scanning electron microscopy (SEM). More in [20, 35, 36].

Similarly, in the work presented in papers [19, 41], the double forged tungsten (DFW) is tested by plasma exposure on PF-1000 at IPPLM, PF-12 device at the Tallinn University (see fig. 2.5 [41]), and QSPA-50Kh device at the Institute of

Plasma Physics of National Science Center Kharkov Institute of Physics and Technology (NSC KIPT).

As far as the Kh-50 device is concerned, it is so called quasistationary plasma accelerator (QSPA). The QSPAs are similar to plasma foci, they are also based on the coaxial electrode system. In contrast to common plasma foci, the electrode system of the QSPAs are specially shaped and equipped by needle-type emitters of electrons to achieve efficient quasistationar flow of high-temperature plasma (see fig. 2.6) [76, 77, 78]. Another significant difference between QSPAa and plasma foci is the pulse duration. The typical pulse duration of the QSPAs is by two or more orders of magnitude higher than in the case of plasma foci, to ensure quasistationarity of the produced plasma. The pulse duration of the Kh-50 device is of about 500 μs. A maximum current of the pulse reaches approximately 0.7 MA. Due to the long pulse duration and relatively high current, the electrical energy stored in the capacitor bank achieves fairly high value of 4 MJ.

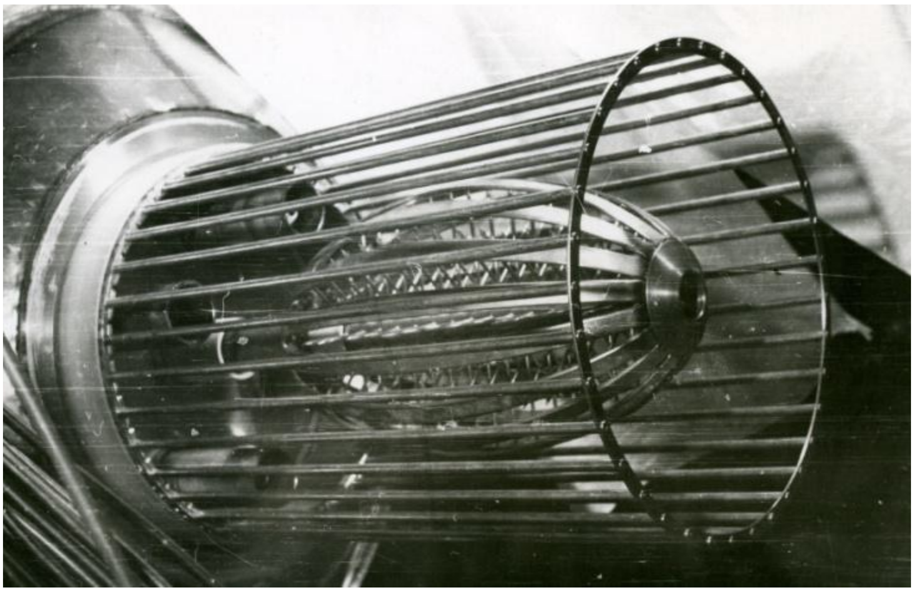

Figure 2.6: A photography of the electrode system of the quasistationary plasma accelerator (QSPA) [77].

As far as the material study at KIPT is concerned, the plasma–surface interaction effects during various transient events (e.g., disruptions, Vertical displacement events (VDEs), edge localized modes (ELMs)) connected with the nuclear fusion research are studied also on the new QSPA-M device (0.6 MA, 250 μF, 1.4 MJ) [79, 80].

The plasma foci and devices based on the plasma focus found application not only in material testing, but also in thin film deposition, for example TiO_2 [81], carbon film [82], tungsten nitride [83], iron [84], etc. Typically, for the material layer deposition, plasma foci with shot repetition frequency on the order of Hz or tens of Hz are used. Such plasma foci are usually much smaller than the single shot devices. Their electrical energy stored in the capacitor banks is on the order of kJ and current achieves several tens of kA or hundreds of kA.

A more detailed description of the plasmafocus application in the material research is beyond the scope of this thesis.

2.3.2 Neutron Sources

The fast neutron sources are necessary both in practical application and in laboratory research. As an example of practical application is a non-invasive detection of explosives, drugs and other low atomic number contraband using neutrons [85, 86, 87, 88]. The drugs and explosives typically contain low-atomic number elements as H, C, N, 0, P, S, and Cl. An interaction probability of x-rays, which are commonly used for contraband inspections, with low-atomic number elements is low [85]. It leads to development of many neutron-based contraband detection techniques [85, 86, 88]. For example, Thermal neutron analysis (TNA), Fast neutron analysis (FNA), Pulsed fast neuron analysis (PFNA), Pulsed fast neutron transmission spectroscopy (PFNTS), Associated particle imaging (API), Pulsed fast-thermal neutron analysis (PFTNA), Fast neutron scattering analysis (FNSA), etc. [85]. We could found more such methods in [85, 88]. A detailed description of these methods is beyond the scope of this thesis. A possibility of usage of the plasma focus as a neutron source for detection of explosive and illicit materials was reported in [89].

In the similar manner like the contraband detection, the neutron sources are used in geology, planetology, and search for raw materials [90, 91].

The neutron radiation is necessary for many research activities or technological tasks. Obviously, the neutrons are generated in nuclear fission reactors, but usually it is inconvenient or impossible to use the nuclear fission reactor. Therefore, the neutrons are also produced by the laboratory sources. The neutron sources could be based on the spontaneous fission. The common such source is ^{252}Cf, however, it is very expensive (hundreds of thousands € [92]) and its half-life is 2.65

Figure 2.7: A system PINS (Portable Isotopic Neutron Spectroscopy) for identification of munition and chemical weapons used by US army [88].

years only. The widespread sources are also the sources based on (α,n) reactions, typically ^{241}Am-Be, or ^{239}Pu-Be. Their half-lifes of 433 years and 24 000 years, respectively are significantly longer than the half-life of the ^{252}Cf, but their costs are also higher. Moreover, it is not possible to simply "switch-off" these radioisotopic sources and a safe storage and ecological liquidation are complicated. Another possibility is to use sources which produce neutrons by the nuclear reactions of an accelerated particle beam with an appropriate target. For example, often used reactions are D(d,n)^{3}He, ^{9}Be(d,n), ^{7}Li(p,n), etc. Such an approach is close to the mechanism of neutron production on Z-pinches and plasma foci with deuterium or deuterated liners. The significant difference between the neutron radiation produced by the accelerator neutron source and Z-pinch or plasma foci is that the accelerator source usually produces the neutrons continuously whereas the Z-pinch is inherently a pulsed device. However, in such relatively short neutron pulse, the Z-pinch is able to generate tremendous amount of the D(d,n)^{3}He neutrons (3.9×10^{13} during tens of nanoseconds [93]). The short and very intensive neutron fluxes are required for many laboratory purposes. For example, it could be used for the study of the multiple neutron capture reactions which are known as the r-processes. Another laboratory application which requires the intensive neutron pulse is the production of isotopes with a high radioactivity and a short half-life. In such a case, the irradiation of a material sample should not be longer than the half-life of the produced isotope, since the decay during the irradiation limits the maximum radioactivity of the sample. The short and intensive neutron pulses generated by Z-pinches allow obtaining the radioisotopes with a practically unlimited half-life (assuming that the neutron pulse duration is on the order of nanoseconds)[5]. In practice, it could be used for example in the neutron activation analysis[6]. As far as the long-duration neutron production is concerned, we note that some Z-pinch modifications, namely small plasma foci with a peak current up to 100 kA could operate in a repetition regime with a frequency up to 10 Hz and produce the neutron bursts continuously [10].

As an example of the repetitive plasma focus neutron source we could mention the PF-6 device with an energy of 6 kJ developed by The Institute of Plasma Physics and Laser Microfusion (IPPLM) in co–operation with the Moscow Physical Society (MPS) [37]. The PF-6 device produces current pulses with current of about 370 kA and shot repetition rate up to 10 Hz [37]. The neutron yield of the PF-6 device achieves 10^8 neutrons per single shot [37]. Another mobile and high-repetition rate plasma focus with similar parameters we found also in ENEA[7] in Italy. Even higher shot repetition rate of 100 Hz was achieved on a portable plasma focus developed by Alameda Applied Sciences Corporation (AASC) [43]. Other examples of small high-repetition rate plasma foci neutron sources can be found all over the world [44, 45, 46].

A substantially different group of plasma focus neutron sources are single shot devices. Whereas the high-repetition shot rate plasma foci are often compact and portable devices, the single shot plasma foci are usually larger, they could occupy whole laboratory or a large part of building. Naturally, their electrical parameters and neutron yield per single shot are significantly higher. We note, that the single

---

[5] The production of radioisotopes with a very short half-life on Z-pinches could be achieved also by the interaction of the pulsed ion beams with a material sample.

[6] The neutron activation analysis lies in the activation of a sample and subsequently the radioisotopic content is determined by the gamma-ray analysis. The original chemical content is evaluated by the known nuclear reactions, their cross-sections and natural isotopic content of the chemical elements. The advantage of this method is that it is nondestructive. Thus, it is often used for analysis of works of art and historical artifacts.

[7] The Agenzia nazionale per le nuove tecnologie, l'energia e lo sviluppo economico sostenibile (Italian National Agency for New Technologies, Energy and Sustainable Economic Development)

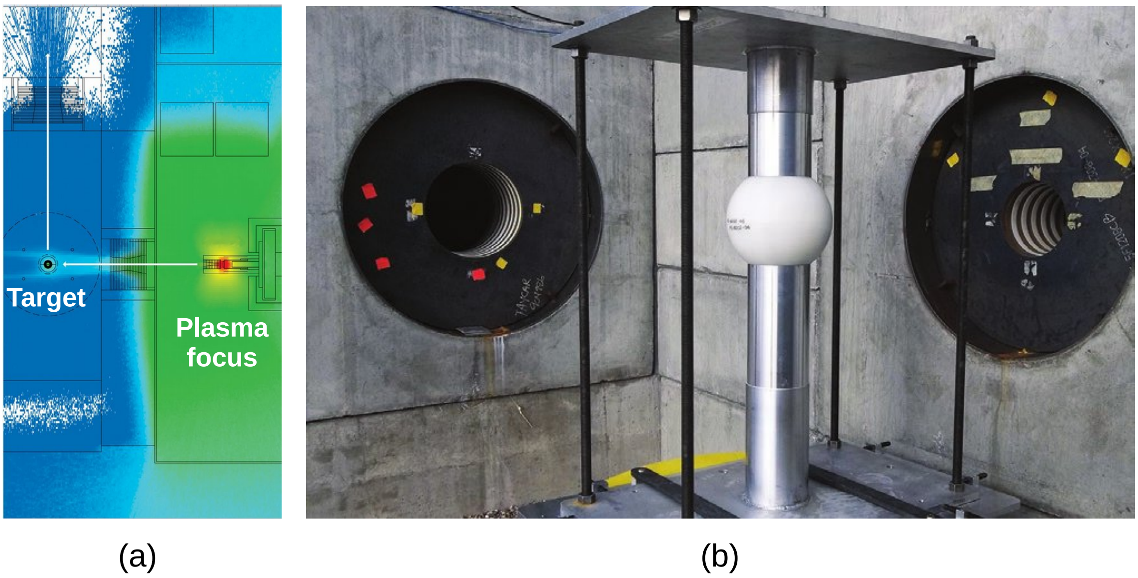

Figure 2.8: (a) Monte Carlo N-Particle transport code (MCNP) simulation of a neutron flux of the neutron-diagnosed subcritical experiment (NDSE) [52]. (b) A photography of the static NDSE target in front of the concrete shielding with ports for the neutron irradiation by the plasma focus and gamma ray detector [52].

shot plasma foci are more common (classical) and most of plasma focus research programs are specialized on the single shot devices. There are various motivations of the single shot plasma focus experiments. Since the mechanism of the neutron production is still not fully clarified, it is studied at many mega ampere-class facilities like PF-1000 [47], PF-360 [48], SPEED 2 [49], FF-1 [50], HAWK DPF [51], etc. A single shot plasma focus device could serve also as an external neutron source for the neutron diagnosed subcritical experiment (NDSE) [52]. The NDSE makes possible to study the nuclear fission under conditions like those at a nuclear explosion, but without the explosion [52]. This topic is very actual due to the international full-scale nuclear test ban treaty [52, 53, 54]. The principle of such NDSE is as follows. A special nuclear material (SNM) target is exposed to the intensive burst of multi-MeV neutrons produced by the plasma focus device. This external neutron burst induce fission chain events in the SNM target and neutron multiplication occurs. At the same time the fission gamma rays are generated. A modern diagnostic techniques make possible to detect both neutrons and gamma rays with nanosecond time resolution [55, 56]. Using time-of-flight and coincidence methods it is possible to distinguish neutron population and gamma rays originated in plasma focus and SNM and evaluate the reactivity and other neutronic properties of the SNM [55, 56]. As far as the SNM target is concerned, it is made from fissile material, usually highly enriched uranium, or plutonium. The SNM target could be represented by static or dynamic device which implodes by an act of detonation of standard explosive (e.g. TNT). An example of the plasma focus static NDSE tests performed by the Los Alamos National Laboratory (LANL) at the Nevada National Security Site (NNSS) is presented in [55] and [56]. For illustration, see fig. 2.8 [52]. In these experiments, two kinds of SNM targets based on highly enriched uranium encapsulated in aluminum and polyethylene were tested. The SNM was placed in the downstream direction 3 m away of the Sodium device. The Sodium device is a 2-MA, 350-kJ plasma focus newly developed by National Security Technologies (NSTec). Since in the NDSE tests the neutron pulse should be as short as possible, unlike the classical plasmafocus, an additional cathode was placed on the z-axis in the distance of about 4 cm from the cathode [55]. By experiments and simulations, it was found that such a limited pinch region reduces the typical neutron pulse length by avoiding the formation of multiple pinches [55]. Using a deuterium-tritium gas mixture, the yield of DT neutrons with the energy of about 14 MeV exceeds 10^{12} per single pulse with the FWHM bellow 100 ns [55, 56]. The detailed description of the diagnostics system and experimental results is beyond the scope of this thesis.

Another very actual application of plasma foci is the flash neutron radiography with high spatial resolution and short exposure time. A notable development of the neutron flash radiography techniques using the Gemini device is presented in [59]. The Gemini device is a plasma focus developed by the NSTec with 1 MJ of the stored electrical energy and the maximum current of 3 MA (see fig. 2.9) [57, 58]. Using a deuterium gas filling, a yield of 2.45 MeV DD neutrons reaches the order of 10^{11}. The neutron radiography image of the tungsten block was converted into the visible light by BC-400 plastic scintillatior. With a help of SMIX Ultra High Speed Framing Camera [61], a sequence of 16 neutron radiography images of a tungsten block was acquired [59]. The exposure time of the individual images was 5 ns and the images were separated by intervals of 10 ns [59]. Such a flash neutron radiography technique seems to be promised for probing of high-density dynamic systems, for example implosions of uranium [60]. Moreover, in the plasma focus NDSE tests, the probing neutrons can be produced by the same plasma focus used to cause the

Figure 2.9: The Gemini plasma focus: stored electrical energy of 1 MJ, current pulse maximum of 3 MA, DD neutron yield above 10^{12} per single shot [57].

fission [59].

2.3.3 Laboratory Astrophysics

Various phenomena which occur in the astrophysical plasma could be simulated using high energy density experimental devices like high power lasers [62, 63], z-pinches [62], plasma foci [64, 66, 65], etc. Notwithstanding that the laboratory scales are very different in comparison with real astrophysical system, it is possible to perform valid experiments. If the certain similarity conditions are fulfilled the scaling factors could be found [62, 67]. Then the physics of scaled experiment is analogical to the physics of the investigated astrophysical system [67].

Such an approach can be used, for example, for study of physics of the supernova explosions and remnants [62, 63, 67], accretion disks around black holes and neutron stars [62], giant planet interiors [68], astrophysical jets [64, 66, 65, 69], and others [62, 70].

As far as the astrophysical jets are concerned, we found them at the young stars, galactic nuclei, microquasars, pulsars, etc. [64, 69] Simulations of the astrophysical jests and plasma flows play an important role in the research program on plasma foci. The pinch evolution lead to generation of the plasma jet along the z-axis of the electrode system. The plasma jet parameters, like temperature, density, motion velocity, etc., are depended on the experimental setup (working gas, pinch current, initial pressure etc.). For illustration, the formation of the plasma jet on the PF-1000 device is displayed in fig. 2.10. These pinhole-MCP[8] images are collected from six individual shots with a neon working gas with initial pressure of 200 Pa, charging voltage of 23 kV, and current maximum of 1.7-1.9 MA [Author's experimental data]. The times in fig. 2.10 are related to the current derivative dip. The first two frames at the times of -290 ns and -145 ns show implosion during the radial acceleration phase. In the frame at the time of -60 ns, we can see a weak beginning of the

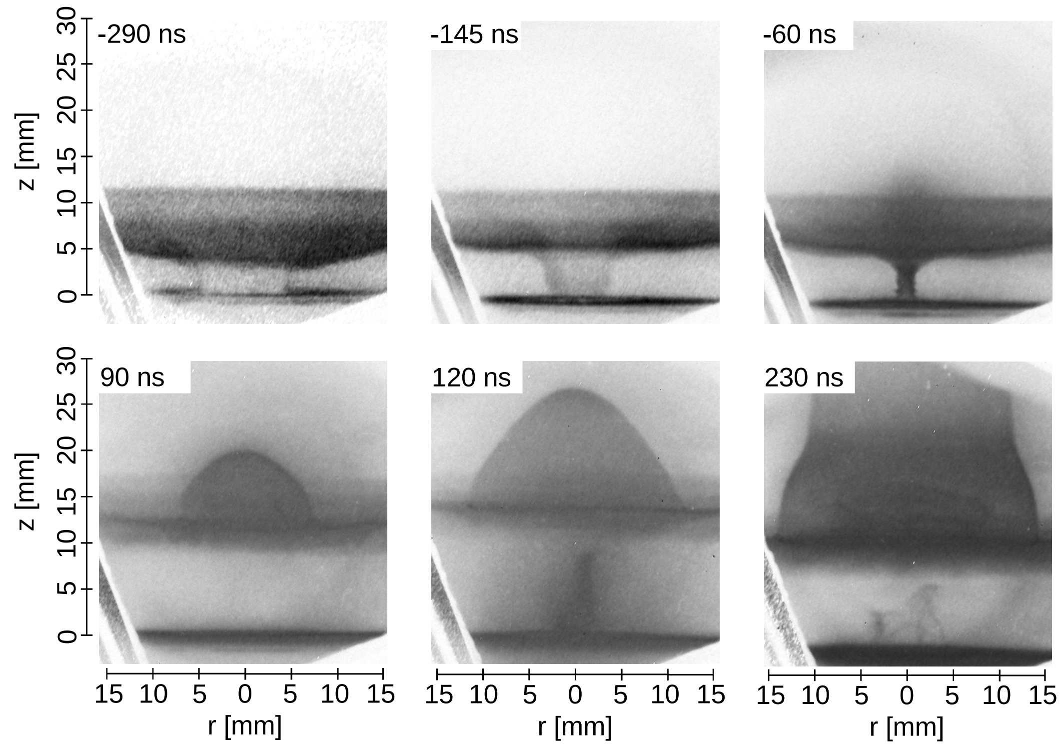

Figure 2.10: Formation of the neon plasma jet front at the PF-1000 with initial working gas pressure of 200 Pa, charging voltage of 23 kV, and current maximum of 1.7-1.9 MA [Author's experimental data]. The times are related to the maximum of the soft x-ray pulse measured by PIN diode.

---

[8] The pinhole camera is based on the gated micro channel plate (MCP) with a nanosecond time resolution which is sensitive the radiation with a wavelength of 0.1-200 nm

formation of the plasma jet front. In the following images at the times 90 ns and 120 ns, the plasma jet front is well visible. In the last image at the time of 230 ns, the dimensions of the plasma jet front are already above the field of vision.

As an important example of a study of the astrophysical plasma jets on the plasma foci, we mention a research on the PF-3 device with the Filippov-type electrode system at National Research Center Kurchatov Institute (NRC KI) in Moscow. The PF-3 is one of the world-largest plasma focus devices with a pulsed power generator composed of capacitor battery with a total capacitance of 9.2 mF. Charging the capacitors to the voltage of 25 kV, the stored electrical energy achieves 2.8 MJ [65] and the load current could achieve up to 4 MA with a rise time of about 10 μs [65]. For an illustration, we can see the PF-3 device in fig. 2.11. The PF-3 device is equipped with a special drift chamber which allowed one to measure the plasma jet and surrounding plasma parameters at the distances of up to 100 cm from the anode forehead [64, 66]. As far as the plasma jet parameters are concerned, the density is up to 10^{23} m^{-3}, the electron and ion temperature achieves 1-5 eV, the plasma jet motion velocity is approximately 5×10^4 m/s, and frozen-in magnetic is typically 10-100 mT [64, 66]. Using a comprehensive diagnostics system which includes high-speed optical recorders [64, 66], time-resolved spectroscopic system [71, 72], multi-channel magnetic probes [66, 73], and others are used for study of the

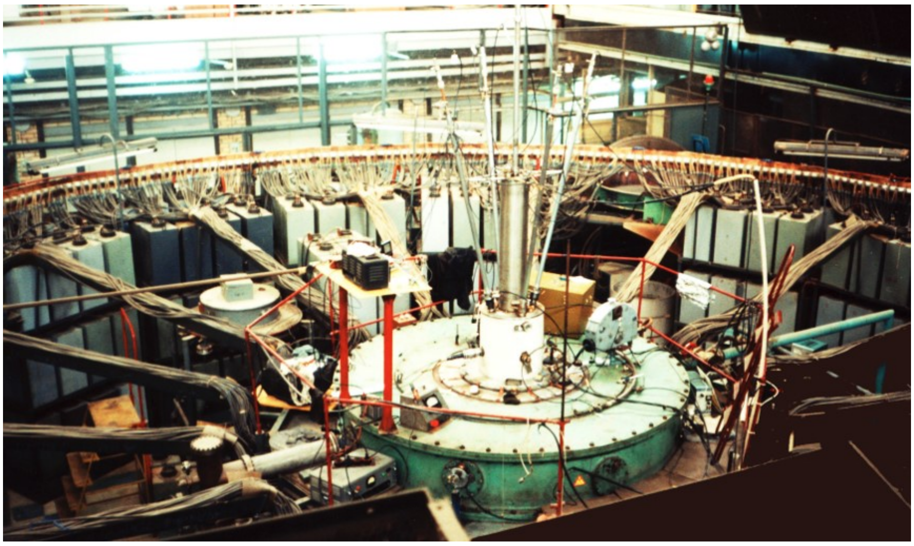

Figure 2.11: The PF-3 Filippov-type plasma focus National Research Center Kurchatov Institute in Moscow, Russian Federation [65].

plasma jet formation, collimation, stability and other features. Based on the results from experiments on the PF-3 device, the mathematical models of the astrophysical jets are formulated [69, 74].

Another example of the study of astrophysical plasma jets using a large plasma focus is the research on the KPF-4-Phoenix device at the Sukhum Physical Technical Institute. In contrast with the PF-3, the KPF-4-Phoenix is the Mather-type plasma focus. Notwithstanding that the maximal allowed charging voltage of the KPF-4-Phoenix is 50 kV, the experiments are usually performed at the charging voltage of 18-20 kV. In such a case, the electrical energy stored in the capacitor bank achieves 230-290 kJ and the current pulse maximum reaches 1.5-2 MA in approximately 7 µs [17, 75].

2.3.4 Pinched Plasma Fundamental Research

Besides that the z-pinch and plasma foci research began approximately 60 years ago, many physical phenomena still have not been explained. From the current fundamental research interests we could mention the following examples. (I) Study of the plasma shocks. The shocks are studied for example on the MAGPIE facility (1 MA, 240 ns) at the Imperial College in London [94] or on the COBRA generator (1 MA, 200 ns) at the Cornel University in New York [95]. (II) Study of the instabilities. An experimental investigation of the pinched plasma instability on the COBRA generator is presented in [95, 96]. The plasma instabilities are also studied on the biggest Z-pinch in the world at the Z-machine (11.4 MJ, 26 MA, 100 ns) in Sandia National Laboratories in Albuquerque [97, 98] in the frame of the MagLIF project [99]. For illustration, the Z-machine is displayed in fig. 2.12(a) and an instability of the MagLIF load without application of the external magnetic field is shown in fig. 2.12(b) [97]. (III) Study of the mechanisms of accelerations of charged particles to MeV energies. At the Z-pinch and plasma focus devices, it was observed that the electron and ion energy significantly exceeds the energy which is possible to explain by currently known physical models. For example, earlier, on the POSEIDON plasma focus in Stuttgart with generator output voltage of 60 kV, ions with energy up to 6 MeV were detected [11]. Recently, ions with energy on the order of tens of MeV were detected at the deuterium gas-puff experiments on the GIT-12 generator (2.6 MJ, 5 MA, 1.7 µs) with the output volatge of 600 kV

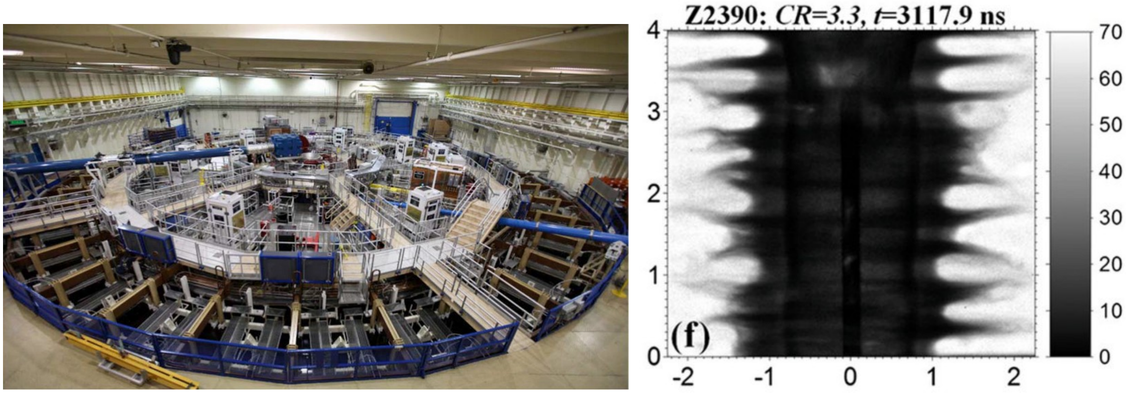

(a) (b)

Figure 2.12: (a) Z-machine in Sandia National Laboratories in Albuquerque, New Mexico: stored electrical energy of 11.4 MJ maximum current of 26 MJ, and rise time 100 ns [99]. (b) An instability of the MagLIF load without the application of the external magnetic field [97].

[100, 101, 102]. An interpretation of these experimental data and a possible explanation is presented in [103, 104]. The theoretical models explaining such accelerations to MeV energies on the Hawk plasma focus (220 kJ, 0.7 MA, 640 kV, 1.2 μs) in Naval Research Laboratories (NRL) are presented in [105]. However, to fully explain this acceleration phenomena the current and magnetic field distribution, dynamic of instabilities, plasma conductivity and other pinched plasma features must be investigated in more detail. This thesis is devoted to the study of these fundamental pinched plasma features on the PF-1000 plasma focus.

At the end of this section, we should mention, that we could found much more applications and research interests then is reported in this thesis. A brief overview of selected plasma focus and z-pinch devices is in the next section.

2.4 Plasma Foci and Z-Pinches in the World

We can find many plasma foci and Z-pinch generators in laboratories all over the world. By far, not all devices and experiments are described in the sections above. To have an overview about the plasma focus devices in the world, the basic parameters and institution affiliation of selected devices are summarized in tab. 2.1. As mentioned above, the significant pinched plasma research is carried on the Z-pinch devices. Therefore, the overview of the Z-pinches is reported in tab. 2.2. Photos of some of the experimental devices from 2.1 and 2.2 are shown in fig. 2.13.

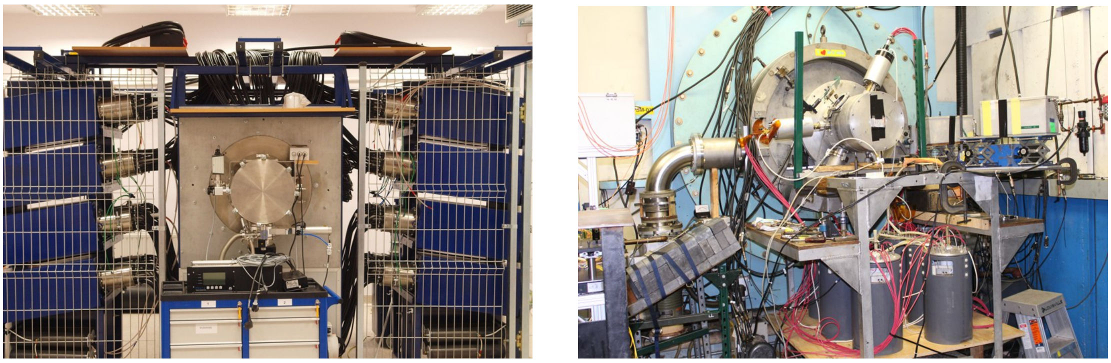

(a) PF-24, IFJ PAN, Krakow, Poland

(b) Hawk, NRL, Washington D.C., USA

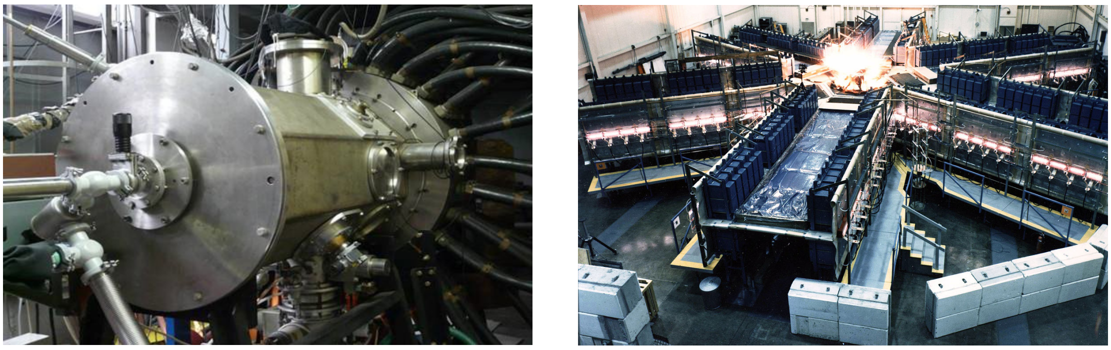

(c) PF-360, NCBJ, Swierk, Poland

(d) Shiva Star, AFRL, Kirtland, USA

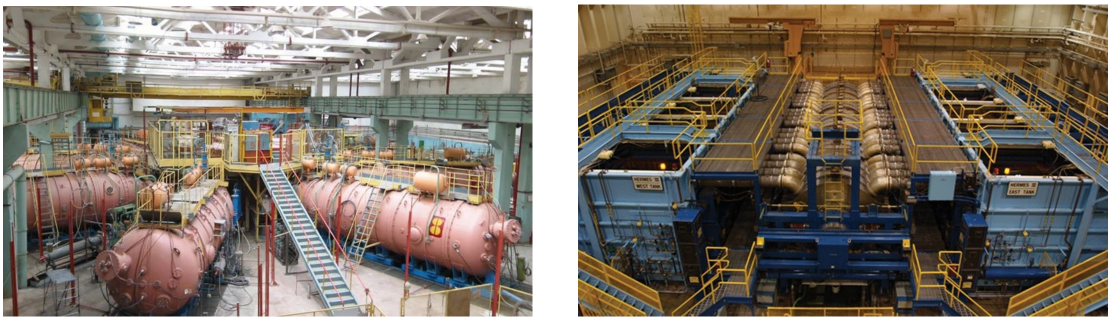

(e) Angara 5, TRINITI, Troitsk, Russia

(f) Hermes-III, SNL Albuqueque, USA

Figure 2.13: Photos of selected plasma focus and z-pinch generators [138, 139, 140, 141, 142].

Device Name	Energy [kJ]	Current [MA]	Voltage [kV]	Rise time [µs]	Geometry Type	Institution	Country	References
Kh-50	4000	0.7	15	80	QSPA	NSC KIPT, Kharkov	Ukraine	[78]
PF-3	2800	11	8-25	10	Filippov	NRC Kurchatov Institute	Russia	[29]
KPF-4-Phoenix	1800	2	18-50	7	Mather	Sukhum Physical Institute	Georgia	[17]
QSPA-M	1400	0.6	40	30	QSPA	NSC KIPT Kharkov	Ukraine	[80]
PF-1000	1060	2.5	16-45	5	Mather	IPPLM, Warsaw	Poland	[106]
Gemini	1000	3	70	6	Mather	NSTec, Las Vegas	USA	[58, 59]
Tallboy	500	2.1	70	6	Mather	NSTec, Las Vegas	USA	[58, 59]
Sodium	350	2.5	35	6	Mather	NSTec, Las Vegas	USA	[58, 59]
HAWK	220	0.7	640	1.2	Mather	NRL, Washington D.C.	USA	[27, 28]
PF-360	200	2.1	38	3	Mather	NCBJ, Swierk	Poland	[11]
SPEED-2	187	2.5	300	0.4	Mather	PPPP, Santiago	Chile	[49]
OneSys	133	1.5	25	6	Mather	NSTec, Las Vegas	USA	[58, 59]
PF-24	93	1.1	25	1.8	Mather	IFJ, Krakow	Poland	[138]
PF-400	80	0.3	27-33	3.5	Filippov	Lebedev Physical Institute	Russia	[107]
FF-1	70	0.4	30-36	2	Mather	LPPL, New Jersey	USA	[16]
BORA	5	0.3	20	1.5	Mather	ICTP, Trieste	Italy	[108]
PF-4	4	0.4	14	3	Mather	Lebedev Physical Institute	Russia	[109]
PFZ-200	4	0.3	20	2	Mather	CTU in Prague	Czech Rep.	[110]
PF-12	3	0.2	16	2	Mather	Tallin University	Estonia	[111]

Table 2.1: Parameters of selected plasma foci devices.

Device Name	Energy [MJ]	Current [MA]	Voltage [MV]	Rise time [ns]	Institution	Country	References
ZR Device	22	26	6	100	SNL, Albuquerque	USA	[112, 114, 115]
Shiva Star	9.4	12	0.12	3000	AFRL, Kirtland	USA	[116]
Julong I (PTS)	7.2	10	6	90	IFP, Mianyang	China	[117, 118]
GIT-12	5	6	0.84	1740	IHCE, Tomsk	Russia	[113]
SPHINX	1.8	6	NA	1000	Centre d'Etudes, Gramat	France	[119, 120]
Hermes-III	1.6	0.7	22	40	SNL, Albuquerque	USA	[121]
Angara 5	1.5	4	1.5	70	TRINITI, Troitsk	Russia	[122]
Saturn	1.4	10	1.9	40	SNL, Albuquerque	USA	[123]
Mercury	0.36	0.36	6	50	NRL, Washington D.C.	USA	[124]
MIG	0.35	2.7	6	100	IHCE, Tomsk	Russia	[125]
MAGPIE	0.34	1.8	2.4	200	Imperial College, London	United Kingdom	[126]
Ambiorix	0.30	2.4	1.2	50	CEA CESTA, Le Barp	France	[127]
Qiang-Guang-I	0.30	2.3	1.2	70	IFP, Mianyang	China	[128]
Gamble II	0.23	1.3	6.8	50	NRL, Washington D.C.	USA	[129]
Zebra	0.2	1.2	2	100	University of Nevada, Reno	USA	[130, 131]
Cobra	0.11	1	NA	100	Cornell University, Ithaca	USA	[132]
CQ-4	0.11	4	0.09	470	IFP, Mianyang	China	[133]
CQ-3	0.08	3	0.09	470	IFP, Mianyang	China	[134]
GIT-32	0.02	1.3	0.08	500	Weizmann Institute, Rechovot	Israel	[135, 136]
MAIZE	0.02	1	NA	100	University of Michigan	USA	[137]

Table 2.2: Parameters of selected Z-pinch generators.

Chapter 3

Apparatus and Diagnostics

3.1 PF-1000 Device

The PF-1000 device is the Mather-type plasma focus at the Institute of Plasma Physics and Laser Microfusion (IPPLM). Examining tab. 2.1 in section 2.4 we can see that PF-1000 is one of the largest plasma focus devices in the world. The PF-1000 device could be divided into two parts: pulsed power generator and electrode system.

3.1.1 Pulsed Power Generator

The pulsed power battery is represented by large capacitor bank composed of 12 identical modules (see fig. 3.1). Each module contain 24 low-inductance capacitors with a capacity of 4.6 μF and maximum voltage of 50 kV. Each capacitor is equipped by dry-air three-electrode spark-gap. Triggering the spark-gaps, all capacitors are connected in parallel and the stored energy is delivered to the transmission lines. The total electrical capacity of such a parallel combination of 288 capacitors is 1.32 mF. As far as the transmission lines are concerned, each of the 12 modules is coupled with 24 coaxial lines which deliver the electrical energy to the electrode system. The maximum electrical energy which could be delivered to the electrode system is of about 1.06 MJ according to 40 kV charging of the capacitors. The maximum short-circuit current of the generator achieves 15 MA. The maximum current which could be reached using the experimental load is approximately 2.5 MA with a rise time (quarter period) of about 5.4 μs. The basic electrical parameters of pulsed power generator of the PF-1000 device are summarized in tab. 3.1.

Total capacitance	1.32 mF
Total inductance	8.9 nH
Characteristic impedance	2.6 mΩ
Charging voltage	16 - 40 kV
Stored electrical energy	168 - 1056 kJ
Maximum short circuit current	15 MA
Maximum load current	2.5 MA
Rise time (quarter period)	5.4 µs

Table 3.1: Parameters of pulsed power generator of the PF-1000 device.

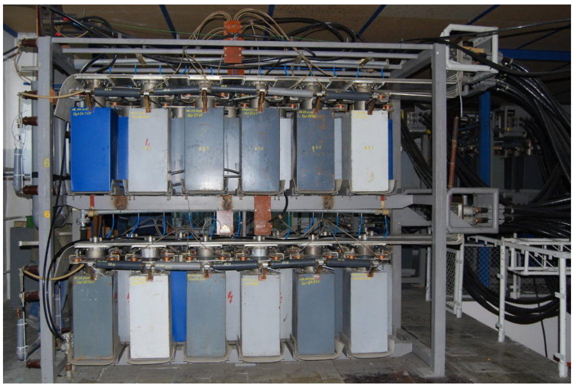

Figure 3.1: One of the 12 modules of the capacitor bank of the PF-1000 pulsed power generator.

3.1.2 Electrode system

The coaxial electrode system with the Mather-type geometry contains a central anode with a diameter of 23 cm and a cathode composed of 12 rods with a diameter of 8.2 cm distributed symmetrically around the anode on a diameter of 40 cm. A length of the coaxial electrode system is 48 cm. The electrode system is placed in a large cylindrical vacuum chamber with a diameter of 140 cm and length of 250 cm. The parameters of PF-1000 electrode system are summarized in tab. 3.2. A photo of the electrode system and vacuum chamber is displayed in fig. 3.2.

Anode diameter	23 cm
Cathode diameter	40 cm
Number of cathode rods	12
Cathode rod diameter	8.2 cm
Anode length	48 cm
Cathode length	48 cm

Table 3.2: Electrode system of the PF-1000 device.

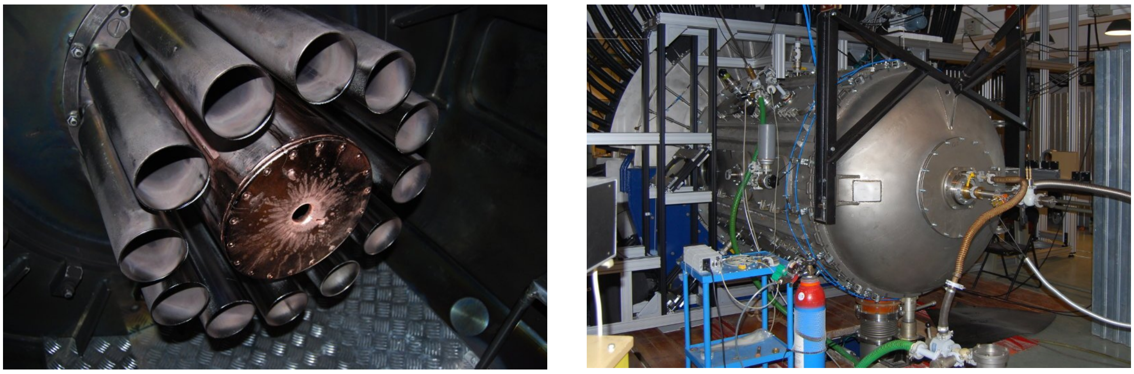

(a) Electrode system

(b) Vacuum chamber

Figure 3.2: Electrode system and vacuum chamber of the PF-1000 device.

3.2 Experimental Diagnostics

On the PF-1000 device an extensive diagnostics system including several kinds of neutron, x-ray, and ion detectors, fast 2D imaging systems, and laser interferometry is established. For this thesis, the most important diagnostics are neutron time-of-flight detectors, silver activation neutron detectors, MCP x-ray pinhole camera, and Mach–Zehnder optical interferometer. Therefore this diagnostics is described in the following subsections.

3.2.1 Neutron Time-of-Flight Detectors

The neutron time-of-flight (nToF) detectors used in experiments on the PF-1000 device are based on the plastic scintillators Saint Gobain BC-408 made of polyvinyltoluene with a density of 1.032 g/cm^3 [143]. The scintillators are of cylindrical shape with 4.5 cm in diameter and a length of 5 cm. The scintillators produce pulses of the visible light with a wavelength of 425 nm [143]. A FWHM of the light pulses is of about 2.5 ns. Properties of the BC-408 scintillators are summarized in tab. 3.3.

Material	Polyvinyltoluene
Density	1.032 g/cm^3
Shape	cylinder
Diameter	4.5 cm
Length	5 cm
Light pulse rise time	0.9 ns
Light pulse decay	2.1 ns
Light pulse FWHM	2.5 ns
Wavelength of max. light emission	425 nm

Table 3.3: Properties of the scintillator BC-408 [143].

The light pulses produced by the scintillator are detected by the photomultiplier tube (PMT) assembly Hamamatsu H1949-51 with the bialkali photocathode with an effective diameter of 4.6 cm and 12 dynode stages [144]. Since the maximum of the PMT sensitivity is at the wavelength of 420 nm, the PMT is suitable for the operation in a combination with the BC-408 scintillator. As far as the time response of the PMT is concerned, the anode pulse rise time is of about 1.3 ns. Parameters of the used PMT Hamamatsu H1949-51 are summarized in tab. 3.4.

Photocathode material	Bialkali
Diameter of photocathode effective area	4.6 cm
Window material	Borosilicate glass
Spectral range	(300 - 650) nm
Wavelength of Maximum Response	420 nm
Dynode structure	12 stages
Anode pulse rise time	1.3 ns

Table 3.4: Parameters of the photomultiplier assembly Hamamatsu H1949-51 [144].

To minimize an interference of the nToF detectors by scattered neutrons, a paraffin shielding is used. In order to increase the detection dynamic range, the detector output is split into two identical signals using passive signal splitter. Such split detector output is connected to the two oscilloscope inputs with a different sensitivity. For this purpose, digital storage oscilloscope Tektronix TDS-3054 with a 500 MHz bandwidth and 10-bit A/D convertor is used. Whole system of detector and data acquisition is placed in the Faraday screening cage. A scheme of the nToF detector and data acquisition system is displayed in fig. 3.3.

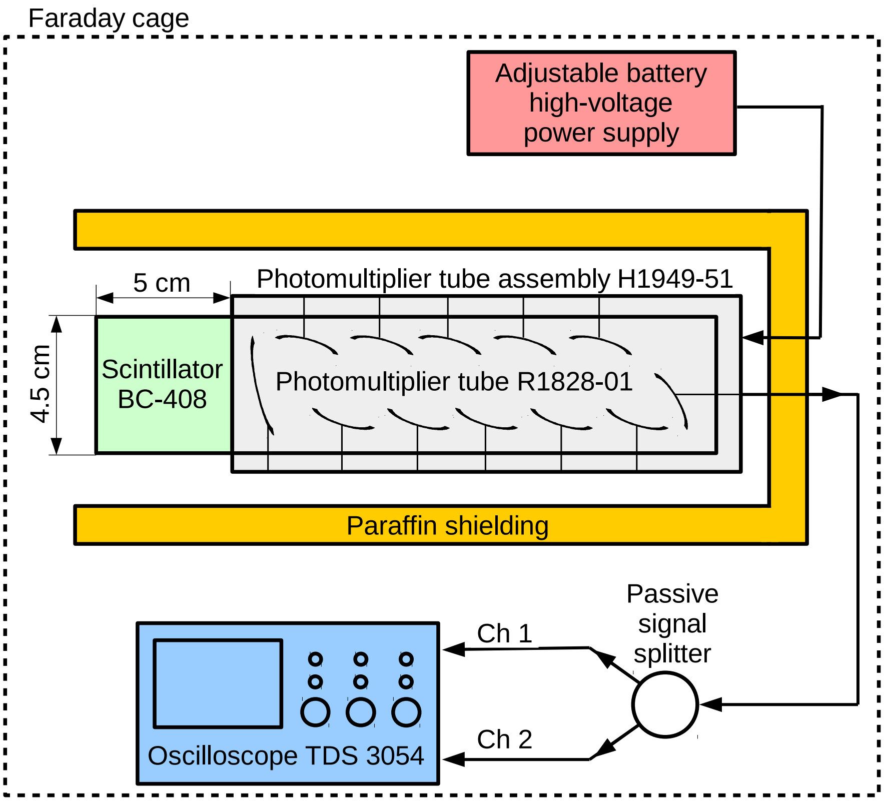

Figure 3.3: Scheme of the time-of-flight detector system.

Features of such nToF diagnostics was thoroughly tested and reported in Klir's paper [145]. A total time resolution of the nToF detection system is 5.5 ns [145]. As far as the dependence of the detection efficiency on the neutron energy is concerned, in the range of considered neutron energies (1.8 - 3.1) MeV, the changes in the detection efficiency are negligible [145]. Photo of the used nToF detector is displayed in fig. 3.4.

In the experiments on the PF-1000 reported in this thesis, three nToF detectors

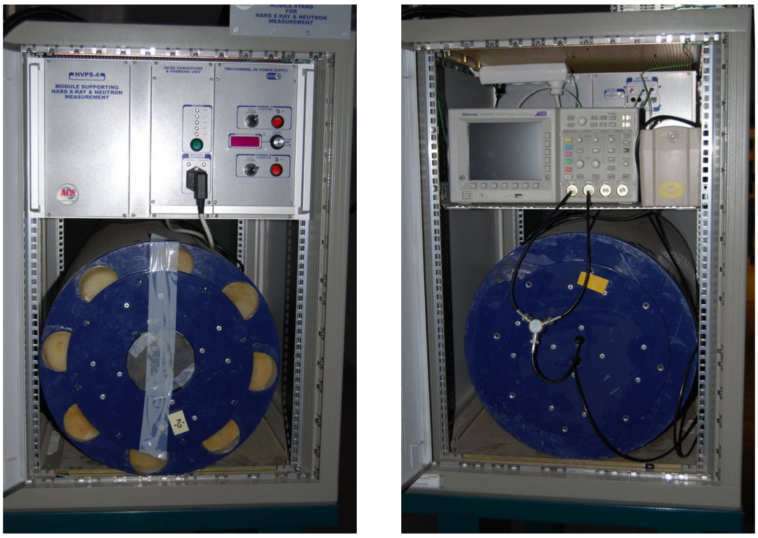

(a) Front side (b) Rear side

Figure 3.4: Photography of the neutron time-of-flight detector.

in the downstream, radial, and upstream directions are used. Each nToF detector is placed at the distance of 7 meters from the pinched plasma. Arrangement of the nToF detectors is shown in fig. 3.5. Using the time of flight methods, it is possible transform the time resolved signal of the nToF detectors into the neutron spectrum [146, 147, 148, 149]. Assuming that the duration of the neutron emission is much shorter than the time of flight of neutrons from their source to the detector, the neutron energy spectrum could be evaluated by formula

$$f(E_n) = s(\tau, d)\frac{A}{\eta(E_n)}\frac{(\tau - t_0)^3}{m_n}\frac{1}{S}, \tag{3.1}$$

where E_n is a neutron energy, $s(\tau, d)$ is a signal of the detector in the distance d at a detection time τ, A is the PMT sensitivity, η is a scintillator detection efficiency, t_0 is a time of the neutron emission, m_n is the neutron mass, and S is a detection (scintillator) surface. Such approach is so-called “basic time-of-flight method”. If the neutron emission is longer than the neutron time of flight to the detector, or if time resolved neutron spectrum is needed, it is possible to use the “extended neutron time-of-flight method”. The extended time of flight employes several detectors and the neutron spectrum is reconstructed using numeric Monte Carlo methods [146, 147]. This method was also established in the experiments on the PF-1000 device [148, 149].

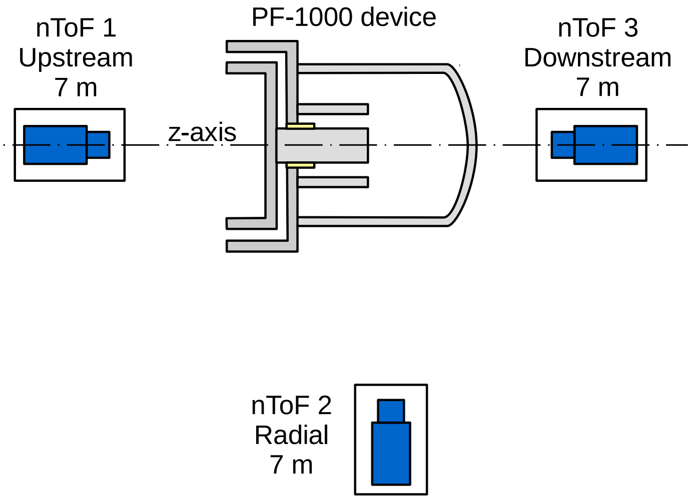

Figure 3.5: Arrangement of the neutron time-of-flight detectors.

3.2.2 Silver Activation Neutron Counters

Neutron yield (number of produced neutrons per single experimental shot) is useful quantitative and qualitative parameter, since it carry an information about the number of reached fusion reactions.

The nToF detectors allow us to evaluate an energy spectrum of a short neutron pulse. However, it is complicated to estimate a total neutron yield by the nToF detectors. An established diagnostic instrument for measurement of neutron yield of pulsed neutron sources is the silver activation counter (SAC).

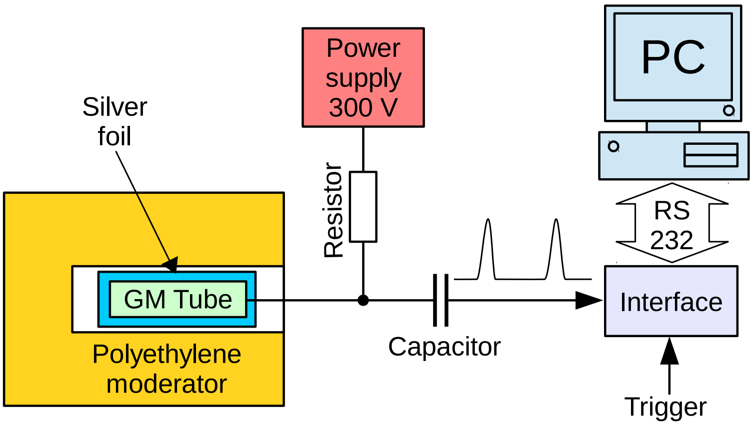

Figure 3.6: Block scheme of the silver activation neutron counter.

A block scheme of the SAC is displayed in fig. 3.6. Principle of neutron detection by the SAC is as follows. Fast DD neutrons with the energy of about 2.45 MeV are moderated by a massive block of polyethylene. Inside the polyethylene block, the Geiger–Müller tube is placed. The Geiger–Müller tube is enveloped by the natural silver foil. The natural silver is composed of two stable isotopes: ^{107}Ag with an abundance of about 52% and ^{109}Ag with an abundance of about 48%. The moderated neutrons induces neutron radiative capture reactions

$$^{107}\mathrm{Ag}(\mathrm{n},\gamma)^{108}\mathrm{Ag}\left(T_{1/2}=142.9\,\mathrm{s}\right)\longrightarrow^{108}\mathrm{Cd}+\beta^{-}\,(97.2\%) \tag{3.2}$$

and

$$^{109}\mathrm{Ag}(\mathrm{n},\gamma)^{110}\mathrm{Ag}\left(T_{1/2}=24.6\,\mathrm{s}\right)\longrightarrow^{110}\mathrm{Cd}+\beta^{-}\,(99.7\%). \tag{3.3}$$

Total cross-sections of the reactions (3.2) and (3.3) are shown in fig. 3.7. Examining fig. 3.7, it is obvious, that the total cross-sections of the reactions (3.2) and (3.3) are much higher at the lower neutron energies than the energy of DD neutrons (of about 2.45 MeV). Therefore the polyethylene moderator is used. Products of the neutron capture reactions ^{108}Cd and ^{108}Cd are unstable isotopes with the half-lifes of 142.9 s and 24.6 s, respectively [150]. The β^{-} radiation of the unstable products

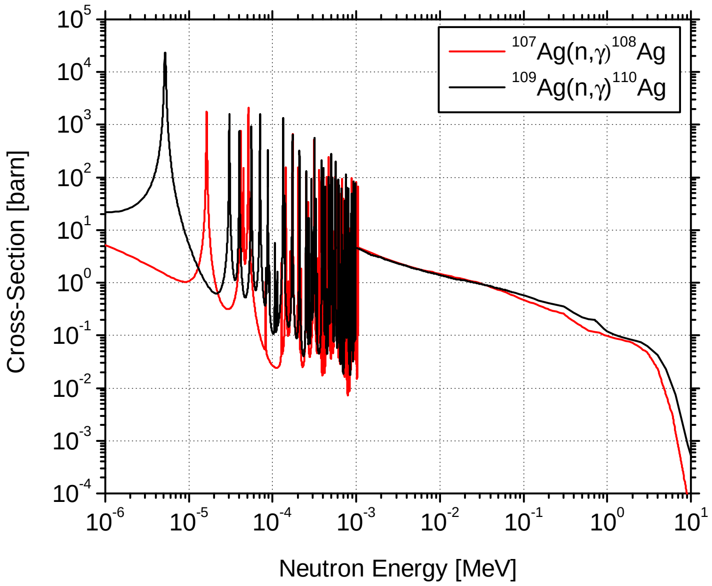

Figure 3.7: The total cross-sections of the radiative neutron capture reactions of natural silver isotopes

is detected by the Geiger–Müller (GM) tube. A number of counts of the GM tube is given by formula

$$C_{SAC} = K_1 \frac{\Phi}{\lambda_1} \left(e^{-\lambda_1 t_1} - e^{-\lambda_1 (t_1 + \Delta t)} \right) + K_2 \frac{\Phi}{\lambda_2} \left(e^{-\lambda_2 t_1} - e^{-\lambda_2 (t_1 + \Delta t)} \right) + C_B, \quad (3.4)$$

where K_1 and K_2 are calibration coefficients, t_1 is the start of the counting and Δt is a duration of the counting, λ_1 and λ_2 are decay constants of the ^{108}Ag and ^{109}Ag isotopes, and C_B is number of counts caused by a background radiation. The SAC is calibrated in-situ using the ^{241}Am-Be neutron source with the exactly defined number of emitted neutrons per second. Output pulses of the Geiger–Müller tube are counted using a computer.

3.2.3 MCP X-ray Pinhole Camera

In order to obtain the time resolved images in the extreme ultraviolet (EUV) and soft X-ray (SXR) region, a pinhole camera (camera obscura) with gated microchannel plate is used. The arrangement of the MCP pinhole camera is shown in fig. 3.8. The microchannel plate is split into 4 independent segments. Using 2×2 pinhole matrix, the hot plasma is projected to each MCP segment. The ZnS luminophore of the MCP emits green visible light which is detected by the CCD camera. Parameters of the MCP are reported in tab. 3.5. A time resolution of the MCP x-ray pinhole camera is given by the high-voltage power supply pulse. A full width of half maximum (FWHM) of the high voltage pulse is about 5 ns. Supplying each MCP segment by the high-voltage pulse in a different time we obtain a time sequence of 4 images in

Photocathode material	Gold
Usable diameter	5.2 cm
Spectral range	0.1 - 200 nm
MCP channel diameter	12 μm
MCP chanel to channel distance	16 μm
Luminophore	ZnS
Output light wavelength	520 nm (Green)

Table 3.5: Parameters of the microchannel plate.

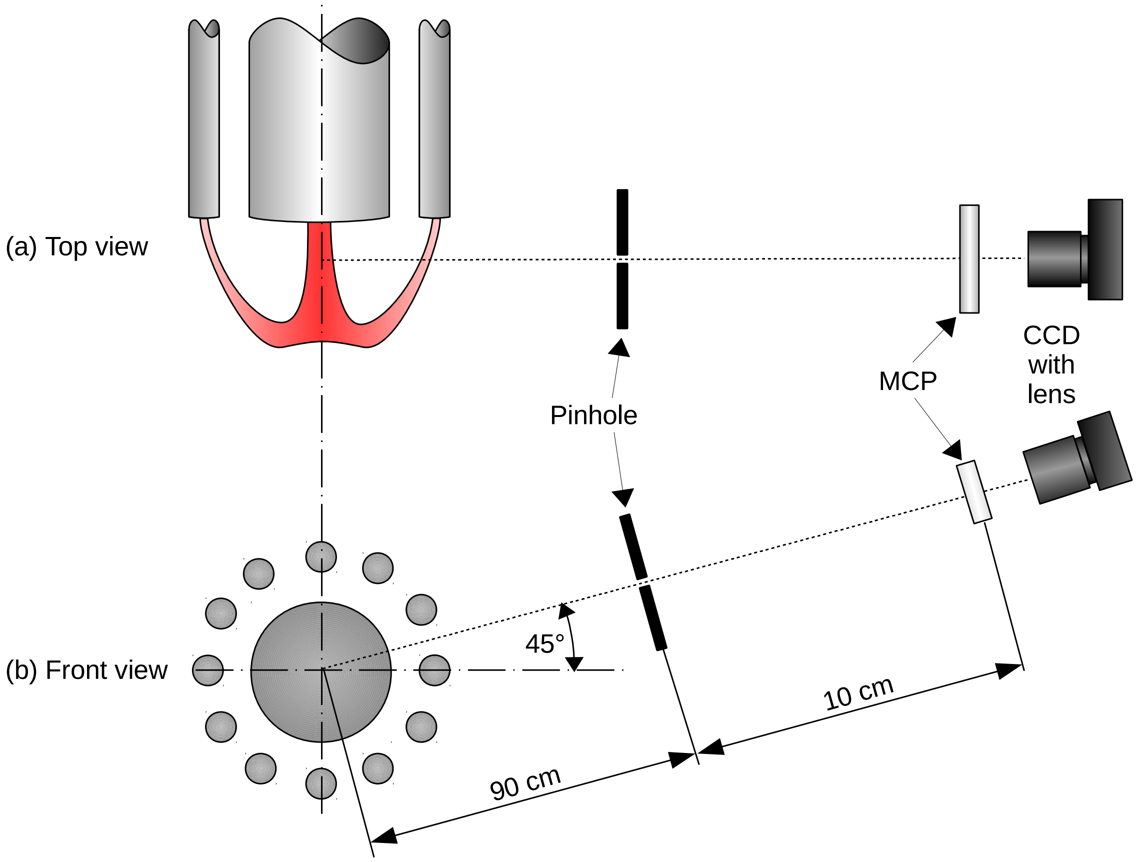

Figure 3.8: A scheme of MCP X-ray pinhole camera.

the photon energy region from 6 eV to 12 keV (UV and SXRs). In our case, the Z-pinch (plasma focus) plasma with the temperature of 0.1–1 keV, could significantly emit UV and SXRs with the mentioned energies by line radiation, recombination radiation, and bremsstrahlung.

The line radiation (bound-bound transition) is emission of a photon with the exactly defined energy which corresponds with a transition of an electron from an upper level to a lower level of some atom or ion.

The recombination radiation (free-bound transition) occurs when a free electron is captured by an ion and transits into a bound state. The difference between the original electron energy and energy of the bound state is radiated by photon. Spectrum of the recombination radiation is continuous with the edges given by the bound state energies. Power of the recombination radiation could be calculated by equation [1]

$$P_r = 1.69 \times 10^{-32} N_e \sqrt{T_e} \sum \left[Z^2 N(Z) \left(\frac{E_\infty^{Z-1}}{T_e} \right) \right], \ \left[\mathrm{W/cm^3}\right], \tag{3.5}$$

where N_e is the electron density, T_e is the electron temperature, $N(Z)$ is the density of of ions with the charge state Z, E_∞^{Z-1} is binding energy of outer electron, and the sum is over all ionization states [1].

The bremsstrahlung (free-free transition) is emitted when an electron is decelerated in the electric field of a collision nucleus. The energy loosed by the electron is converted into the electromagnetic radiation. Obviously, since the electron loses its energy continually, the bremsstrahlung energy spectrum is also continuous. A radiation power of bremsstrahlung from the hydrogen-like plasma is given by formula [1]

$$P_{br} = 1.69 \times 10^{-32} N_e \sqrt{T_e} \sum \left[Z^2 N(Z) \right], \ \left[\mathrm{W/cm^3}\right], \tag{3.6}$$

where N_e is the electron density, T_e is the electron temperature, Z is the charge state, and the sum is over all ionization states [1].

Thus, using the MCP X-ray pinhole camera we could obtain the time resolved visualization of plasma regions with a higher temperature, and/or a higher density, and/or admixtures with a higher atomic number.

The radiative processes in plasmas are described in more detail in [151].

3.2.4 Laser Interferometry

Interferometry is one of the most precise non-invasive methods how to measure the electron density of a hot plasma electron with the high spatial and time resolution. The interferometric measurement is fundamental diagnostic instrument in the experiments on the PF-1000 device. Therefore, it is described in more detail.

Interferometry method

If ω frequency of an electromagnetic wave is higher than ω_e electron plasma frequency or if n_e electron density of plasma is lower than n_{ec} critical electron density [154]

$$n_e \leq n_{ec} = \omega^2 \frac{\varepsilon_0 m_e}{e^2}, \tag{3.7}$$

where ε_0 is the permittivity of vacuum, m_e is the electron rest mass, and e is the charge of electron, the electromagnetic wave propagates through the plasma with the refractive index N approximated by formula [154]

$$N \approx 1 - \frac{1}{2}\frac{\omega_e}{\omega} = 1 - n_e \lambda^2 \frac{e^2}{8\pi^2 \varepsilon_0 c^2 m_e}, \tag{3.8}$$

where c is the light velocity and λ is the electromagnetic wave wavelength. In the optical range, it allows to measure an electron density approximately $(10^{20} - 10^{26})$ m^{-3} by various interferometer designs. In experiments on the PF-1000 device, the interferometer system is based on the optical Mach-Zehnder interferometer. Principle of the Mach-Zehnder interferometer is shown in fig. 3.9. A laser[1] beam is split into two arms by the mirror with a reflectivity of 50%[2]. The first arm (probing) pass through the probed object which is the hot plasma in our case. The second arm (reference) goes outside the plasma. Subsequently, the probing and reference beams are directed to a photo detector (e.g. CCD, photographic film, etc.) where the interference of the beams is detected. Evidently, the reference arm wave $U_r(t)$ could be described by formula

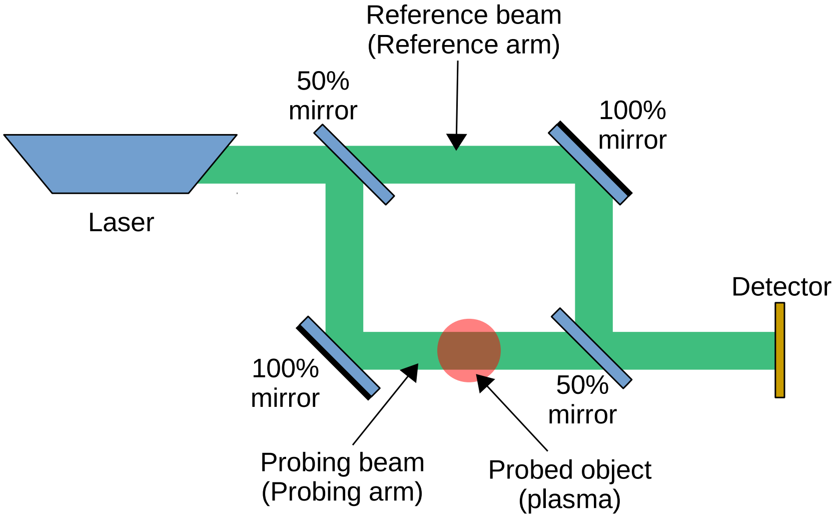

Figure 3.9: Principe of the optical Mach-Zehnder interferometer.

$$U_r(t) = U_{r0} \exp\left\{ i \left[\omega \left(t - \frac{X_r}{c} \right) \right] \right\}, \tag{3.9}$$

---

[1] In principle, it is possible to use a non-coherent light like in the case of the first Mach-Zehnder interferometers in the end of the 19th century. However, it is simpler and more practical to use laser. Therefore, nowadays laser is used in almost all optical interferometers.

[2] Usually mirrors with a reflectivity of 50% are used, but we can meet also interferometers which use splitter mirros with different reflectivity

where U_{r0} is an amplitude of the reference wave, ω is a wave angular velocity, X_r is a length of the reference arm (distance from the laser source to the detector), and c is the light velocity. Similarly, we can describe the probing arm wave

$$U_p(t) = U_{p0} \exp\left\{ i \left[\omega \left(t - \frac{X_p}{c} - \frac{\int_A^B \left[N(x,y,z) - 1\right] dx}{c} \right) \right] \right\}, \tag{3.10}$$

where U_{p0} is an amplitude of the probing wave, X_p is a length of the reference arm, A is a point where the probing beam enters the plasma, B is a point in which the probing beam leaves the plasma, and $N(x,y,z)$ is a refractive index of the plasma in the point (x,y,z). A phase of the reference wave we substitute as

$$\varphi_r = \omega \left(t - \frac{X_r}{c} \right) \tag{3.11}$$

and a phase of the probing wave as

$$\varphi_p = \omega \left(t - \frac{X_p}{c} - \frac{\int_A^B \left[N(x,y,z) - 1\right] dx}{c} \right) \tag{3.12}$$

The superposition of the probing and the reference beam on the detector gives sum [153]

$$U_\Sigma(t) = U_{r0} \exp\left\{ i\varphi_r \right\} + U_{p0} \exp\left\{ i\varphi_p \right\} \tag{3.13}$$

The photodetectors are sensitive to the light intensity

$$I = U_\Sigma U_\Sigma^*, \tag{3.14}$$

where U_Σ^* is the complex conjugate wave. By the combination of equations (3.13) and (3.14) we obtain expression [153]

$$I = \left(U_{r0} \exp\left\{ i\varphi_r \right\} + U_{p0} \exp\left\{ i\varphi_p \right\} \right) \left(U_{r0} \exp\left\{ -i\varphi_r \right\} + U_{p0} \exp\left\{ -i\varphi_p \right\} \right). \tag{3.15}$$

After mathematical modifications, the equation (3.15) could be expressed as [153]

$$I = U_{r0}^2 + U_{p0}^2 + U_{r0} U_{p0} \left[\exp\left\{ i(\varphi_r - \varphi_p) \right\} + \exp\left\{ -i(\varphi_r - \varphi_p) \right\} \right]. \tag{3.16}$$

Using the Euler's formula we obtain [153]

$$I = U_{r0}^2 + U_{p0}^2 + 2U_{r0} U_{p0} \cos(\varphi_r - \varphi_p). \tag{3.17}$$

after an inverse substitution of (3.11) and (3.12) we obtain [153]

$$I = U_{r0}^2 + U_{p0}^2 + 2U_{r0} U_{p0} \cos\left(-\frac{\omega}{c} X_r + \frac{\omega}{c} X_p + \frac{\omega}{c} \int_A^B \left[N(x,y,z) - 1\right] dx \right). \tag{3.18}$$

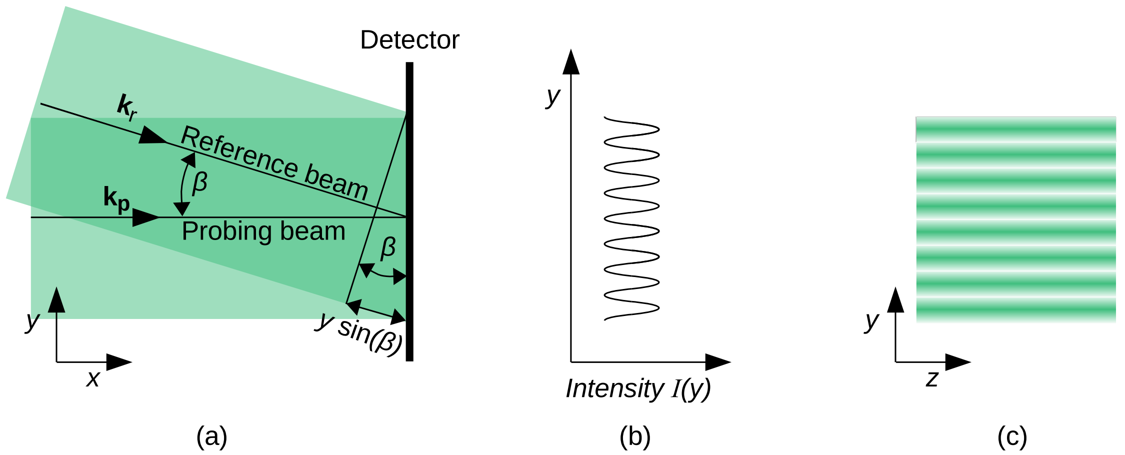

Figure 3.10: Interference of the probing and reference beams. (a) Visualization of the angle β between the probing and reference laser beam incoming to the detector plane. (b) Dependence of the interference image intensity on y-coordinate - forming of the interference stripes. (c) Interference image without phase shifts caused by the plasma.

In the case of the Mach-Zehnder interferometer we usually consider $X_r = X_p$. Expressing ω/c as $2\pi/\lambda$ where λ is the laser wavelength, the equation (3.18) becomes to

$$I = U_{r0}^2 + U_{p0}^2 + 2U_{r0}U_{p0}\cos\left(\frac{2\pi}{\lambda}\int_A^B \left[N(x,y,z)-1\right]dx\right). \tag{3.19}$$

Thus, the intensity of the light in the photodetector plane (y, z) is depended on the phase shift $2\pi/\lambda \int_A^B [N(x,y,z)-1]\,dx$. However, since the cosine function is even function, we are not able to distinguish between the positive and negative time shift. Therefore, in practice, the reference wave arrives to the detector plane (y, z) with a different angle than the probing wave. Thus, considering that the wave vector $\mathbf{k}_p$ of the probing wave is perpendicular to the detector plane (y, z) it forms an angle β with the wave vector $\mathbf{k}_r$ of the reference wave. This situation is displayed in fig. 3.10. If the vectors $\mathbf{k}_p$ and $\mathbf{k}_r$ lie, for example in the plane (y, x), difference of phases of the incoming reference wave and probing wave is shifted by $2\pi y\sin(\beta)/\lambda$ or, for a small β, the phase shift could be approximated as $2\pi y\beta/\lambda$. Consequently, the light intensity in the detector plane (y, z) is also depended on the y-coordinate. Thus, the intensity of the laser light in the detector plane (y, x) is [153]

$$I = U_{r0}^2 + U_{p0}^2 + 2U_{r0}U_{p0}\cos\left(\frac{2\pi}{\lambda}\left[y\sin\beta + \int_A^B [N(x,y,z) - 1]\,dx\right]\right). \tag{3.20}$$

If the probing wave passes through a medium with the same refractive index as the reference wave (vacuum or air), parallel light stripes with a period given by β and λ in the detector plane are formed. If the probing wave passes through a plasma with some $N(x, y, z)$ different from the refractive index of the vacuum or air, the stripes are deflected. If the signs of the derivatives $\partial\left(\int_A^B [N(x,y,z) - 1]\,dx\right)/\partial y$ and $\partial\left(2\pi y\sin\beta/\lambda\right)/\partial y$ are the same, the stripes will get closer along the y-axis. And conversely, if the signs of the derivatives are different, a distance between the stripes will be growing [153].

As far as the practical usage of (3.20) is concerned, values of $U_{r0}(y, z)$ and $U_{p0}(y, z)$ we could found by alternately blocking the reference and probing beams in the interferometer and a value of $2\pi y\sin\beta/\lambda$ we found by an unperturbed interferogram (without plasma)[153]. Consequently we could find the phase shift caused by the differences of the reflective index

$$\phi(y,z) = \frac{2\pi}{\lambda}\int_A^B [N(x,y,z) - 1]\,dx. \tag{3.21}$$

To evaluate the electron density, we use formula (3.8). Assigning values in SI units to variables in (3.8) we obtain

$$N - 1 = -4.46 \times 10^{-16}\lambda^2 n_e. \tag{3.22}$$

The combination of the equations (3.21) and (3.22) gives

$$\phi(y,z) = -2\pi\lambda\,4.46 \times 10^{-16}\int_A^B n_e(x,y,z)dx. \tag{3.23}$$

Since the classical interferometry with one probing beam gives only two-dimensional projection of the probed plasma, it is impossible to determinate three-dimensional[3] distribution of $N(x, y, z)$. However, in many practical cases, like z-pinch structures, an axial symmetry could be assumed. Thus, the refractive index is constant on a radius r.

---

[3] To find three-dimensional distribution of $N(x, y, z)$ is possible to use holographic interferometry.

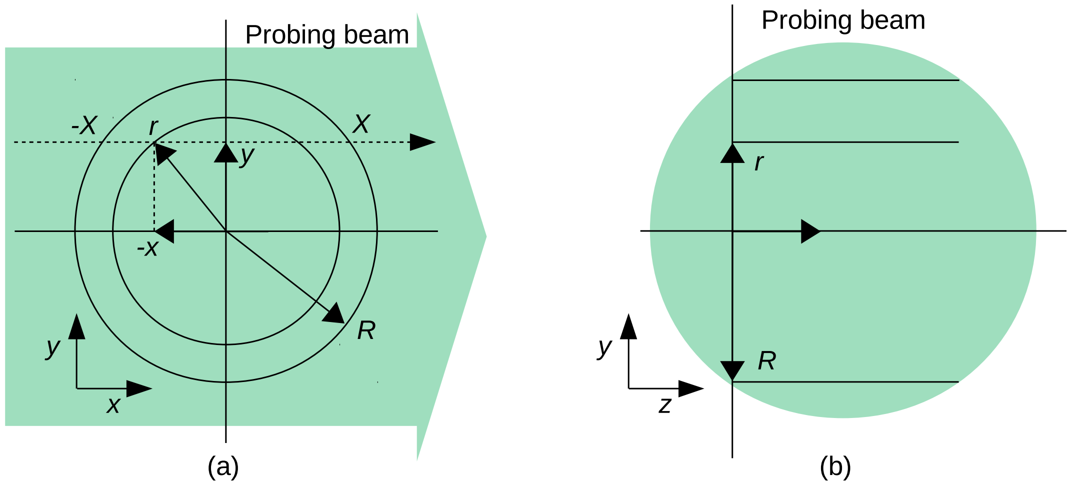

Figure 3.11: Cross-section of the probing laser beam and probed plasma (a) in xy-plane, (b) yz-plane.

Transforming equation (3.21) to the cylindrical coordinate system (see fig. 3.11) we obtain

$$\phi(y,z) = -2\pi\lambda\, 4.46 \times 10^{-16} \int_{-X}^{X} n(r,z)dx = -4\pi\lambda\, 4.46 \times 10^{-16} \int_{0}^{X} n(r,z)dx. \tag{3.24}$$

Substituting $x = \sqrt{r^2 - y^2}$ and $dx = \dfrac{r}{\sqrt{r^2 - y^2}}dr$ we obtain

$$\phi(y,z) = -4\pi\lambda\, 4.46 \times 10^{-16} \int_{y}^{R} \frac{r n_e(r)}{\sqrt{r^2 - y^2}}dr, \tag{3.25}$$

where R is the radius of the axisymmetric plasma. The equation (3.25) is the well-known Abel transform of the electron density $n_e(r)$ [153, 155, 156]. Therefore, it is possible to find $n_e(r)$ by the inverse Abel transform [153, 155, 156]

$$n_e(r,z) = \frac{1}{2\pi^2\lambda 4.46 \times 10^{-16}} \int_{r}^{R} \frac{d\phi(y,z)}{dy} \frac{dy}{\sqrt{y^2 - r^2}}. \tag{3.26}$$

The equation (3.26) could be solved by numeric methods. For practical purposes, especially for pinched plasma, could be used the following method which simplify processing of the interferometric data [157].

If, in the point (x,y), the phase shift caused by the plasma is equal to δ-multiple of the wavelength of the probing laser, then an element of interference strip which without influence of the plasma was in the point (x, y) is shifted by δ-multiple of distance of the neighboring strips. Thus, substituting $\phi(y,z) = \delta(y,z)\,2\pi$ in equation (3.25) we obtain

$$\delta(y,z) = -2\lambda\,4.46 \times 10^{-16} \int_y^R \frac{r n_e(r)}{\sqrt{r^2 - y^2}} dr \qquad (3.27)$$

and Abel inversion

$$n_e(r,z) = \frac{1}{\pi\lambda 4.46 \times 10^{-16}} \int_r^R \frac{d\delta(y,z)}{dy} \frac{dy}{\sqrt{y^2 - r^2}}, \qquad (3.28)$$

is possible to numerically solve easily. A result constant from the integral in (3.28) practically represents difference between plasma which surrounding the pinch structure. Since a density of the pinched plasma is much higher (by several orders of magnitude) in the case of dense plasma foci and Z-pinches, the integration constant is neglected.

16-frame Mach-Zehnder Interferometer

Laser probing system used in experiments on the PF-1000 device is based on the 16-channel Mach-Zehnder interferometer. This world unique probing system developed by Dr. Marian Paduch is the key plasma diagnostic instrument in experiments on the PF-1000 device. Principle of this laser probing system is schematically shown in fig. 3.12.

The probing pulsed beam is generated by Nd:YLF (Neodymium-doped yttrium lithium fluoride) laser. Wavelength of this laser is 1053 nm and pulse length is less than 1 ns. For the interferometric probing, the laser beam is converted to the second harmonic with a wavelength of 527 nm (visible green light) with a help of KD*P (potassium dideuterium phosphate) crystal . Energy of the pulses with the second harmonic wavelength is about 500 mJ. The original laser beam diameter of 12 mm is increased to 60 mm by the expander [152].

The expanded probing beam enters to the optical splitter and delay line system. By the system of mirrors with 100% and 50% reflectivity, the original single beam is splitted into 16 beams (see fig. 3.12). The length paths of each beam are specially chosen to obtain delays of 10 ns and 20 ns between individual beams (absolute delays of 0, 10, 30, 40, 60, 70, 90, 100, 120, 130, 150, 160, 180, 190, 210 and, 220 ns).

These delayed beams are expanded to the diameter of 150 mm to cover the dimensions of the hot plasma produced by the PF-1000 device. These expanded beams arrive to the Mach-Zehnder interferometer where each mirror is common for all beams. The probing beams pass through the hot plasma in front of the electrode system and the reference beam pass outside the experimental chamber.

The interferometer output beams are directed to 4 photographic films by a beam separator represented by a system of prisms. To avoid an irradiation of the photographic films by plasma the radiation, an interferometric filters are placed on the outputs of the beam separator.

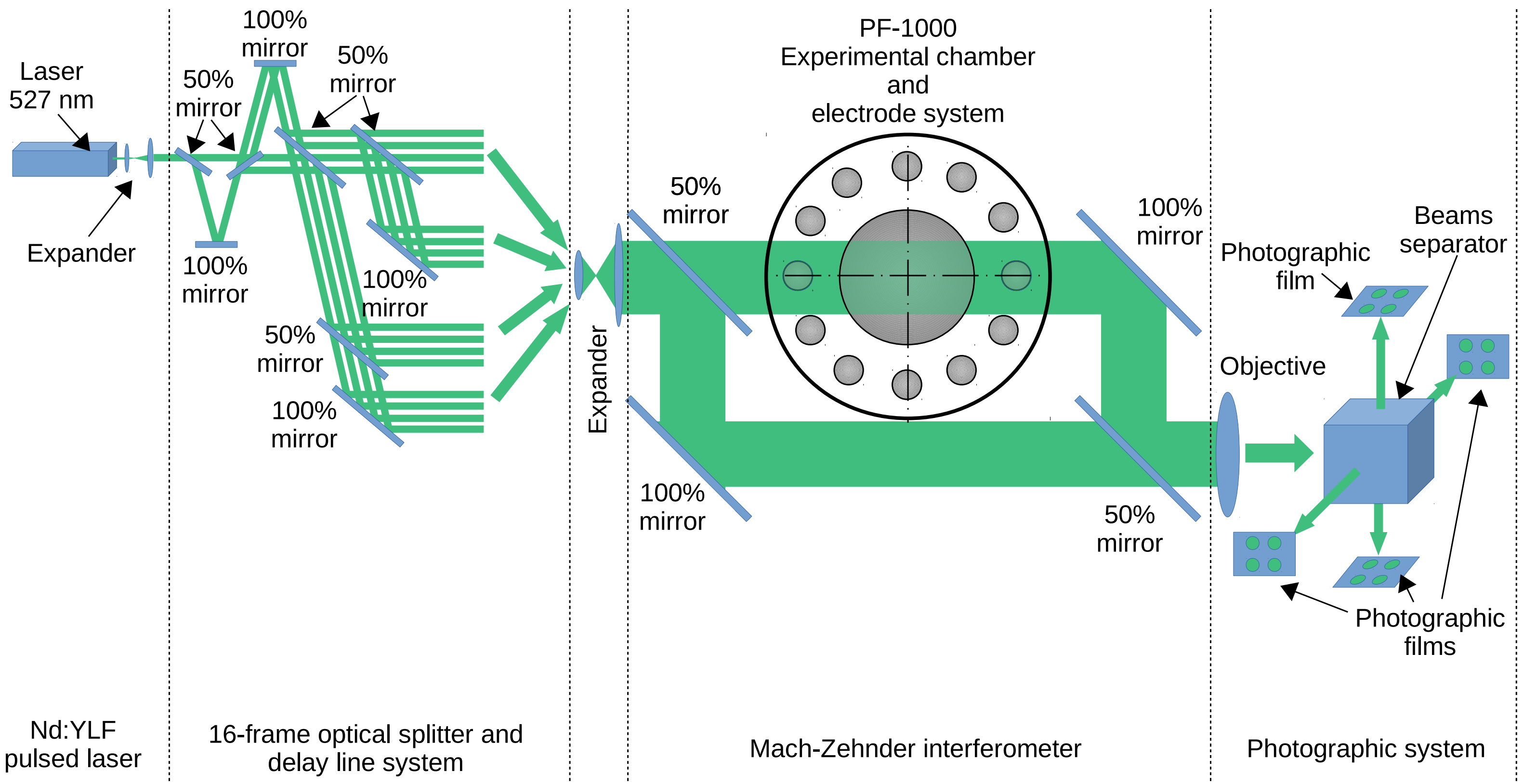

Figure 3.12: Scheme of 16-frame laser probing system based on Mach-Zehnder interferometer in experiments on the PF-1000 device [152].

Chapter 4

Experiments with Deuterium Gas Filling

This experiments represents the typical configuration of the plasma focus experiments where the standard Mather-type electrode system described in subsection 3.1.2 is used and the chamber is filled by the deuterium gas before the shot. These shots are important to have a reference for other experiments with a gas-puff load or a modified electrode system. For illustration, the time-integrated photo of the discharge №12858 in the visible light is shown in fig. 4.1.

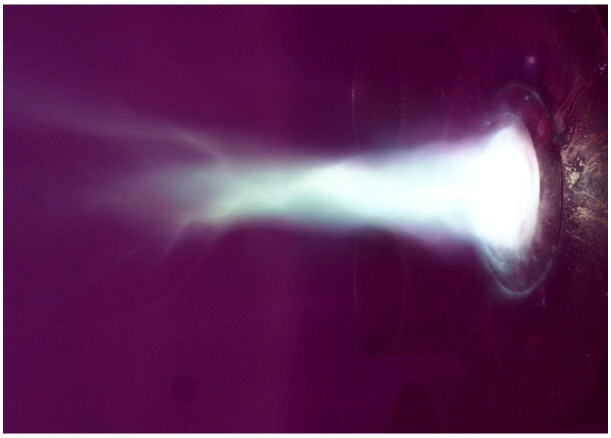

Figure 4.1: Time-integrate photo of the discharge №12858 in the visible light.

4.1 Experimental Setup

Before the shot, the experimental chamber is pumped to a high vacuum of about 10^{-3} Pa and then the chamber is filled by the deuterium gas with an absolute pressure of $100 - 300$ Pa. The capacitor battery is charged typically to the voltage of $(16 - 27)$ kV, thus the stored electrical energy corresponded to $(250 - 490)$ kJ. In this configuration, the discharge current varies between 1.3 and 2.5 MA.

4.2 Experimental Results

As a typical shot with the deuterium gas filling we present shot №8585. In this shot, the capacitors were charged to the voltage of 25 kV and the experimental chamber was filled by the deuterium gas with a pressure of 260 Pa. The current derivative, PIN-diode, and scintillation ToF detector normalized signals are displayed in fig. 4.2.

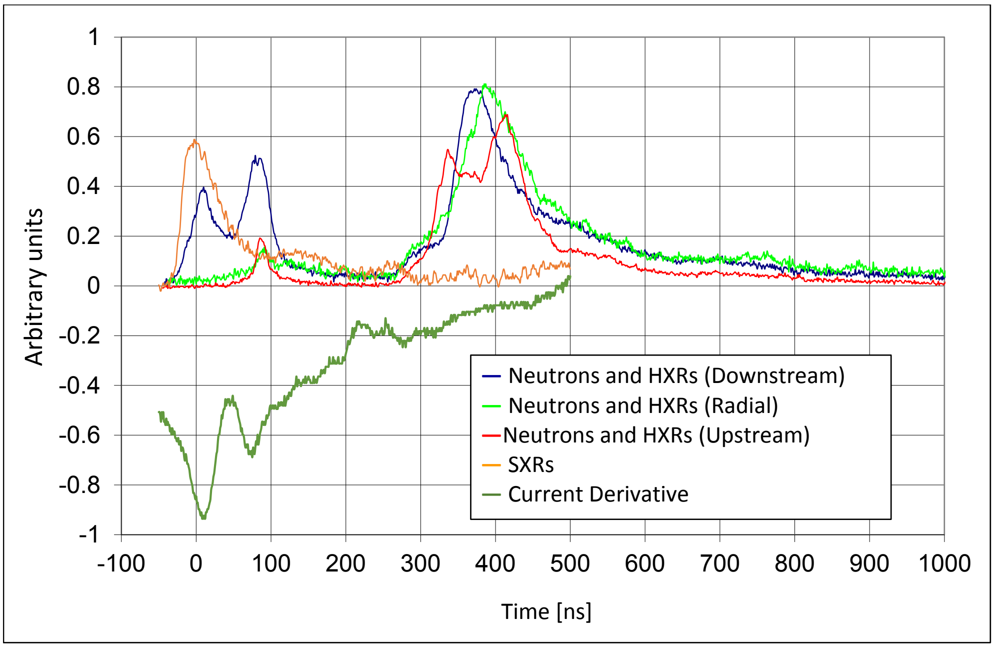

Figure 4.2: Shot №8585: The current derivative, PIN-diode, and scintillation ToF detector normalized signals.

In the fig. 4.2, the time of 0 ns correspond to the dip of the current derivative. It occurs when the pinched plasma is heated to the maximal temperature. At this time, the plasma is compressed to the minimal diameter before the stagnation phase when the instabilities with less diameter could appear. Each plasma instability disruption is accompanied by a local minimum of the current derivative. During the instability disruption a high electric field is induced by dI/dt and dL/dt which accelerates charged particles. The interaction of accelerated electrons with the anode generates the bremsstrahlung (HXR) pulse with a maximum in the upstream direction and detected by the scintillation time-of-flight detectors (we note that the signals in fig. 4.2 are normalized). Collisions of the accelerated deuterons led to the DD nuclear reactions and neutron emission with a maximum in the downstream direction. A total neutron yield in this shot achieved 1.2×10^{11}.

4.2.1 Interferometric Study

Using the Interferometry method described in subsection 3.2.4 the interferograms were converted to the two-dimensional densitograms for several times. Densitograms of the above mentioned representative shot №8585, processed by the computer numeric method of prof. Tadeusz Pisarczyk with a help of Dr. Tomasz Chodukowski is displayed in fig. 4.3. We note that the axial symmetry is assumed. As we can see in fig. 4.3, during the pinch phase from a time of -28 ns to the time of 52 ns, the electron density on the border of the plasma column is above 10^{23} m^{-3}. The diameter of such discharge plasma column is approximately 2 cm and a length of the plasma column grows with the time from of about 5 cm to 8 cm. The highest electron density in the center of the plasma column exceeds 10^{25} m^{-3}. A diameter of this dense region achieves about $1 - 2$ cm during the maximum of the compression. The length of this region is approximately 5 cm.

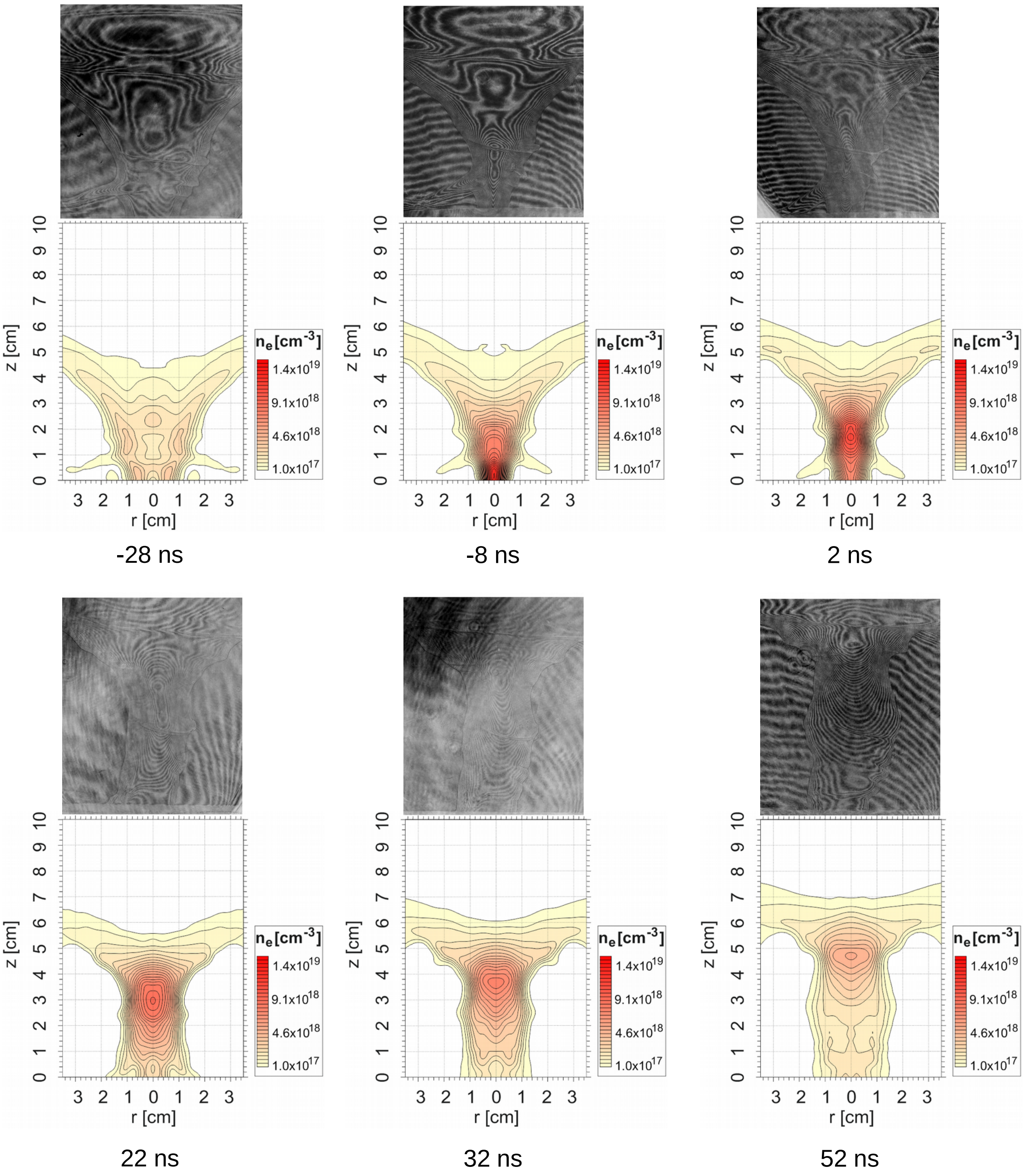

-28 ns -8 ns 2 ns

22 ns 32 ns 52 ns

Figure 4.3: Interferograms of the plasma implosion in the shot №10064.

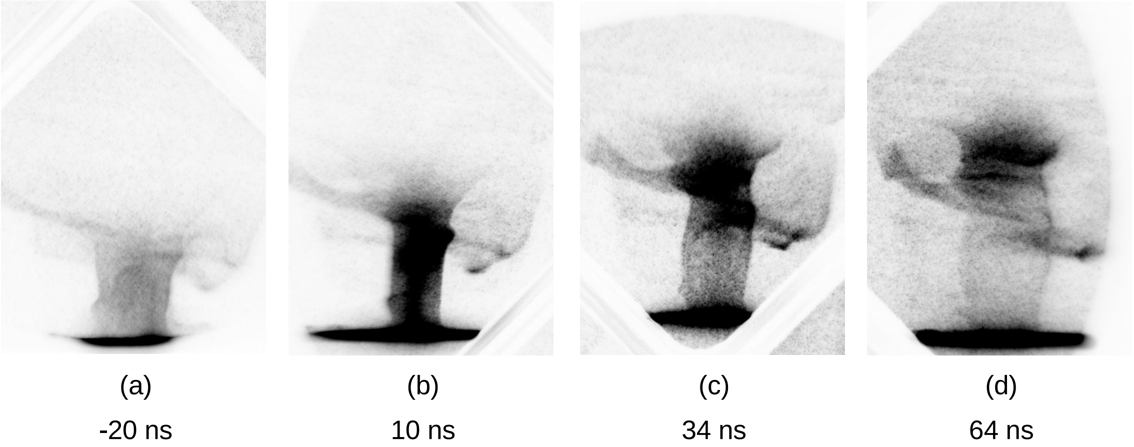

Figure 4.4: MCP pinhole camera image sequence in the SXR region of pinched plasma in the shot №12609.

4.2.2 MCP Pinhole Camera Images

To obtain SXR images with a nanosecond exposition time, the gated 4-frame MCP pinhole camera described in subsection 3.2.3 is used. The time sequence of the SXR images of the typical shot with the deuterium gas filling №12609 is displayed in fig. 4.4. In the shot №12609 the capacitor bank was charged to the voltage of 16 kV and initial pressure of the deuterium gas was 200 Pa.

4.3 Conclusions

On the PF-1000 device, the modern plasma diagnostic techniques with the high spatial and temporal resolution including the fast gated MCP SXR pinhole camera and the world unique 16-frame optical interferometer are established. Using this diagnostic techniques, it is possible to evaluate the time evolution of the electron density distribution and plasma dynamics.

These classical plasma focus experiments with the static gas filling and the flat-top anode can serve as the reference for the novel plasma focus configurations which are described in the following chapters.

Chapter 5

Experiments with Central Electrode Gas-puff

In contrast to the classical plasma-focus experiment, in which the pinched plasma is formed only by the gas of the static filling of the experimental chamber, in the experiments with the gas-puff the pinched plasma includes also a gas injected by a special gas nozzle.

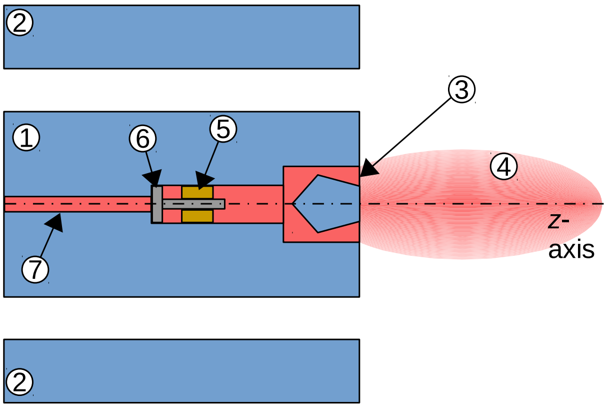

Figure 5.1: Arrangement of the shots with the central-electrode gas-puff. (1) Anode, (2) Cathodes, (3) Gas-puff nozzle, (4) Gas-puff, (5) Coil of the electromagnetic valve, (6) Poppet of the electromagnetic valve, (7) Gas-puff feed tube.

5.1 Experimental Setup

The supersonic gas nozzle is placed in the axis of the central electrode (anode). A shape of the nozzle is designed to achieve as low divergence of the gas-puff injection as is possible. The plasma focus electrode system with the central electrode gas-puff is schematically displayed in fig. 5.1.

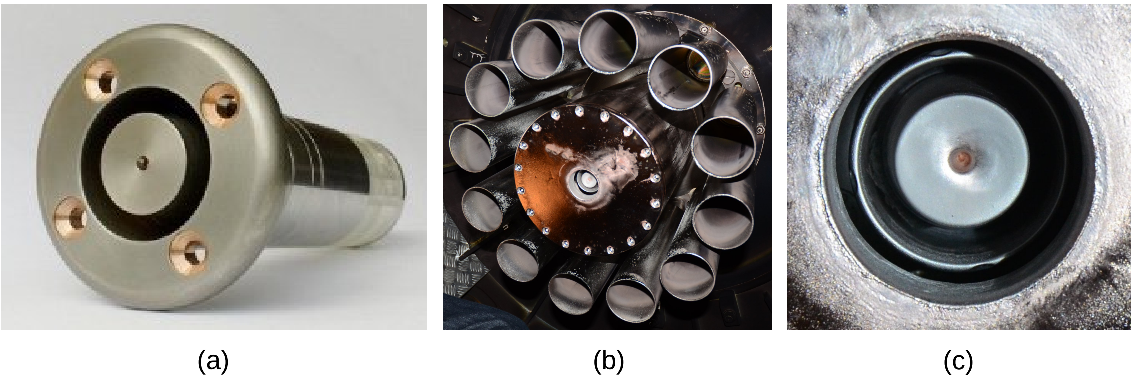
(a) (b) (c)

Figure 5.2: Fast electromagnetically driven gas-puff valve. (a) Overall view of the valve, (b) Electrode system with the valve, (c) Detailed view of the valve nozzle in the center of anode.

The gas-puff valve is based on an poppet which is driven by the magnetic field generated by the electric coil. The coil is supplied by a current pulse with an amplitude up to 20 kA. The gas-puff valve is triggered usually of about 2 ms before the trigger of the PF-1000 current generator. A pressure of the gas which is injected by the gas-puff valve is typically on the order of hundreds of kPa.

Overall view of the used gas-puff valve is shown in fig. 5.2(a) and photo of the electrode system with mounted valve are displayed in figs. 5.2(b) and 5.2(c).

The used gas-puff vale, developed on the Department of Physics of FEE CTU in Prague, is described in more detain in literature [159, 160].

Using this fast valve, four gas-puff load combinations were tested: a) deuterium gas filling and deuterium gas-puff, b) deuterium gas filling and neon gas-puff, c) neon gas filling and deuterium gas-puff, and d) neon gas filling and neon gas-puff.

5.2 Experimental Results

In total, 270 shots have been performed with various combinations of the gas filling (Deuterium, Hydrogen, and Neon) at a pressure in the range from 70 Pa to 200 Pa and gas-puff (Deuterium, Hydrogen, and Neon) at a pressure (30-200) kPa.

As the typical representative of the shots with the gas-puff, in this thesis, we present shot №9881. This shot was performed with the charging voltage of 23 kV and initial deuterium gas filling with the pressure of 200 Pa. The deuterium gas-puff valve pressured to 300 kPa was triggered 2 ms before the PF-1000 current generator trigger. In this shot, maximum of the discharge current achieved 2 MA. Signals of SXRs, HXRs, neutrons in the radial direction and current temporal derivative are shown in fig. 5.3. The zero time in the signals in fig. 5.3 correspond to the minimum of the current derivative. Usually in this moment the maximum of the plasma compression is assumed. We note, that the different cable lengths of detectors are taken into account in the plotted signals in fig. 5.3.

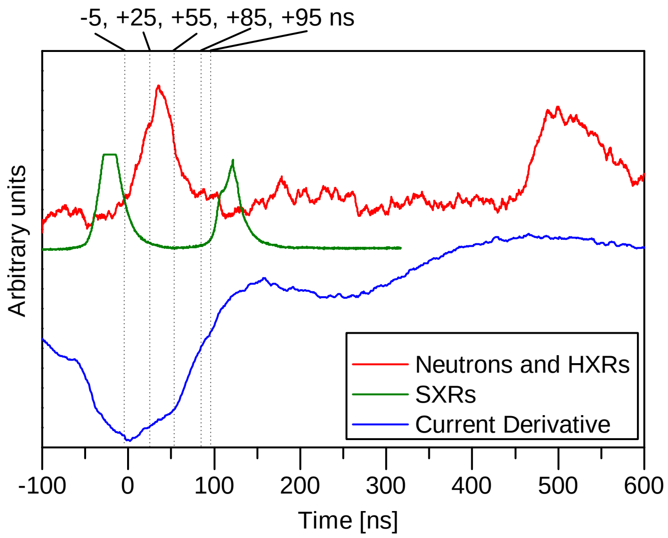

Figure 5.3: Shot №9881. Hard x-rays (HXRs) and neutrons measured by the ToF detectors (red line), soft x-rays (SXRs) of measured by the PIN diode (green line), and discharge current temporal derivative measured by the inductive coils (blue line).

As far as the neutron production is concerned, according to the silver activation detectors the total neutron yield is of about 4×10^{10}.

5.2.1 Interferometric study

Sequence of the interferometric images of the pinched plasma in the shot №9881 is shown in fig. 5.4. For a better orientation, the times of the interferometric images are marked in the signals in fig. 5.3. From the interferograms in fig. 5.4 the distributions of the electron areal density $N_e(x, y)$ are evaluated using the method presented in subsection 3.2.4. At the time of -5 ns the plasma column is shrinking to the z-axis. The maximums of $N_e(x, y)$ are near the plasma column boundary. At the moment of 25 ns (fig. 5.5(b)) the maximums of $N_e(x, y)$ on each z-level are transported to the axis of the pinched plasma column. Radii of the pinch column

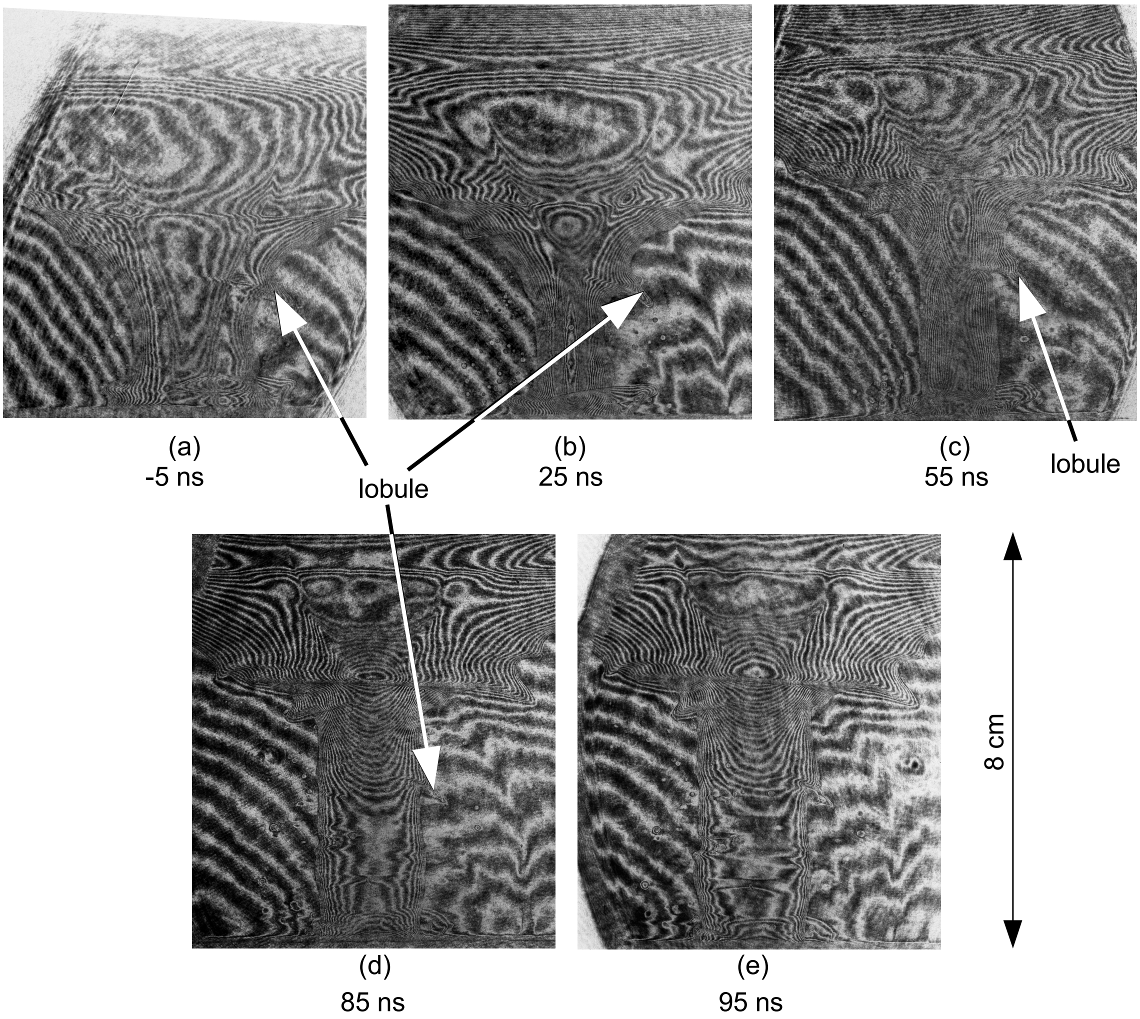

Figure 5.4: The interferometric images of the pinched plasma in the shot №9881.

diminishing along the whole z-axis. The zipper effect is well visible. The radii of

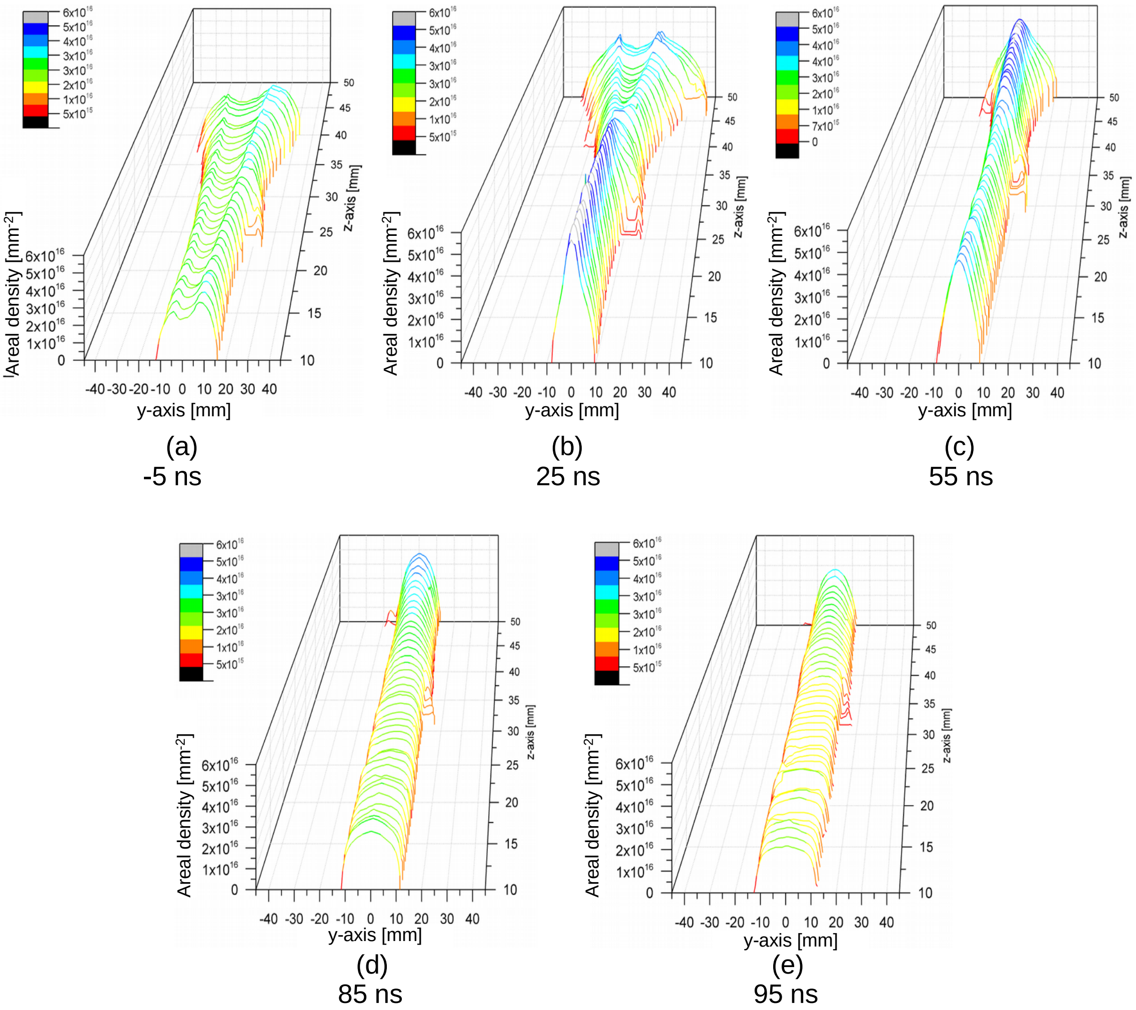

(a) -5 ns

(b) 25 ns

(c) 55 ns

(d) 85 ns

(e) 95 ns

Figure 5.5: Areal distribution of the electron density in the shot №9881.

the plasma column are slowly increasing at the lower values of z. For z = 1.5 cm the radius of the plasma column is 8 mm at 25 ns and 9 mm at 55 ns.

At the time of 85 ns and $z = 45$ mm (fig. 5.5(d)) the radius of the plasma column is still decreasing, while at $z = 40$ mm the radius of the column is already increasing. Maximums of $N_e(x, y)$ started decreasing along the all z-axis.

At the moment of 95 ns (fig. 5.5(e)) maximums of $N_e(x, y)$ continue decreasing along the all z-axis. It happens due to the dominant motion of the mass going along the z-axis to the umbrella shape of the dense plasma sheath. Time resolved linear electron density of plasma $\eta_e(z)$ curves are shown in fig. 5.6. At the lower values

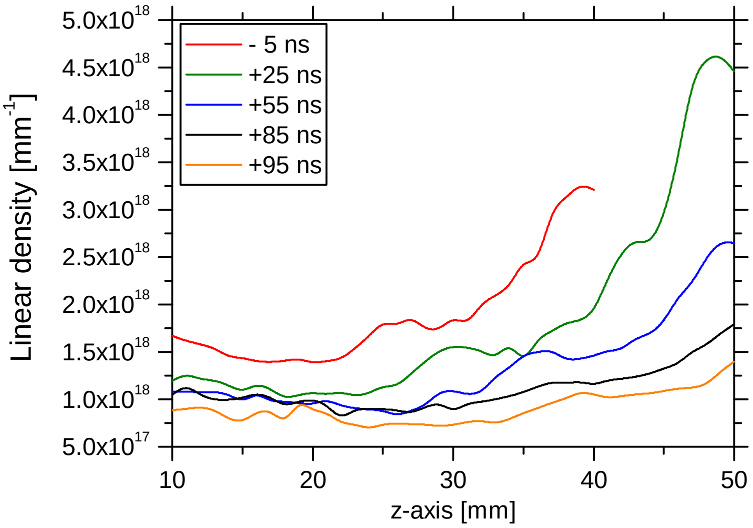

Figure 5.6: Temporal evolution of the linear electron densities in the shot №9881.

of the z-axis, the linear densities decreases with the time more slowly than at the higher values of the z-axis. Linear density decreases till the value of 8×10^{18} per cm with z in range 1.0 - 3.4 cm at the end of the observation. It is apparent from fig. 5.5 and fig. 5.6 that the mass is transported both in the axial and radial direction.

In fig. 5.6, at the time of -5 ns, we see a small peak in $z = 25$ mm. This peak is moved to $z = 30$ mm at the time of 25 ns and then to $z = 35$ mm at the time of 55 ns. It is caused by the lobule moving along the z-axis and transporting some amount of plasma. Here lobule is a kind of $m = 0$ or $m = 1$ instability, when the part of plasma prolapse out of the dense column, see fig. 5.4, also lobules are described in [164]. In this shot, the velocity of this axial motion of the lobule is about $(1.5 \pm 0.3) \times 10^5$ m/s (similar to the implosion velocity). The linear densities at –5 ns have higher values than at later times. This is explained by the effect of transport of plasma along the z-axis during its elongation.

As far as the radius in the maximum of the compression is concerned, in the case of the deuterium gas-puff and deuterium filling, the plasma was compressed typically to the diameter $(3 - 4)$ cm at the distance of about $z = 1.5$ cm during the phase of stagnation (before formation of the instabilities). In the case of deuterium gas-puff and deuterium filling, the electron density in this region reaches typically $(0.8 - 1.6) \times 10^{24}\mathrm{m}^{-3}$.

In the case of deuterium initial filling and neon gas-puff, the minimum plasma diameter during the stagnation and electron density of the pinched plasma were similar to the case of deuterium filling and deuterium gas-puff.

In the case of the neon initial filling and deuterium gas-puff, the plasma was usually pinched to the diameter of about 1 cm. It is 4 times smaller diameter then in the case of deuterium filling. Nevertheless, the electron density typically reaches about $1 \times 10^{24}\mathrm{m}^{-3}$, which is lower than typical electron density in the shots with the deuterium initial filling due to the strong zippering.

Since using the interferometer we obtain images of electron density distribution in 16 different times, it is possible to calculate the plasma implosion velocity. It seems that the implosion velocity is not significantly depended on the gas-puff configuration and it depends mostly on the gas of initial filling and its pressure. The typical implosion velocity in the shots with the deuterium filling with the pressure of 200 Pa is 1.5×10^5 m/s. Similar implosion velocity was reached with the neon initial filling with the pressure of 75 Pa. For deuterons, such an velocity corresponds to kinetic energy of about 0.25 keV. The energy of neon ions with the velocity of 1.5×10^5 m/s reaches approximately 2.5 keV, due to the tenfold higher mass in the comparison with deuterons.

5.2.2 MCP Pinhole Camera Images

Using the central electrode deuterium gas-puff the shots are relatively well reproducible. Thus, it is possible to connect images of the most sensitive frame of the MCP from several shots and obtain the time resolved sequence in SXR and EUV region. Such a sequence of the shots with 200 kPa initial deuterium gas filling and 150 kPa deuterium gas-puff is shown in fig. 5.7. Probably, the first think which we observe in the images in fig. 5.7 are the sharp and bright fibers - filaments. Such filaments have been observed only in the shots with the deuterium gas-puff and deuterium gas filling and deuterium gas-puff and neon gas filling. An origin of these filaments is not explained. Since due to the line emission the heavier elements emit more EUVs and SXRs than hydrogen, we assume that the filaments are caused by impurities in the gas-puff. It is probably remnants of atmosphere in the gas-puff valve. However, the interesting experimental result is that these impurities do not significantly affect the neutron yield. The average neutron yield in this configuration is about 6×10^{10}.

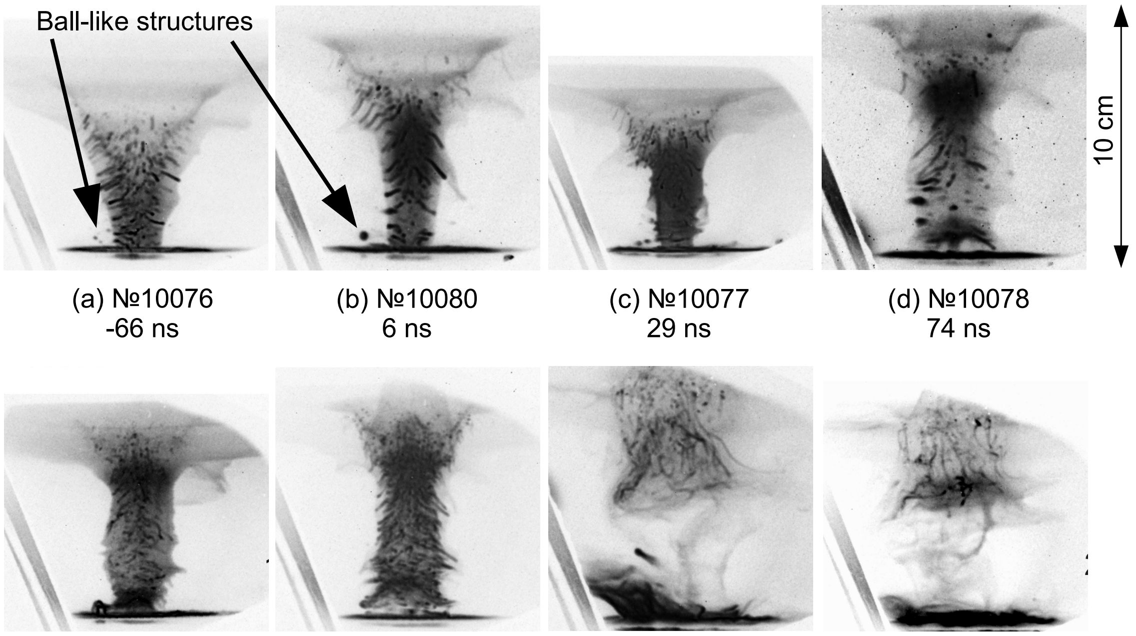

(a) №10076
-66 ns

(b) №10080
6 ns

(c) №10077
29 ns

(d) №10078
74 ns

(e) №10075
109 ns

(f) №10074
147 ns

(g) №10079
240 ns

(h) №10081
240 ns

Figure 5.7: UV/SXR images obtained using the MCP pinhole camera.

Analogously, the experiments with the neon gas-puff were performed. As well as in the experiments with the deuterium gas-puff, the shot reproducibility allows us to create the time sequence of the MCP images from several shots. For example, the sequence of shots with the initial deuterium gas filling with the pressure of 200 Pa and neon gas-puff with a pressure of 30 kPa is shown in fig. 5.8. As expected, in

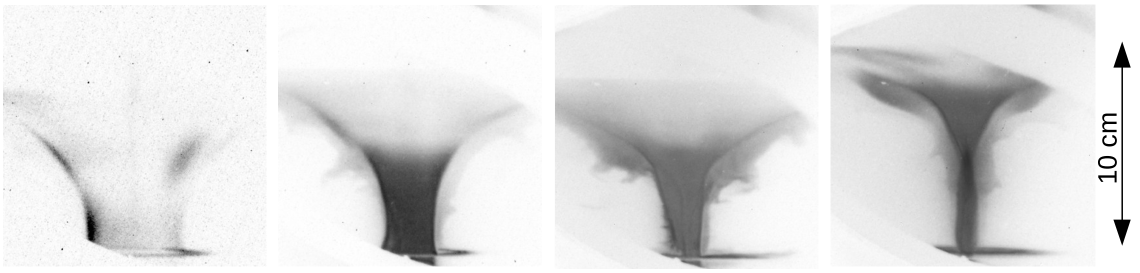

(a) № 10339
-147 ns

(b) № 10340
-63 ns

(c) № 10343
-16 ns

(d) № 10341
40 ns

Figure 5.8: EUV/SXR images obtained using the MCP pinhole camera.

the shots with the neon gas-puff, the MCP images are much better exposed than in the case of the shots with the deutrium only due to the line radiation. As we can see in fig. 5.8 the above mentioned bright filaments have not been observed. The reason is probably that the neon plasma emits a more intensive line radiation than the atmosphere admixtures. Assuming that the bright signal in the MCP images in fig. 5.8 is emitted by the neon plasma, it seems that the neon plasma is pinched to a relatively small diameter of about 1 cm during the current derivative minimum . At the later times, the neon plasma is pinched bellow the diameter of 1 cm and it stay stable for tens of ns (see fig. 5.8(d)).

Surprisingly, even it seems that in the center of the pinched plasma column is a significant amount of neon ions, the neutron yields achieved $(2-6)\times 10^{10}$. This relatively high neutron yield is approximately two times lower in comparison with the shots in the pure deuterium. A possible explanation of such neutron yields is that the neon is mixed with the deuterium.

5.2.3 Ball-like Structures

We have observed many shots with the ball-like structures which are visible on the MCP (see fig. 5.7) and interferometric images outside of the dense column. It was possible to observe these structures only in the shots with the deuterium gas-puff. The larger number of the ball-like structures was observed in the shots with $(66-80)$ Pa of the initial pressure of the neon initial chamber filling and 200 Pa of initial pressure of the deuterium filling and 150 kPa pressure of deuterium in the gas-puff [158].

We distinguish between big and small ball-like structures which differ in their diameter. The big ball-like structures with have a diameter of $(3-10)$ mm and small structures have a diameter of $(0.7-3)$ mm. A lifetime of the small ball-like structures is lower (from tens of ns to 150 ns) than the lifetime of the big structures which is usually $150-200$ ns, or more. All ball-like structures does not change their position during their existence, but their size and shape are changed.

5.2.3.1 Evolution of Small Ball-like Structures

In this subsection two shots with the deuterium gas-puff(№10125 with the neon initial filling and №10078 with the deuterium initial filling) with small ball-like structures are described.

Shot №10125

The signals of SXRs, HXRs, neutrons and voltage are shown in fig. 5.9. The interferometric frames of the evolution of the small ball-like structures are shown in fig. 5.10. Estimation of the electron density profiles of the first structure (which is signed as 1 in fig. 5.10) in different times are shown in fig. 5.11. Estimation of the electron density profiles of the second structure (which is signed as 2 in fig. 5.10) in different times are shown in fig. 5.12. The evolutions of the total number of electrons in the ball-like structures are shown in fig. 5.13.

The occurrence of the two small ball-like structures (which is signed as 1 and 2 in fig. 5.10) were noticed at the time of -62 ns. It is 10 ns before the beginning of the pinch stage at the time of -52 ns. These structures occurred in the region where the imploding plasma sheet had passed.

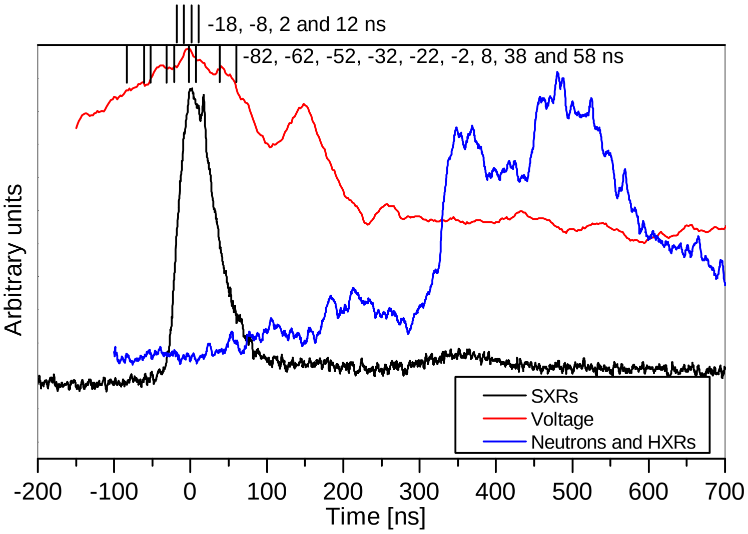

Figure 5.9: Signals of shot №10125: SXRs (black), HXRs and neutrons (blue) and voltage (red).

The diameter of the first structure (which is signed as 1 in fig. 5.10) is about 1.2 mm at the time of -62 ns and it is well visible till the moment of -32 ns, when the explosion of the constriction happened (fig. 5.10(b)). At that moment, the ball diameter increased up to 1.6 mm and the number of the fringes increased from 0.7 to 1.2. Structure is visible till the moment of 38 ns. At this moment, the diameter of the structure increased up to 3 mm and the number of fringes decreased till approximately 0.3. The lifetime of the structure was about 100 ns.

The maximum of the electron density in the center of the first structure is approximately 3.5×10^{24} m^{-3} (fig. 5.11) from the moment of -62 ns to -32 ns and it decreases till 1.3×10^{24} m^{-3} at the time of -22 ns. The electron densities are not estimated after -22 ns because the boundaries of the structure in the interferometric images are poorly visible. The number of the fringes of approximately 0.5 or less causes a big inaccuracy in the electron density evaluation. The inaccuracy of the calculations also depends on the choice of the geometric boundaries of the structures and it is about 20%.

The value of the total number of electrons in the first structure increases from 1.1×10^{15} to 2.2×10^{15} to the moment of -32 ns and decreases at the time of -22 ns till 1.2×10^{15}.

The second structure (fig. 5.10, signed as 2) achieved 1 mm of the diameter at

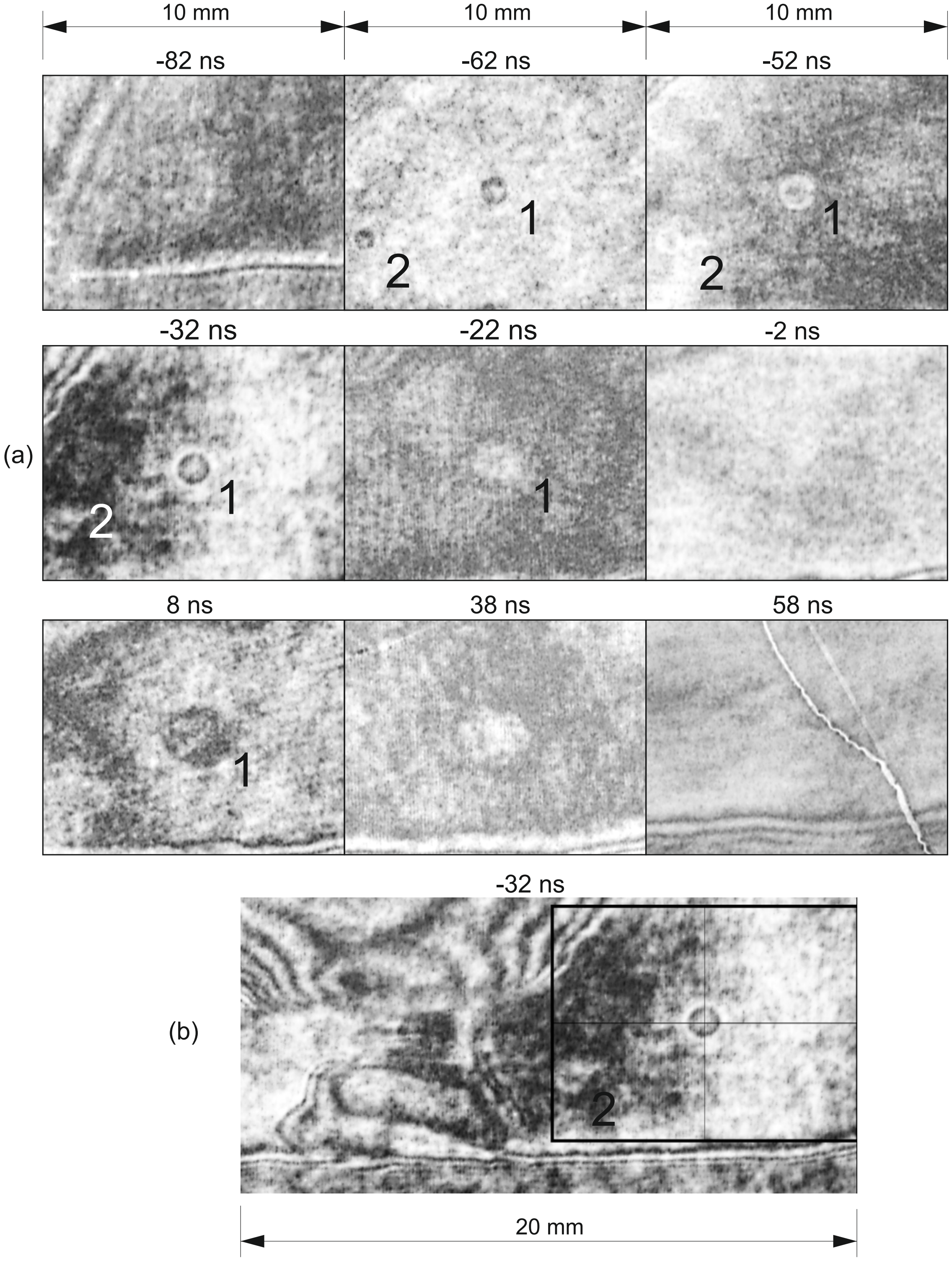

Figure 5.10: Interferometric images of shot №10125:(a) evolution of the ball-like structure from the beginning to the end of its existence, (b) view on the plasma column and ball-like structure at the time of -32 ns.

the time of -62 ns. At this moment the number of fringes is 0.7. Structure was visible till the moment of -32 ns, when the explosion of the constriction happened. At this moment the diameter of the structure increased up to 1.2 mm and the number of fringes did not change. The lifetime of the structure was of about 30 ns.

The maximum of the electron density in the center of the second structure is approximately 7.5×10^{24} m^{-3} (fig. 5.12) at the moment of from -62 ns to -52 ns. It decreases till 2.8×10^{24} m^{-3} at the end of the existence at the time of -32 ns.

The value of the total number of electrons in the second structure equals to approximately 0.7×10^{15} at the time from -62 ns to -32 ns. The structure is too small and it's lifetime is too short for making statistics of the total number of electrons.

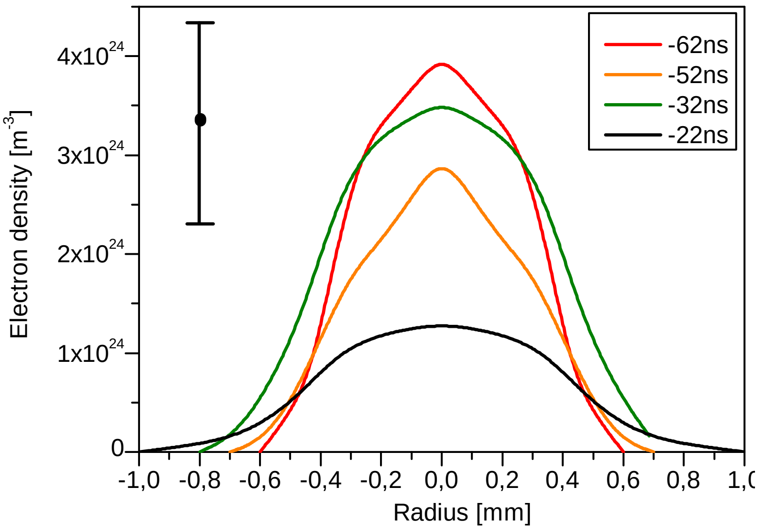

Figure 5.11: Shot №10125. The electron density profiles of the small ball-like structure, which is signed as 1 in fig. 5.10, in different times.

These structures started to decay at the moment of the explosion of the constriction at the time of -32 ns (fig. 5.10(b)). The decaying of the second structure which is closer to the pinch column started earlier. The first structure continues to decay at the later times from -2 ns to 38 ns (fig. 5.10(a)).

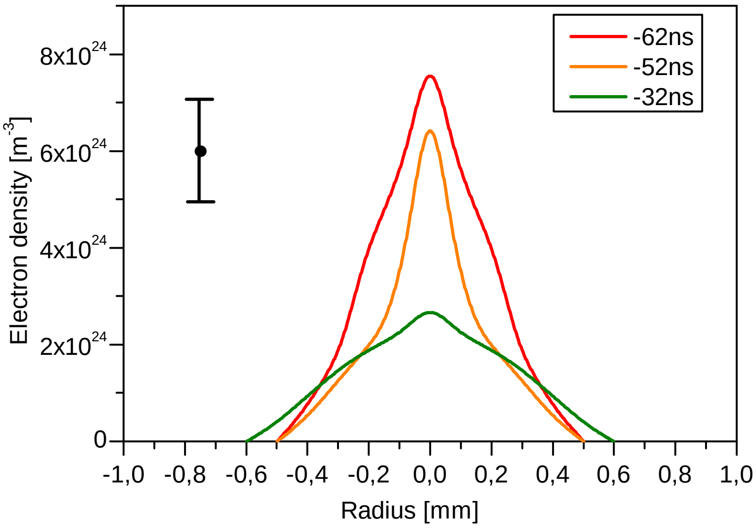

Figure 5.12: Shot №10125. The electron density profiles of the small ball-like structure, which is signed as 2 in fig. 5.10, in different times.

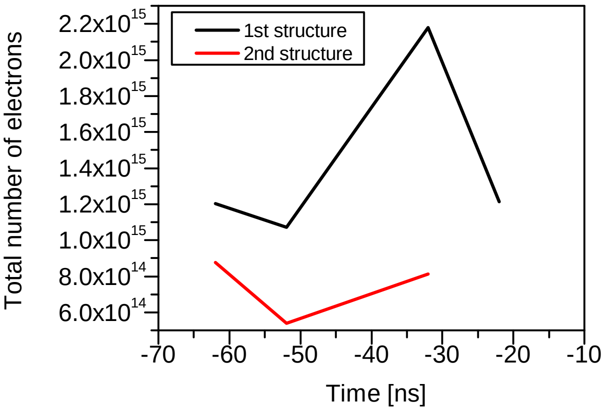

Figure 5.13: Shot №10125. The evolution of the total number of electrons in ball-like structures, which is signed as 1 (black) and 2 (gray) in fig. 5.10.

Shot №10078

In shot №10078 we observed small ball-like structure (fig. 5.14) near the dense plasma column (from -45 to 95 ns) which appeared in the region where the imploding plasma sheet had passed. The structure has the ideal spherical symmetry from the time of -45 ns (with the diameter of 1.4 mm) to 15 ns (with the diameter of 1.9 mm) after which it started to transform to ellipse which is well seen at the time of 45 ns.

Also, the surface of the expanding dense plasma column is closer to the structure than in the earlier times. Next 50 nanoseconds from the moment of 45 ns to 95 ns the structure gradually disappears on the backgraound of the dense plasma column. Probably, after a time of 95 ns the structure disappeared or it is absorbed by the expanding column of the dense plasma.

The lifetime of the structure is about 140 ns.

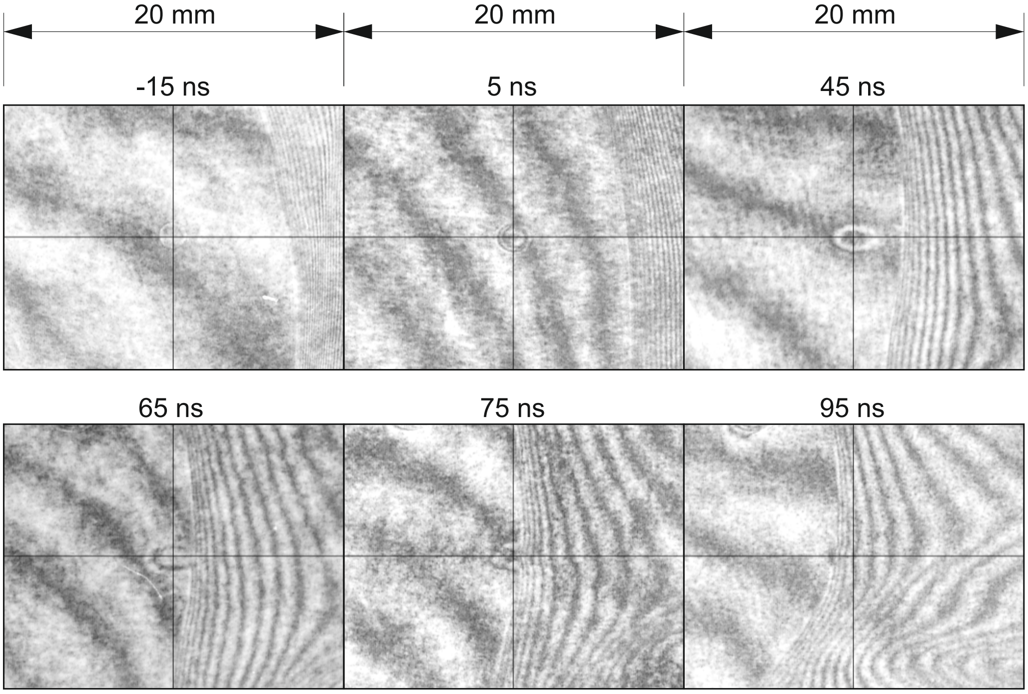

Figure 5.14: Shot №10078. Interferometric frames of the evolution of the ball-like structure.

5.2.3.2 Evolution of Big Ball-like Structures

In this chapter three shots (№10122, №10099, and №10125 with the neon filling of the chamber) with the big ball-like structures are presented.

Shot №10122

The bigger ball-like structure is observed in shot №10122. The signals of SXR, HXR, neutrons and voltage probe are shown in fig. 5.15. In fig. 5.16 the interferometric and EUV frames are shown. The interferometric frames of the evolution of the structure is shown in fig. 5.17. The electron density profiles of the structure are shown in fig. 5.18. The evolution of the total number of electrons in ball-like structure is shown in fig. 5.19.

The occurrence of the ball-like structures (fig. 5.17) was noticed at the time of −90 ns. It is 40 ns before the beginning of the pinch stagnation at the time of −50 ns. This structure occurred in the region where the imploding plasma sheet had passed. The distance of the ball-like structure from the pinch axis, which is estimated from EUV and interferometric frames, is approximately 47 mm.

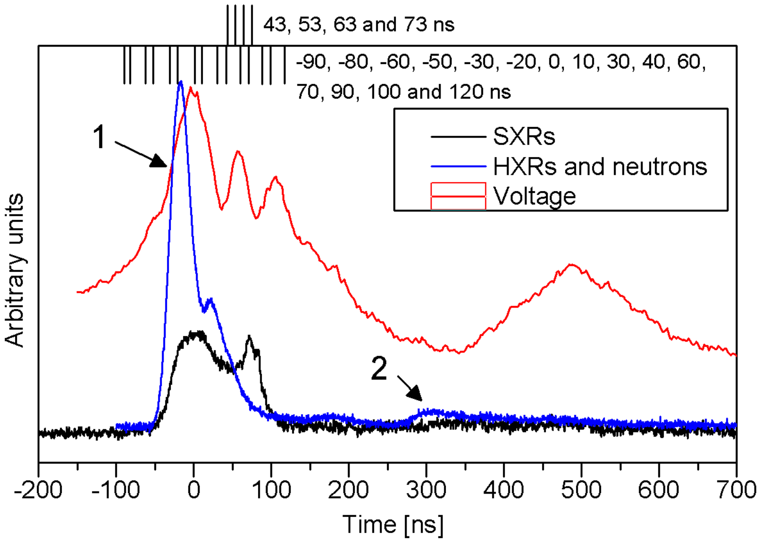

Figure 5.15: Shot №10122. Signals of SXR (black), HXR (blue, which is signed as 1), neutrons (blue, which is signed as 2) and voltage probe (red)

The diameter of the ball-like structure (fig. 5.17) is 1.9 mm at the time of -90 ns. During next 180 ns at the time from -90 ns to 90 ns the diameter of the structure grows up to 6 mm, the number of fringes gradually increased from 0.5 to 4.5-5 and fringes appears in the central chaotic round field without fringes. Later, at the time from 90 to 100 ns it is not able to determine the diameter correctly, because of the background plasma of expanding dense plasma column. The number of fringes

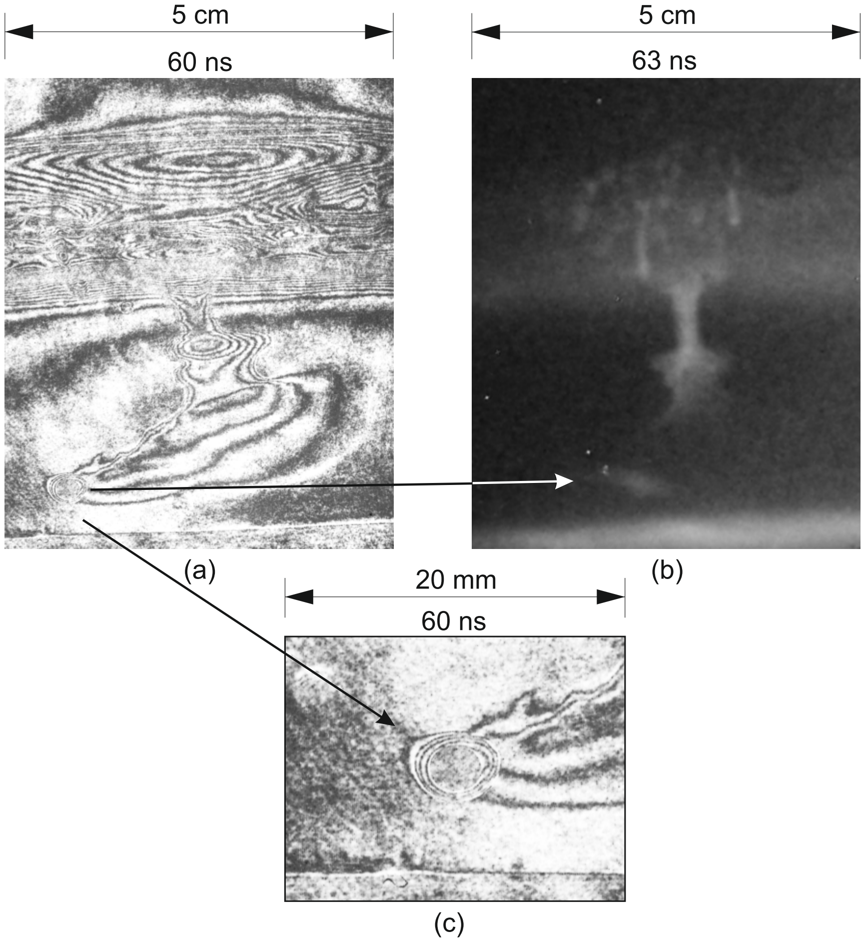

Figure 5.16: Shot №10122. Interferometric (a) and EUV frames (b) and detailed picture of ball-like structure (c).

rapidly increased to almost 9. And then, during the last 20 ns the structure started to gradually decay and the shape of the fringes transformed to more unsymmetrical forms. The diameter continues to increase and reaches the value of about 6.2 mm. The number of fringes started to decrease. At the time of 120 ns it seems that the structure interacts with the expanding dense plasma column.

The maximum of the electron density in the center of the structure is approximately 2×10^{24} m^{-3} (fig. 5.18) at the time of -30 ns. Later, at the time from -20 to 100 ns the electron density gradually increases up to 11×10^{24} m^{-3}. During last 20 nanoseconds of the observation, the maximum of the electron density decreased to 6×10^{24} m^{-3}.

The value of the total number of electrons in the structure increases from the moment of -90 ns to 100 ns from 0.5×10^{17} to 3.8×10^{17} and decreases till 3.2×10^{17} at the time of 120 ns.

We do not know the electron density in the central part exactly because of the structure's inner part without fringes, therefore we assumed the values of the electron densities for this region equal to the boundary values of electron densities of the structure. The uncertainty of that calculation is of about 20%.

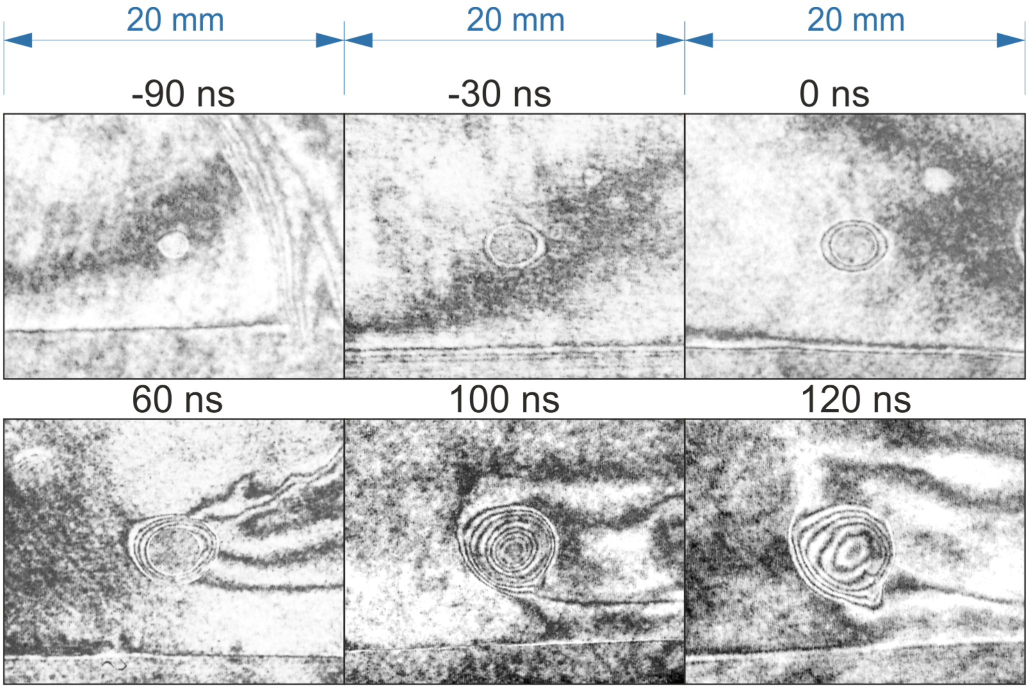

Figure 5.17: Shot №10122. Interferometric frames of the evolution of the ball-like structure.

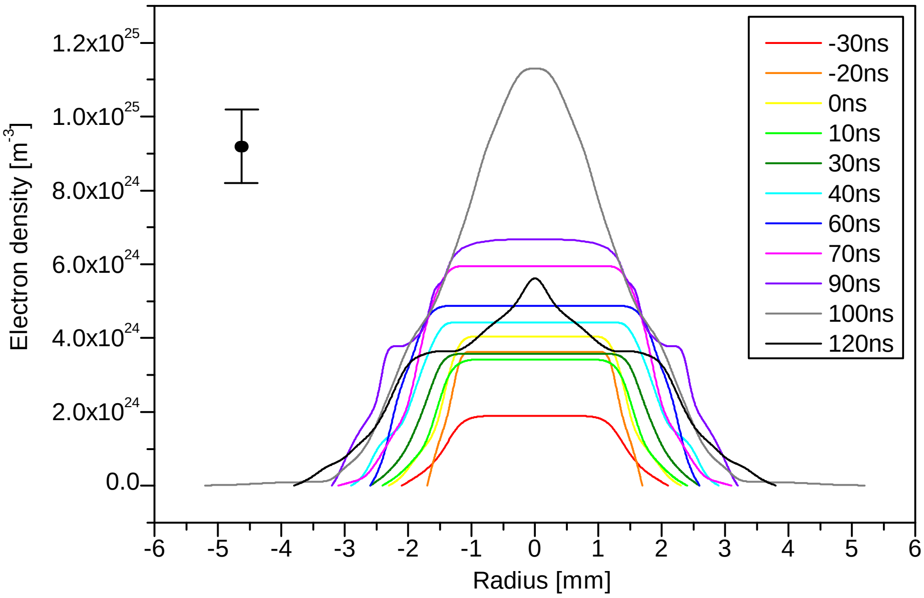

Figure 5.18: Shot №10122. The electron density profiles of the ball-like structure in different times.

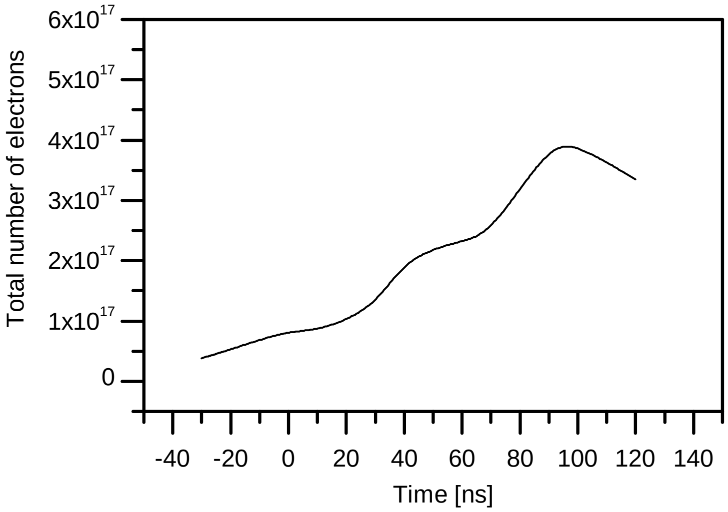

Figure 5.19: Shot №10122. The evolution of the total number of electrons in ball-like structure.

Shot №10099

The signals of SXR, HXR and voltage probe are shown in fig. 5.20. In fig. 5.21, the interferometric and EUV frames are shown. The electron density profiles in different times are shown in fig. 5.22.

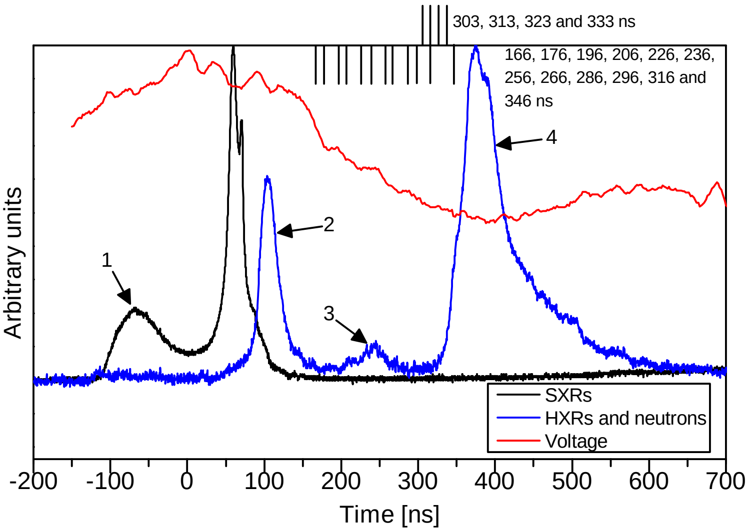

Figure 5.20: Shot №10099. Signals of SXR (black), HXR (blue, signed as 2), neutrons (blue, which is signed as 3, produced during first SXR pulse, and second neutron pulse, which is signed as 4, produced during first HXR pulse, which signed as 2) and voltage probe (red).

The interferometric pictures of the ball-like structure (fig. 5.21) were registered during it's decay after the time of the SXR, HXR and neutron pulses (from 166 to 376 ns).

The diameter of the structure (fig. 5.21) is 9 mm at 166 ns. At this time the the central part of the structure is very unsymmetric. May be it is the result of the coalescence of the two smaller structures. During next 210 ns from the time of 166 ns to 376 ns the diameter of the structure grows up to 12 mm. The number of fringes gradually decreases from 6 to 1.5. Due to the high emission of EUV the structures could have high temperature (fig. 5.21 at 333 ns.).

The maximum of the electron density in the center of the structure is approximately 6×10^{24} m^{-3} (fig. 5.22) at the time of 166 ns. At the moment of 196 ns it increases up to 10^{25} m^{-3}. The diameter increased until 10 mm. Later at the tine from 196 to 376 ns electron densities gradually decrease till approximately 1.3×10^{24} m^{-3}.

The value of the total number of electrons in the structure gradually decreases from 4×10^{17} to 2.3×10^{17} from the moment of 166 ns to 376 ns.

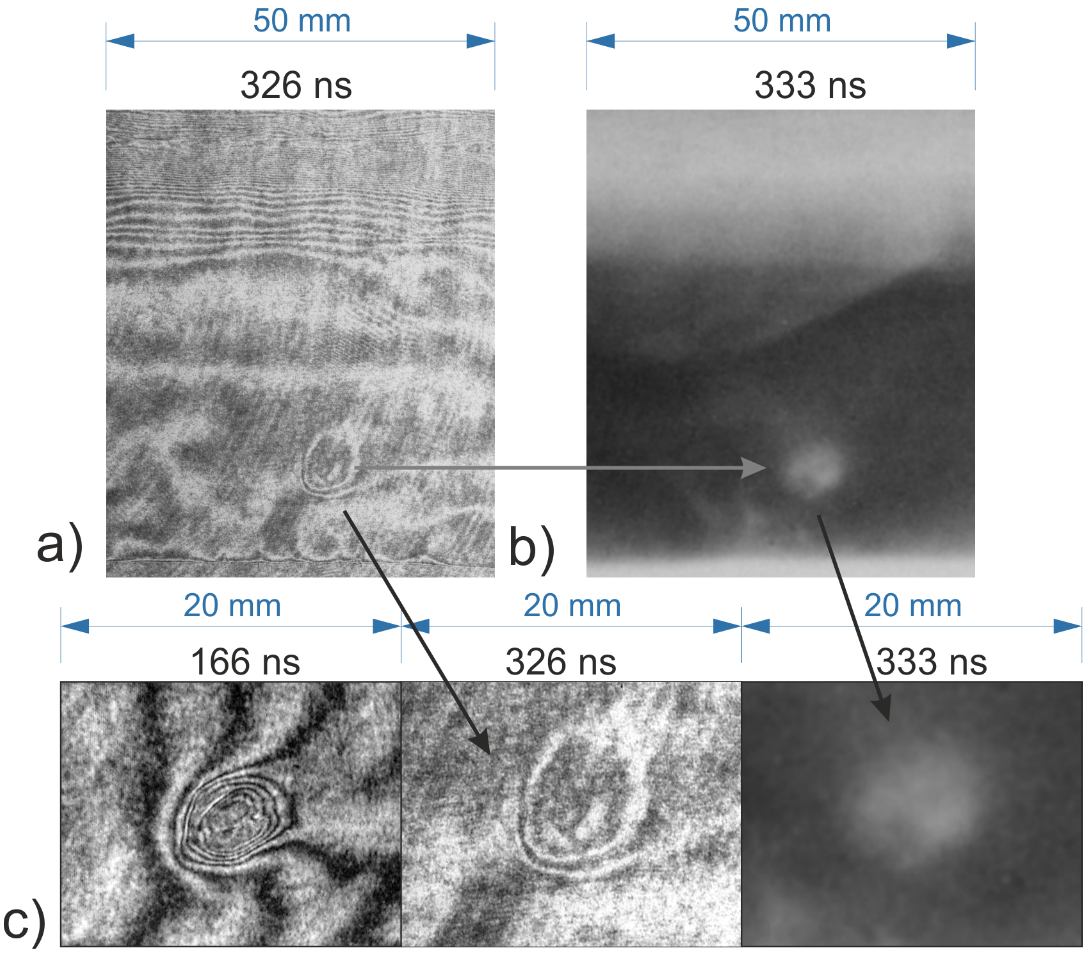

Figure 5.21: Shot №10099. Interferometric (a) and EUV frames (b) and detailed pictures of the ball-like structure (c).

This structure could exist for such a long time, because the two ball-like structures are coalesced (fig. 5.21) without an influence of the pinching column. There is also seen the plasma flowing through the low density plasma.

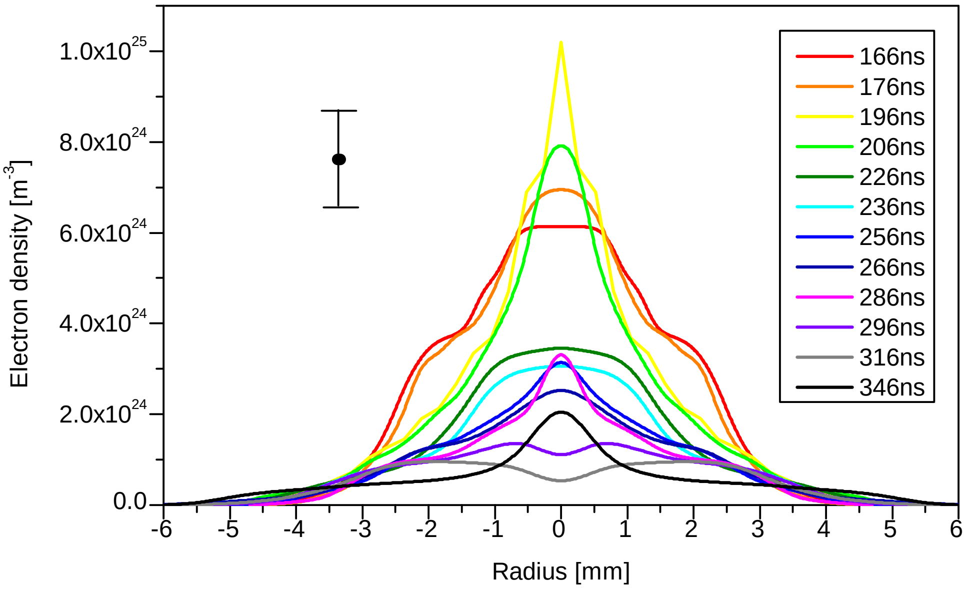

Figure 5.22: Shot №10099. The electron density profiles at the different times.

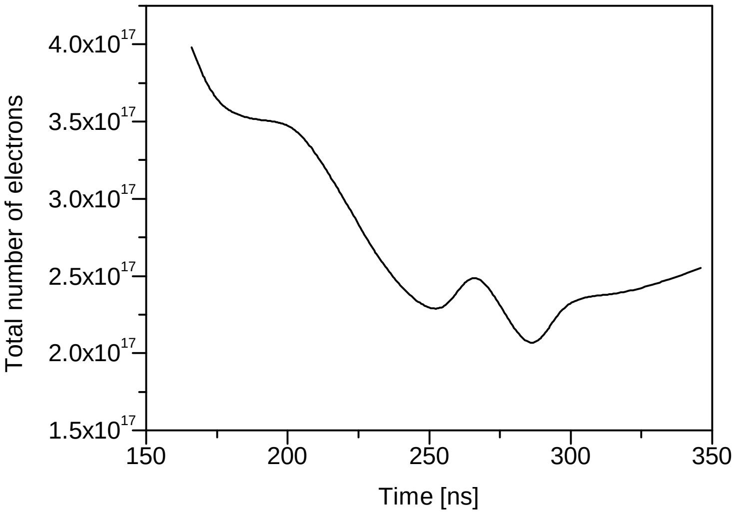

Figure 5.23: Shot №10099. The evolution of the total number of electrons in ball-like structure.

Shot №10125

Some of the structures could appear in near the plasma sheet or near it. The example is the shot №100125. In fig. 5.24, the interferometric and EUV frames are shown.

The interferometric frames of the evolution of the ball-like structure are shown in fig. 5.25.

The first ball-like structure (which is signed as 1 in fig. 5.25) in the area of umbrella-plasma sheet was detected at the time of -152 ns (90 ns before the stagnation phase). The diameter of the structure is 2.1 mm. The second structure with the diameter of 1 mm was observed at the time of -142 ns. From the time of -112 ns to -62 ns the diameters increased to 1.8 mm and 1.1 mm for the first and the second structure respectively. At this moment the first structure was observed out of the area of the umbrella-plasma sheet. At the time of −52 ns, the third structure with the diameter of 0.7 mm was observed. At the moment of 8 ns, all three structures are out of the umbrella-plasma sheet. Their diameters are 3.1, 1.8 and 1.4 mm for the first, the second and the third structures respectively. All these structures are visible on the interferometric frames till the end of the observation at 58 ns. At this moment, the diameters of the structures are 3.1, 2.7 and 1.8 mm.

During the whole time of the observation, the central part was chaotic and it did not changed. Taking into account that there is no information about the future evolution of structures, all of these structures could be estimated as big structures, because they have a big diameter and a long lifetime. All three structures are seen on the EUV frames at the moment of 12 ns, hence, all of them could have high temperature.

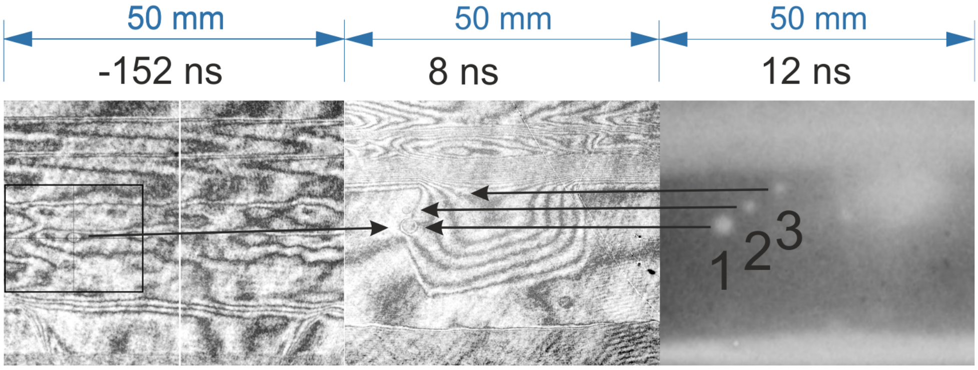

Figure 5.24: Shot №10125. Interferometric and EUV frames of the pinch column with the ball-like structures.

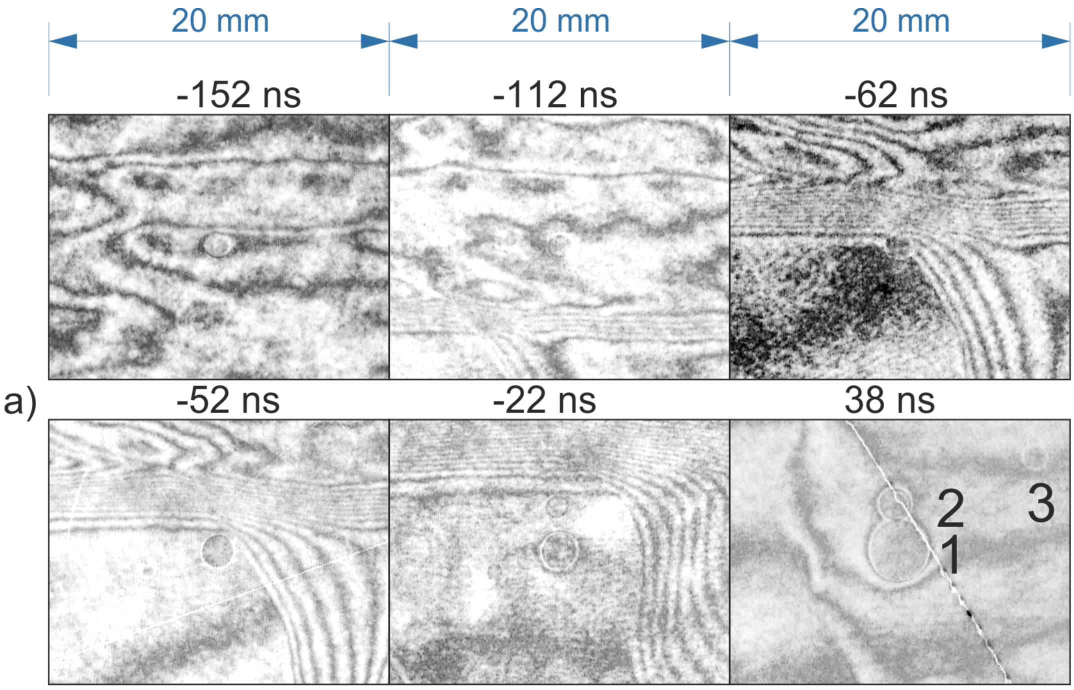

Figure 5.25: Shot №10125. Interferometric frames of the evolution of the ball-like structure.

5.2.4 Summary of the ball-like structure's properties

The conclusions are summarized as follows:

1. The evolution of ball-like structures could be divided into two phases:
   - **a)** phase of increase,
   - **b)** phase of decay.
2. The ball-like structures could appear in the regions where the imploding plasma sheet has passed or it appear without the external influence during the stagnation phase of the plasma column.
3. During the 1st phase (30 ns - 200 ns) the diameter of the ball-like structures increases. The number of fringes could increase from 1 to about 10. The electron densities are above 10^{24} m^{-3} and reach up to 1.1×10^{25} m^{-3}. The total number of electrons increase and it depends on the size of each structure.

During the 2nd phase (30 ns - 200 ns) the diameter of the ball-like structures continues increasing. The number of fringes decreases. The electron densities decrease and the total number of electrons decreases as well.

The mean lifetime of the ball-like structures is from several tens of nanoseconds to 200 ns or more.

4. The velocity of the expansion of the ball-like structures is approximately $(3-20) \times 10^4$ m/s.
5. The ball-like structures does not change their position in relation to the anode face (in visible inaccuracy ±0.3 mm).
6. The ball-like structures probably have the higher temperature, because they were observed in EUV frames.
7. The ball-like structures could decay during the constriction explosion of disappear without the visible external influence or disappear in the expanding dense plasma column.

The central chaotic part of the big ball-like structures without fringes is supposed to be turbulent with the same electron density as the density of the boundary layer.

The plasma mass could flow between the ball-like structure and the surrounding plasma.

The higher electron density and electron temperature induce the higher plasma pressure in the ball-like structure than in the surrounding plasma. Consequently, this higher pressure can be explained by the pinch pressure of the current flowing around the ball-like structure.

Small Ball-like Structures

Some small ball-like structures appear in the regions where the imploding plasma sheet has passed. In another shots with the deuterium filling in the chamber we observed a big amount of the small ball-like structures. In that shots some of the structures appeared without the visible external influence in low density plasma during the stagnation phase of the dense plasma column.

During the 1st phase of the small ball-like structure evolution (30 ns - 70 ns) the diameter increases from the value of about 1 mm to 2 mm. The number of fringes could increase from about 1 to 1.5. The maximums of electron densities is approximately $(3 - 8) \times 10^{24}$ m^{-3}. The total number of electrons increase up to approximately 2×10^{15} and it depends on the size of each structure.

During the 2nd phase (30 ns - 70 ns) the diameter increases up to the value of 3 mm. The number of fringes decreases. The maximums of electron densities decreases and the total number of electrons decreases too.

The mean lifetime of the ball-like structure is from several tens of nanoseconds to 150 ns.

These structures could decay during the pinched plasma constriction explosion, without external influence or in the stagnating pinch column.

Big Ball-like Structures

The big ball-like structures could appear in the regions where the imploding plasma sheet has passed. During 1st phase of the big ball-like structure evolution (100 ns - 200 ns) the diameter increases from the value of (1 - 2) mm up to (6 - 9) mm. The number of fringes could increase from 0.5 to 9 - 10 until the central chaotic part be filled by fringes. The maximums of electron densities increase up to approximately $(5 - 11) \times 10^{24}$ m^{-3}. The total number of electrons increase up to approximately 4×10^{17} and it depends on the size of each structure.

During 2nd phase (100 ns - 200 ns) the diameter could increase up to the value of 6 - 12 mm. The number of fringes decrease. The maximums of electron densities also decrease. The total number of electrons decreases too.

The mean lifetime of the big ball-like structure is (150 - 200) ns or more.

The plasma mass could flow between the ball-like structure and the dense plasma column or to the low density plasma in the surrounding area, which we observe in shot №10078, when the structure transformed to ellipse at 45 ns (fig. 5.14), or in shot №10122 at the time of 100 ns, when the total number of electrons decreased after the structure started to be influenced by expanding pinch column (fig. 5.17), or in shot №10099, when the plasma mass flows to the surrounding area (fig. 5.21).

There was able to calculate the mean velocity of radius enlargement of the structures and it was approximately $(3 - 20) \times 10^4$ m/s. The big ball-like structures could decay in the dense pinch column (fig. 5.16) or disappear without the external influence (fig. 5.21).

5.3 Conclusions

The plasma focus experiments with the deuterium gas filling and deuterium gas-puff, deuterium gas filling and neon gas-puff, neon gas filling and deuterium gas-puff, and neon gas filling and neon gas-puff were performed. In these experiments, various combinations of the initial gas filling pressure and gas-puff pressure were tested.

The plasma was investigated by optical 16-frame interferometer, gated EUV/SXR MCP pinhole camera, SXR PIN diodes, scintillation HXR and neutron ToF detectors, and silver activation neutron counters.

The axial and radial transport of the mass in the plasma column were evaluated, radial plasma mass moving is demonstrated and velocities of transporting of plasma mass along the z-axis were investigated.

Using the interferometric and MCP diagnostics we observed, that the gas-puff discharges are more stable than the usual plasma focus discharges without gas-puff. The higher stability of the plasma column could explain the longer SXRs emission measured by PIN diodes (of about 40% longer emission of SXRs in comparison with the shots without the gas-puff).

In the MCP images we observe a bright radiation in the center of the pinched plasma in the shots with the deuterium gas initial filling and the neon gas-puff. It indicates a presence of a significant amount of neon in the pinched plasma. In these shots, the average neutron yield of 4×10^{10} was achieved. This value is lower than in the experiments without the gas-puff, however not much. Thus, it seems that the neon is mixed with the deuterium but it does not affect the neutron production or that the neutrons are significantly produced by reactions on a greater diameter than the diameter of the imploded neon plasma.

As fare as the shots with with the deuterium gas-puff and deuterium gas initial filling are concerned, a 20% increase of the average neutron yield was reached in comparison with the shots without the gas-puff.

In the shots with the deuterium gas-puff, bright and sharp linear filaments were observed. These filaments have never been observed in the shots wihtout gas-puff or in the shots with neon gas-puff.

In the gas-puff plasmafocus experiments a relative stable ball-like structures have been observed and investigated. Results of these experiments are published in papers [158, 163, 164, 165, 166, 167, 168].

Chapter 6

Experiments with Central Electrode Cone

In this chapter, experiments with the novel electrode configuration are described. At plasma foci, the influence of the central electrode shape on the plasma dynamics and neutron yield was theoretically predicted and experimentally tested in USA [169]. In [169], the flat-top and hemispherical anode are used. In our experiments, the central anode has a form of cone.

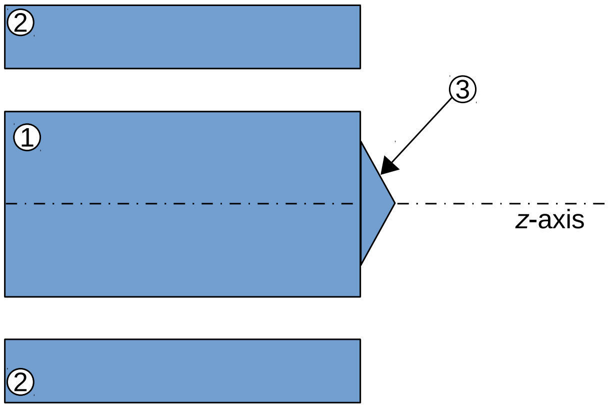

Figure 6.1: Arrangement of shots with the central-electrode cone. (1) Anode, (2) Cathodes, (3) Cone.

6.1 Experimental Setup

The copper cone with a diameter of 10 cm and height of 2 cm was coaxially placed on the flat surface central anode with the diameter of 23 cm. On the top of the cone is a hole with a diameter of 1 cm. For clarity, the scheme of the electrode system is shown in fig. 6.1 and photo of the electrode before and during the discharge №12055 (the filaments are visible there) is displayed in fig. 6.2. The series of 50 experimental shots with the central electrode cone was performed with the charging voltage of 16 kV corresponding to 250 kJ of stored energy in the capacitor battery. The discharge current maximum reached about (1.1 – 1.3) MA. The initial pressure of the static deuterium gas filling was 100 Pa.

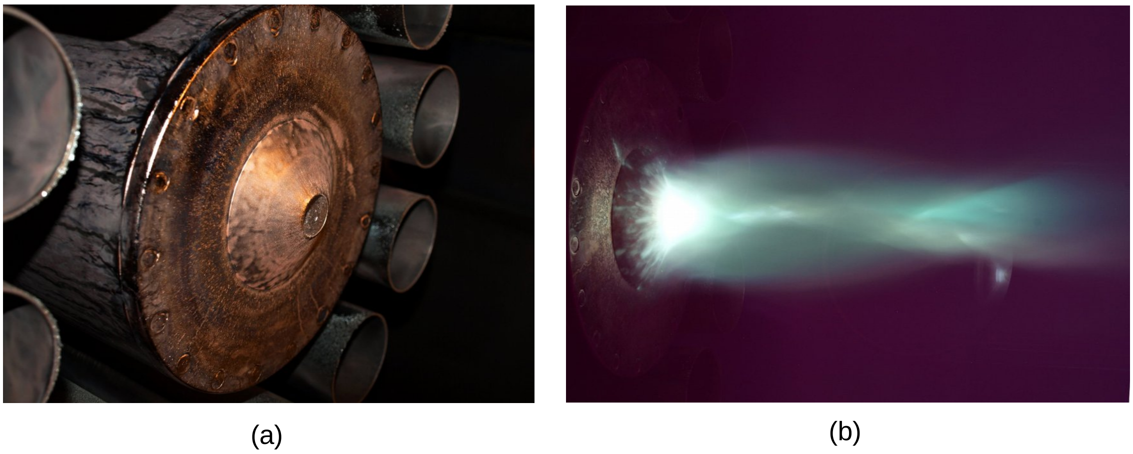
(a) (b)

Figure 6.2: Photo of the electrode system with the central electrode cone. (a) detailed view on the central electrode cone, (b) during shot №12055.

6.2 Experimental Results

Perhaps, the most significant result is the increase in the neutron yield. The typical neutron yield in the shots with anode cone is about 5.3×10^{10}, whereas in the shots with the flat-top anode the typical neutron yield is 0.8×10^{10} (6.6 times lower), for the charging voltage of 16 kV and initial deuterium gas pressure of 100 Pa.

Unlike at the classical plasma focus experiments, the typical firs dip in the current derivative was not accompanied by the SXR, HXR, and neutron pulse as is apparent from the normalized signals in fig. 6.3 from the representative shot №11856.

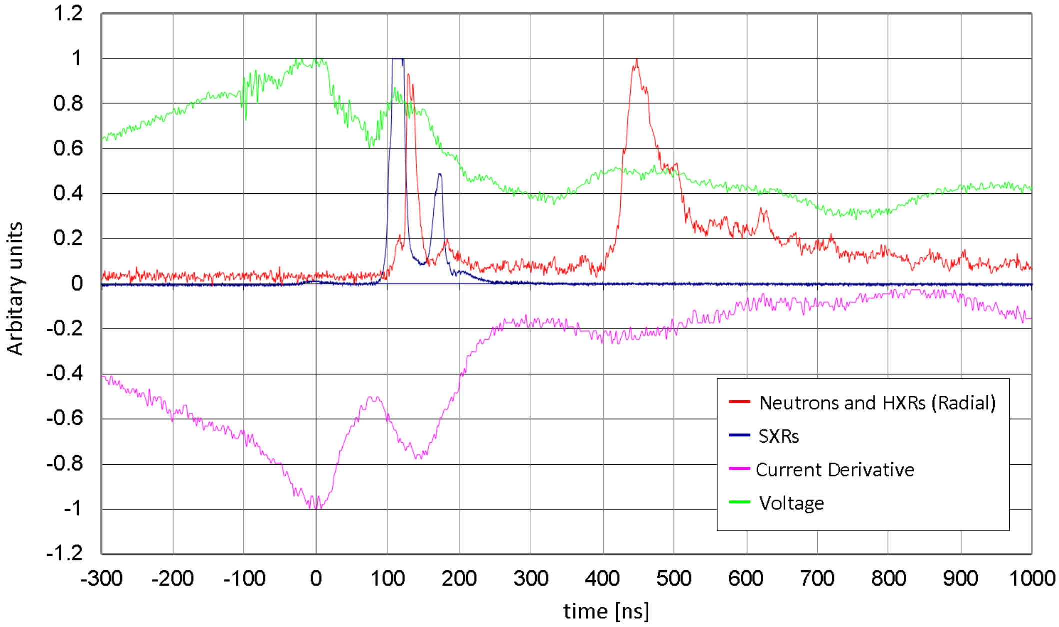

Figure 6.3: Normalized signals of the scintillation detector (neutrons and HXRs), PIN-diode (SXRs), current derivative, and voltage from shot №11856.

6.2.1 Interferometric study

Examining the sequence of the interferometric images of the representative shot №11856 in fig. 6.4, a significant change in the compressed plasma shape is apparent. At the maximum of compression, the minimum diameter is typically of about 1 cm. Thus, in comparison with the classical plasma focus experiment with the flat-top anode, the minimum plasma diameter is almost twice smaller in the case of the anode cone experiments. As far as the plasma column length is concerned, the pinched plasma was shortened to $1-2$ cm, from ~ 7 cm typical for the classical anode shape.

As far as the plasma implosion is concerned, in average, the implosion velocity reaches 10^5 m/s similarly as in the shots with the classical flat-top anode. Likewise the pinched plasma electron density achieves $(10^{24}-10^{25})$ m^{-3}.

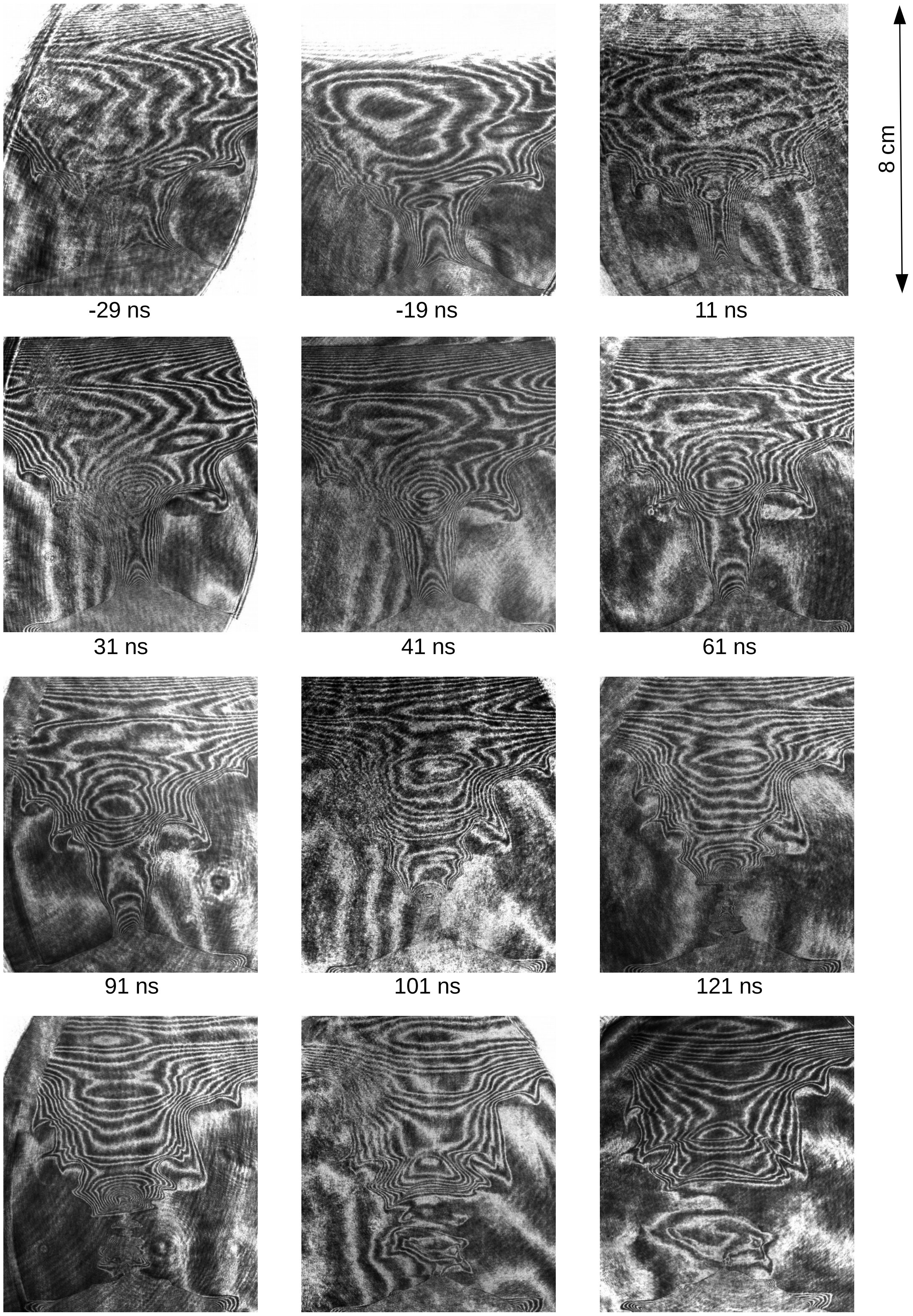

-29 ns -19 ns 11 ns

31 ns 41 ns 61 ns

91 ns 101 ns 121 ns

131 ns 161 ns 181 ns

Figure 6.4: Time sequence of interferometric images in shot №11856.

6.2.2 MCP Pinhole Camera Images

In the sequence of the MCP SXR camera images in fig. 6.5, we can see the bright anode cone on the bottom border of the frames which overexpose the images due to intensive x-rays. Above the cone is visible column of the deuterium pinched plasma. In contrast to the shots with the flat-top anode, the pinched plasma column SXR radiation in the MCP images is weak. It is in accordance with the PIN-diode SXR signals. Since the plasma densities in the shots with and without the anode cone are similar, it seems that the the weak SXR emission could be caused by a lower temperature at the stopping of the plasma implosion.

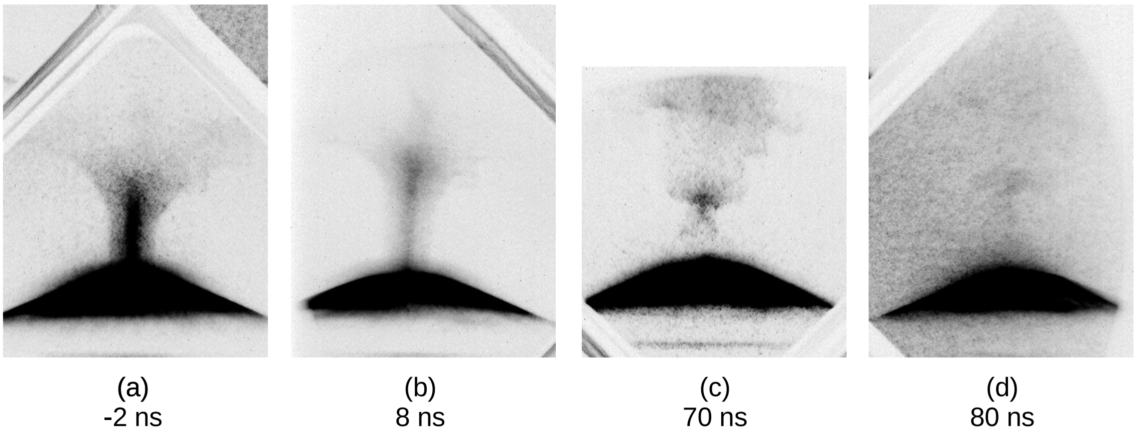

Figure 6.5: Shot №12085 MCP SXR pinhole camera images.

6.3 Conclusions

As the most important result of the experiments with the anode cone, we present the significant increase of the neutron yield in comparison with the classical flat-top anode. This result is different than the simulations and experiments with the hemispherical anode presented in [169] in which the neutron yield was lower than in the case of the flat-top anode. The reasons why the increase of the neutron yield occurs are still being investigated. Our experiments with the central anode cone are published in papers [170, 15].

Chapter 7

Discussion

In the beginning of the discussion of the experiments, we summarize the experimental data. In tab. 7.1 we found the fundamental experimental data from the shots with the classical plasma focus load, gas-puff load, and load with the central electrode cone, reported in this thesis. In this table, shots with the optimal initial settings are taken into account. As the optimal initial settings we mean such charging voltage and working gas pressure in which the maximum of compression occurs at the time close to the current maximum. The discharge parameters listed in tab. 7.1 are as follows: η_e linear electron density, ρ_m linear mas density, v_{mip} plasma implosion velocity, E_i ion kinetic energy given by the v_{mip}, L length of the pinched plasma column, I_{max} discharge current maximum, U_{peak} peak voltage, D_{min} minimal diameter of the pinched plasma, D_S diameter of the plasma column during the stagnation, $\langle n_e \rangle$ mean electron density, and Y_N total neutron yield.

For an application of plasma focus as a neutron source, it is important to find plasma focus load configuration with the most efficient neutron production. Looking into tab. 7.1 we see that in the shots with the central electrode cone, the average neutron yield is 6.6 times higher than in the shots with the same charging voltage but without the cone.

From the results in tab. 7.1 we can found general parameters which characterize the Z-pinch plasma in experiments reported in this thesis.

Load configuration	Classical plasma focus discharge			D_2 gas-puff		D_2 gas-puff	Anode cone
Initial filling gas	D_2	D_2	Ne	D_2	D_2	Ne	D_2
Initial filling gas pressure [Pa]	100	200	80	100	200	80	100
Gas-puff initial pressure [Pa]	-	-	-	(15×10^5) Pa	(15×10^5) Pa	(15×10^5) Pa	-
Charging voltage [kV]	16	23	23	16	23	23	16
Sotred Energy [kJ]	250	350	350	250	350	350	250
η_e [$\times 10^{18}$ cm^{-1}]	7 ± 1	7.1 ± 0.8	1.6 ± 0.3	$(7 + 4) \pm 1$	$(6.6 + 4.0) \pm 1.0$	$(1.4 + 2.0) \pm 0.3$	5.0 ± 0.5
ρ_m [µg/cm]	24 ± 2	24 ± 2	54 ± 10	$(24 + 3) \pm 6$	$(22 + 13) \pm 3$	$(46 + 7) \pm 10$	17 ± 2
v_{imp} [$\times 10^5$ m/s]	1.5 ± 0.2	1.7 ± 0.4	2.1 ± 0.2	1.5 ± 0.2	1.5 ± 0.2	1.7 ± 0.4	1.0 ± 0.2
E_i [keV]	0.25 ± 0.10	0.3 ± 0.1	4.6 ± 1.0	0.25 ± 0.10	0.25 ± 0.10	3.6 ± 0.7	0.17 ± 0.05
L [cm]	7 ± 1	7 ± 1	1.5 ± 0.5	7 ± 1	7 ± 1	2.0 ± 0.5	1.5 ± 0.5
I_{max} [MA]	1.2 ± 0.1	1.8 ± 0.2	1.7 ± 0.2	1.2 ± 0.1	1.8 ± 0.2	1.7 ± 0.2	1.2 ± 0.1
U_{peak} [kV]	20 ± 2	28 ± 5	32 ± 6	17 ± 2	25 ± 5	35 ± 6	17 ± 3
D_{min} [cm]	1.8 ± 0.2	1.4 ± 0.2	0.5 ± 0.1	0.3 ± 0.1	1.5 ± 0.2	0.7 ± 0.3	1.0 ± 0.3
D_S [cm]	2.0 ± 0.2	2.5 ± 0.2	0.6 ± 0.1	2.1 ± 0.3	4.0 ± 0.2	1.0 ± 0.2	2.1 ± 0.5
$\langle n_e \rangle$ at D_{min} [$\times 10^{24}$ m^{-3}]	4.4 ± 1.0	4.5 ± 1.0	2.5 ± 0.3	4.4 ± 1.0	5.0 ± 1.0	4.0 ± 0.5	4.5 ± 1.0
$\langle n_e \rangle$ in stagnation [$\times 10^{24}$ m^{-3}]	1.0 ± 0.3	1.1 ± 0.1	0.6 ± 0.1	0.6 ± 0.1	1.5 ± 0.1	1.0 ± 0.2	3.1 ± 0.5
Y_N [$\times 10^{10}$]	0.8 ± 0.3	4.5 ± 3.0	-	0.8 ± 0.5	5.9 ± 3.0	4.0 ± 3.0	5.3 ± 2.0

Table 7.1: Summary of the fundamental experimental data from the experiments with different plasma focus load.

Mean-Free Path

We begin with the mean-free path which is very fundamental plasma parameter necessary for many considerations.

The mean-free paths in Z-pinch plasma could be estimated using formulas in [171]. Approximation of the mean-free path in meters for electron-ion Coulomb collisions is

$$\lambda_e \approx 2 \times 10^{22} \frac{T_e^2}{Z n_e}, \tag{7.1}$$

where T_e electron temperature is in keV, Z is average charge state of ions, and n_e is electron density in m^3. The mean-free path for ion-ion collisions is approximated by [171]

$$\lambda_i \approx 2 \times 10^{22} \frac{T_i^2}{Z^3 n_e}, \tag{7.2}$$

where T_i is the ion temperature in keV and Z is the ion charge. In the case of the hot deuterium plasma in which $Z = 1$, the equations (7.1) and (7.2) become fully analogous, differing only in the temperature. The dependence of both electron and ion mean-free path for various temperatures is displayed in fig. 7.1. In fig. 7.1. We assume that the ion temperature is approximately equal to the ion kinetic energy given by the implosion velocity. Examining tab. 7.1 we found that the deuteron temperature is approximately $(0.2 - 0.3)$ keV. For plasma during the stagnation with the typical electron density of about 10^{-24} m^3 we obtain the ion mean-free path $(0.8 - 1.8)$ mm. It is a boundary between the colision and colsionless plamsa. As far as electrons are considered, their temperature is higher than the kinetic energy given by the implosion velocity due to electron-ion collisions. By SXR study published in [168], using time-resolved filtered PIN diodes and Rowland Spectrometer spectrometer, the electron temperatures ranges from 50 to 150 keV. Thus, the electron mean-free path is approximately $(0.05 - 0.5)$ mm.

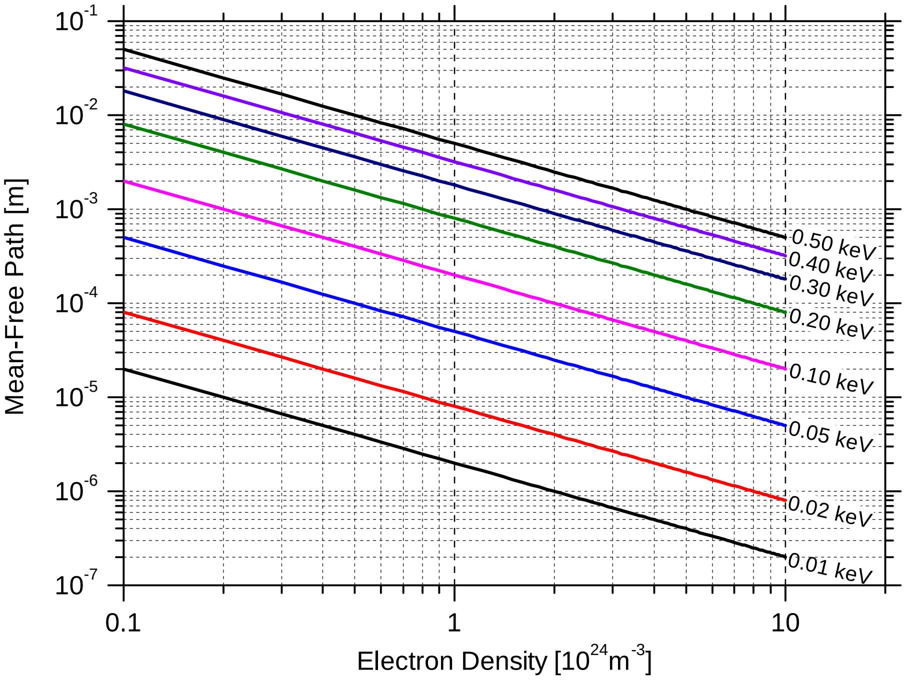

Figure 7.1: Dependence of the mean-free path for electrons.

Temperature Equilibrium Time

Using the estimation of the electron temperature and electron density, we could approximate the temperature equilibrium time in nanoseconds for Z-pinch plasma by formula [171]

$$\tau_{eq} \approx 10^{27} \frac{A T_e^{3/2}}{Z n_e}, \tag{7.3}$$

where A is the atomic mass. For deuterium plasma, assuming $A = 2$, $T_e = (0.05 - 0.15)$ keV, $Z = 1$, and $n_e = 10^{24}$ m^{-3} we obtain the thermal equilibrium time of approximately $(20 - 120)$ ns. Consequently, the dense structures could could be in quasi-stationary state longer time.

Collision Time

Collision time and collision rate are parameters closely related with the mean-free path. For electrons and ions the collision time is given by

$$\tau_{e,i} = \frac{1}{\nu_{e,i}} = \frac{\lambda_e}{v_{Te,Ti}}, \tag{7.4}$$

where $\nu_{e,i}$ is collision rate and $v_{Te,Ti}$ is the thermal velocity of electrons (index Te) and ions (index Ti) [171]. Assuming $v_{Ti} = v_{imp} \doteq 1.5 \times 10^5$ m/s and $v_{Te} = \sqrt{2T_e/m_e} \doteq (4-7) \times 10^6$ m/s, we obtain $\tau_i \doteq (5-12)$ ns ($\nu_i \doteq (8-20) \times 10^7$ s^{-1}) and $\tau_e \doteq (13-38)$ ps ($\nu_e \doteq (3-8) \times 10^{10}$ s^{-1}).

Collisionality

Knowing the mean-free path of the particles in plasma, we could evaluate electron and ion collisionality. The collisionality (C) is very important for plasma dynamics and thermalization processes in the plasma [171]. The dimensionless C parameter is defined as the ratio of l the spatial scale and the particle mean free path [171]. Thus, collisionality for electrons and ions is given by

$$C_{e,i} = \frac{l}{\lambda_{e,i}}, \tag{7.5}$$

where l is a plasma scale-length along the magnetic flux tube [171]. Assuming $l \doteq 6$ cm, we obtain ion collisionality between 33 and 75 and electron collisionality $120 - 1200$.

Magnetization

Similarly like the collisionality, the electron magnetization[1] is a dimensionless parameter very important for thermodynamics of the pinched plasma [171]. As far as the ion magnetization is concerned, in the case of deuterium or deuterium-tritium plasma, it could plays a significant role in the neutron production efficiency [101]. The magnetization for electrons and ions is defined as the ratio of the cyclotron frequency and the collision rate [171]

$$M_{e,i} = \frac{\omega_{Ci,e}}{\nu_{e,i}}, \tag{7.6}$$

where the cyclotron frequency is given by the well-known formula $\omega_{Ce,i} =\mid Q \mid_{e,i} B/m_{e,i}$. The toroidal magnetic field[2], evaluated by the pinched deuterium plasma current and diameter, is approximately 20 T. Thus, the cyclotron frequencies are $\omega_{Ce} \doteq 3.6 \times 10^{12}$ rad/s and $\omega_{Ci} \doteq 9.4 \times 10^{8}$ rad/s and magnetizations are $M_e \doteq (50 - 140)$ and $M_i \doteq (5 - 11)$.

Alfvén Velocity

The Alfvén velocity is the characteristic velocity of plasma macroscopic transformations, e.g. magnetohydrodynamic instabilities [31, 39, 154]. For the deuterium plasma, the Alfvén velocity could be evaluated in SI units by the following formula [154]

$$v_A \approx 2.2 \times 10^{16} \frac{B}{\sqrt{n_e}}. \tag{7.7}$$

For our experiments we obtain the Alfvén velocity during the pinched plasma stagnation of approximately 4×10^5 m/s in the regions with the electron density of 10^{24} m^{-3} and approximately 5×10^4 m/s in the regions with the higher density of 10^{25} m^{-3}.

---

[1] We note, that in physics exists also a different definition of magnetization $M = \frac{q}{lt}$ [1]. Such a sense of M magnetization is not considered in this thesis.

[2] The magnetic field of pinched plasma contains also a poloidal component. However, the poloidal component is negligible in comparison with the toroidal component.

Parameter β

The dimensionless parameter β is defined as the ratio of the thermodynamic pressure and the magnetic pressure. Large β parameter implies that the magnetic field does not plays a significant role in the macroscopic plasma dynamics [171]. In [171], we found the following evaluation of the β parameter

$$\beta = \frac{p}{p_m} = 4 \times 10^{-22} \frac{n_e \left(T_e + \dfrac{T_i}{Z} \right)}{B^2}, \tag{7.8}$$

where p is the thermodynamic pressure and p_m is the magnetic pressure. Substituting above mentioned typical parameters of plasma in our experiments in SI units into (7.8) we obtain $\beta \doteq 0.4$ in the regions with $n_e = 10^{24}$ m^{-3} and $\beta \doteq 4$ in the regions with $n_e = 10^{25}$ m^{-3}. Consequently, the dense plasma structures in Z-pinches and plasma focuses are magnetized.

Magnetic Reynolds Number

In the magnetohydrodynamics, a time-evolution of the magnetic field could be described by the following formula derived from the Maxwell's equations and Ohm's law [31]

$$\frac{\partial \mathbf{B}}{\partial t} = \nabla \times (\mathbf{v} \times \mathbf{B}) + \frac{1}{\sigma\mu}\nabla^2\mathbf{B}, \tag{7.9}$$

where $\mathbf{v}$ is the plasma mass flow velocity, σ is the plasma conductivity, and μ is the plasma permeability. The first term in the right side of (7.9) represents the magnetic field freezing rate and the second term represents the resistive dissipation of the magnetic field [31]. The ratio of the first term and second term in (7.9) is called the magnetic Reynolds number. For the Z-pinch plasma, the Reynolds number could be evaluated by the following formula [171]

$$R_M = 0.25MT^2 l\sqrt{\frac{Z+1}{Z^2 A}}, \tag{7.10}$$

where M is the above evaluated magnetization, T is the plasma temperature in keV, and ll is the spatial length scale in cm. If the plasma conductivity is high, $R_M \gg 1$ and the magnetic filed is frozen into plasma [31, 171]. Otherwise, if $R_M l1$ the ohmic dissipation is dominant.

For the hot deuterium plasma the atomic mass and ion charge are $A = 2$ and $Z = 1$. If we assume the lowest reasonable parameters: $M = 5$, $T = 20$ eV, and $l = 1$ cm, we obtain $R_M = 3125$. Thus, even in such very pessimistic estimation the R_M is very high and in fact is probably even higher. Therefore, in our experiment, the magnetic field is effectively frozen into the plasma.

Larmor radius

For completeness of the characterizing of the plasma in our experiments, the very basic plasma parameters are evaluated by the above presented values.

To evaluate the Larmor radius we assume toroidal magnetic field of 20 T. For the electron velocities of $(4-7)\times 10^6$ m/s we obtain the electron Larmor radius of $(10-20)$ μm and for ions with a velocity of about 1.5×10^5 m/s the Larmor radius is approximately 160 μm, which is lower than ion mean free path.

Debye length

As far as the Debye length is concerned, for the non-equilibrium the Debye length is given by [154]:

$$\lambda_D = \left[\frac{ne^2}{\varepsilon_0}\left(\frac{1}{kT_e} + \frac{1}{kT_i}\right)\right]^{-\frac{1}{2}} . \tag{7.11}$$

For above mentioned electron and ion temperatures $\lambda_D \doteq 50$ nm in the region with $n_e = 10^{24}$ m^{-3} and $\lambda_D \doteq 20$ nm in the region with $n_e = 10^{25}$ m^{-3}. Thus, since the number of charged particles is about roughly 523 for $n_e = 10^{24}$ m^{-3} and 335 for $n_e = 10^{25}$ m^{-3} and λ_D is much smaller then characteristic dimensions of the plasma in our experiments, the collective behavior could be assumed.

Nuclear Fusion Energy Yield

Obviously, the energy released by the nuclear fusion reactions is much smaller than the electrical energy stored in the capacitor banks, or the energy energy transferred to the imploding plasma. However, it could be interesting to quantify such released energy. A number of reached D(d,n)^{3}He reactions is given by the neutron yield. A probability of the second branch of DD collision, the reaction D(d,p)T with the energy yield of about 4.03 MeV, is practically equal to the probability of the D(d,n)^{3}He reaction with the energy yield of about 3.27 MeV [1]. Other reactions we do not take into account[3]. Assuming a good shot with a relatively high neutron yield of 10^{11} we obtain the total energy released from the nuclear fusion reactions of about 0.12 J. This is approximately 3×10^6 times less energy than the electrical energy of 350 kJ stored in the capacitors at the 23 kV charging.

---

[3] One can note, that reactions D(t,n)^{4}He could occur do to the MeV tritons produced by the D(d,p)T reaction. However the number of the tritions ($10^9 - 10^{11}$) is negligible in comparison with the number of deuterons in the plasma.

Summary of Plasma Characterizing Parameters

The above introduced plasma characterizing parameters, for the electron density $n_e = 10^{24}$ m^{-3} and $n_e = 10^{25}$ m^{-3} which are typical for plasma in our experiments, are summarized in tab. 7.2. We note, that in the hot deuterium plasma we assume $n_e = n_i$.

Electron density [m^{-3}]	10^{24}	10^{25}
Electron mean-free path [mm]	0.05 – 0.5	0.005 – 0.05
Deuteron mean-free path [mm]	0.8 – 1.8	0.08 – 0.18
Temperature Equilibrium Time [ns]	20 – 120	2 – 12
Electron collision time [ps]	13 – 38	1.3 – 3.8
Deuteron collision time [ns]	5 – 12	0.5 – 1.2
Electron collision rate [s^{-1}]	$(8 - 20) \times 10^{7}$ s^{-1}	$(8 - 20) \times 10^{8}$ s^{-1}
Deuteron collision rate [s^{-1}]	$(3 - 8) \times 10^{10}$ s^{-1}	$(8 - 20) \times 10^{11}$ s^{-1}
Electron collisionality [-]	120 – 1200	1200 – 12000
Deuteron collisionality [-]	33 – 75	330 – 750
Electron magnetization [-]	50 – 140	5 – 14
Deuteron magnetization [-]	5 – 11	0.5 – 1.1
Alfvén Velocity [m/s]	4×10^{5}	5×10^{4}
Parameter β [-]	0.4	4
Magnetic Reynolds number [-]	> 3125	> 6875
Electron Larmor radius [µm]	10 – 20	
Deuteron Larmor radius [µm]	160	
Debye length [nm]	50	20
Number of particles in Debye sphere [-]	523	325

Table 7.2: Fundamental parameters characterizing plasma in experiments presented in this thesis

Chapter 8

Conclusions

In this thesis, the experiments with two novel configurations of the plasma focus experimental load are presented: experiments with the central electrode (anode) gas-puff and experiments with central electrode (anode) cone. For a reference, classical plasma focus experiments with the static deuterium gas filling are presented int his thesis too. In these experiments, the plasma is investigated using the 16-frame optical interferometer, 4-frame gated MCP soft x-ray pinhole camera, and soft x-ray PIN-diodes. The DD neutron yield is measured using the silver activation counters and using the scintillation detectors, the time-resolved signals of the neutron pulses are obtained.

Based on the experimental data the plasma dimensions, implosion velocities, plasma densities, and temperatures were evaluated. By these evaluated quantities the fundamental parameters which characterize the plasma were estimated.

A summary of the most interesting results of the experiments are as follows.

8.1 Selected Results of Experiments

In the experiments with deuterium gas filling and deuterium gas-puff, the plasma stays a longer time stable than in the classical experiment with the static deuterium filling. In these shots, the typical neutron yield is not significantly different from the neutron yield in the shots with the static deuterium gas filling.

In the shots with the deuterium gas-puff very bright plasma fiber filaments have been observed by the MCP soft x-ray camera. The origin of this filaments is not known. We could assume that is particularly cased by impurities. However, the impurities could play just a role of a “dye” which allows a visualization of hot spots in the plasma. Such filaments have never been observed in the shots without the central electrode deuterium gas-puff and we have not found any earlier observation of any similar plasma structures in the plasma focus experiments.

An increased attention have been devoted to the study of the relatively long-lived ball-like plasma structures. Their electron densities and time evolution was investigated using the interferometry.

In the shots with deuterium gas initial filling and neon gas-puff, a bright radiation in the center of the pinched plasma is observed by the MCP soft x-ray camera. It indicates a presence of neon in the central region of the pinched plasma. At the same time, a relatively high average neutron yield of 4×10^{10}, comparable with the neutron yield in the shots with the pure deuterium, was reached. Therefore, it seems that the mixing of deuterium and neon does not significantly affect the neutron yield, or that the neutrons are produced by deuteron reactions not in the center of the pinched plasma but on a larger diameter.

In the plasma focus experiments with the central electrode cone a significant increase in the neutron yield was achieved. In the shots with the static deuterium gas filling with the same pressure and the same charging voltage, the average neutron yield was $6-7$ times higher in the shots with the cone than in the shots with classical anode shape.

The experiments with the central electrode cone are still at the beginning. For a better understanding to reasons of the neutron yield increase more systematic experimental campaigns are required.

A personal contribution of the author of this thesis to the experiments reported in this thesis is summarized in appendix A and the list of the experimental internships is presented in appendix D.

In appendix B and appendix C are lists of papers and conference contributions in which the experiments presented in this thesis are published.

8.2 Perspective of Pinched Plasma Research

The plasma foci which are in principle Z-pinch devices, are very efficient neutron and hard x-ray sources. Currently the MA-class plasma foci are used as neutron sources for the subcritical experiments in USA [55, 56, 57, 58]. Nowadays, plasma foci plays also significant role in the laboratory astrophysics [64, 66, 71, 72, 73, 74]. As far as the thermonuclear fusion at pinched plasma is concerned, in the MagLIF experiments, the thermonuclear DD neutron yield of 2×10^{12} was achieved.

In the world, several new MA-class plasma focus and Z-pinch devices have been recently assembled, for example PF-24 [138] CQ-3-MMAF [134], and MAIZE [137]. Z-pinch devices with even higher currents of 48 MA and 65 MA are designing in USA [172].

Therefore, the plasma focus research seems to be perspective and promising.

8.3 Future Prospects

There are many future plans. For example to perform experiments with several shapes of the central electrode cone, try to find the optimal one for highest neutron yield and explain the reason of the neutron yield increase.

The great and long-term challenge is to explain the observed organized ball-like, toroidal, and fiber plasma structures, try to find an astrophysical analogy of these plasma structures, and using a suitable scaling characterize it.

Appendix A

Author's Personal Contribution to Experiments

Author of this thesis actively participates in the plasma focus experimental campaigns on the PF-1000 device in the years 2013–2016. The list of these experimental internships we found in appendix D.

The main contribution of the author of this thesis is the processing of the experimental data, especially processing of the images obtained by the unique 16-frame interferometer. With a help of the interferometry, the plasma dynamics, line densities, and volume densities have been evaluated. The author's most crucial contribution to the plasma focus research lies in the experiments with the central electrode gas-puff. These experiments are new in the plasma focus research and their results are original. In the gas-puff experiments, unique long-lived filaments of a ball or fiber form have been observed. Therefore, a special emphasis, in the author's work, is put on the study of these structures.

Author of this thesis is the corresponding author of two papers in impacted journals [161, 162]. She is also a co-author of 25 other papers in impacted journals. Total list of the author's papers is reported in the appendix B. List of the conference contributions is reported in appendix C.

Appendix B

List of Papers

List of papers related to this doctoral thesis in journals with the impact factor. We note that, in some publications, maiden name B. Batobolotova is used. In the following publications an equal contribution of all authors is assumed.

1. B. Cikhardtova, P. Kubes, J. Cikhardt, M. Paduch, J. Kravarik, K. Rezac, J. Kortanek, *Evolution of the small ball-like structures in the plasma focus discharge*, Nukleonika **61**, 2, 2016. (The authors contributed equally to this publication, each of them by 14%).

2. B. Cikhardtova, P. Kubes, J. Cikhardt, M. Paduch, E. Zielinska, J. Kravarik, K. Rezac, J. Kortanek, O. Sila, *Temporal distribution of linear densities of the plasma column in a plasma focus discharge*, Nukleonika **60**, 2, 2015. (The authors contributed equally to this publication, each of them by 11%).

3. P. Kubes, M. Paduch, M.J. Sadowski, J. Cikhardt, B. Cikhardtova, D. Klir, J. Kravarik, V. Munzar, K. Rezac, E. Zielinska, E. Skladnik-Sadowska, A. Szymaszek, K. Tomaszewski, and D. Zaloga, *Axial compression of plasma structures in a plasma focus discharge*, Physics of Plasmas **25**, 6, ISSN: 1070-664X 2018.

4. P. Kubes, M. Paduch, M.J. Sadowski, J. Cikhardt, B. Cikhardtova, D. Klir, J. Kravarik, V. Munzar, K. Rezac, E. Zielinska, E. Skladnik-Sadowska, A. Szymaszek, K. Tomaszewski, and D. Zaloga, *Characterization of fast deuterons involved in the production of fusion neutrons in a dense plasma focus*, Physics of Plasmas **25**, 1, ISSN: 1070-664X 2018.

5. P. Kubes, M. Paduch, J. Cikhardt, B. Cikhardtova, D. Klir, J. Kravarik, K. Rezac, E. Zielinska, M.J. Sadowski, A. Szymaszek, K. Tomaszewski, and D. Zaloga, *Increase in the neutron yield from a dense plasma-focus experiment performed with a conical tip placed in the centre of the anode end*, Physics of Plasmas **24**, 9, ISSN: 1070-664X 2017.

6. P. Kubes, M. Paduch, J. Cikhardt, B. Cikhardtova, D. Klir, J. Kravarik, K. Rezac, E. Zielinska, M.J. Sadowski, A. Szymaszek, K. Tomaszewski, and D. Zaloga, *Transformation of the ordered internal structures during the acceleration of fast charged particles in a dense plasma focus*, Physics of Plasmas **24**, 7, ISSN: 1070-664X 2017.

7. P. Kubes, M. Paduch, J. Cikhardt, B. Cikhardtova, D. Klir, J. Kravarik, K. Rezac, E. Zielinska, M. J. Sadowski, A. Szymaszek, K. Tomaszewski, D. Zaloga, *Filamentation in the pinched column of the dense plasma focus*, Physics of Plasmas **24**, 3, ISSN: 1070-664X, 2017.

8. P. Kubes, M. Paduch, B. Cikhardtova, J. Cikhardt, D. Klir, J. Kravarik, K. Rezac, J. Kortanek, E. Zielinska, M. J. Sadowski, K. Tomaszewski, *Interferometry and x-ray diagnostics of pinched helium plasma in a dense plasma focus with an Al-wire on the axis*, Physics of Plasmas **23**, 11, 2016

9. P. Kubes, M. Paduch, B. Cikhardtova, J. Cikhardt, D. Klir, J. Kravarik, K. Rezac, J. Kortanek, E. Zielinska, M.J. Sadowski, K. Tomaszewski, *The influence of the nitrogen admixture on the evolution of a deuterium pinch column*, Physics of Plasmas **23**, 2016.

10. P. Kubes, M. Paduch, B. Cikhardtova, J. Cikhardt, D. Klir, J. Kravarik, K. Rezac, E. Zielinska, D. Zaloga, M. J. Sadowski, K. Tomaszewski, *Influence of the Al wire placed in the anode axis on the transformation of the deuterium plasma column in the plasma focus discharge*, Physics of Plasmas **23**, 2016.

11. P. Kubes, M. Paduch, J. Cikhardt, D. Klir, J. Kravarik, K. Rezac, B. Cikhardtova, J. Kortanek and E. Zielinska, *The evolution of the plasmoidal structure in the pinched column in plasma focus discharge*, Plasma Physics and Controlled Fusion **58**, 4, ISSN: 0741-3335, 2016.

12. P. Kubes, M. Paduch, J. Cikhardt, D. Klir, J. Kravarik, K. Rezac, B. Cikhardtova, J. Kortanek, E. Zielinska, *The evolution of the plasmoidal structure in the pinched column in plasma focus discharge*, Plasma Physics and Controlled Fusion **56**, 2016.

13. P. Kubes, M. Paduch, J. Cikhardt, D. Klir, K. Rezac, J. Kravarik, B. Cikhardtova, J. Kortanek, E. Zielinska, *Puffing Deuterium Compressed by a Neon Plasma Sheath at the Initial Poloidal Magnetic Field in Plasma Focus Discharge*, IEEE Transactions on Plasma Science **53**, 8, 2015.

14. P. Kubes, M. Paduch, J. Cikhardt, B. Cikhardtova, K. Rezac, D. Klir, J. Kravarik, J. Kortanek, and E. Zielinska, *Investigation of compression of puffing neon by deuterium current and plasma sheath in plasma focus discharge*, Physics of Plasmas **22**, 6, ISSN: 1070-664X, 2015.

15. P. Kubes, M. Paduch, J. Cikhardt, D. Klir, J. Kravarik, K. Rezac, J. Kortanek, B. Cikhardtova, and E. Zielinska, *Existence of a return direction for plasma escaping from a pinched column in a plasma focus discharge*, Physics of Plasmas **22**, 5, ISSN: 1070-664X, 2015.

16. P. Kubes, M. Paduch, J. Cikhardt, J. Kortanek, B. Cikhardtova, K. Rezac, D. Klir, J. Kravarik, and E. Zielinska: *Filamentary structure of plasma produced by compression of puffing deuterium by deuterium or neon plasma sheath on plasma-focus discharge*, Physics of Plasmas **21**, 12, ISSN: 1070-664X, 2014.

17. P. Kubes, M. Paduch, J. Cikhardt, J. Kortanek, B. Batobolotova, K. Rezac, D. Klir, J. Kravarik, W. Surala, E. Zielinska, M. Scholz, L. Karpinski, and M.J. Sadowski, *Neutron production from puffing deuterium in plasma focus device*, Physics of Plasmas **21**, 8, ISSN: 1070-664X, 2014.

List of papers in journals with the impact factor which are not directly related to this doctoral thesis.

1. D. Klir, A.V. Shishlov, V.A. Kokshenev, P. Kubes, K. Rezac, S. Buryskova, R.K. Cherdizov, J. Cikhardt, B. Cikhardtova, G.N. Dudkin, J.T. Engelbrecht, F.I. Fursov, S.L. Jackson, J. Krasa, J. Kravarik, N.E. Kurmaev, V. Munzar, V.N. Padalko, N.A. Ratakhin, O. Sila, K. Turek, V.A. Varlachev and R. Wagner, Plasma Physics and Controlled Fusion **61**, 1, ISSN: 0741-3335, 2019.
2. V. Munzar, D. Klir, J. Cikhardt, B. Cikhardtova, J. Kravarik, P. Kubes, K. Rezac, *Investigation of Magnetic Fields in Z-Pinches via Multi-MeV Proton Deflectometry*, IEEE Transactions on Plasma Science **46**, 11, ISSN: 0093-3813, 2018.
3. D. Klir, A.V. Shishlov, V.A. Kokshenev, P. Kubes, K. Rezac, R.K. Cherdizov, J. Cikhardt, B. Cikhardtova, G.N. Dudkin, F.I. Fursov, T. Hyhlik, J. Kaufman, B.M. Kovalchuk, J. Krasa, J. Kravarik, N.E. Kurmaev, A.Yu. Labetsky, V. Munzar, H. Orcikova, V.N. Padalko, N.A. Ratakhin, O. Sila, J. Stodulka, K. Turek, V.A. Varlachev, and R Wagner, *Ion acceleration mechanism in mega-ampere gas-puff z-pinches*, New Journal of Physics **20**, ISSN: 1367-2630, 2018.
4. T. Pisarczyk, S.Yu. Guskov, T. Chodukowski, R. Dudzak, Ph. Korneev, N.N. Demchenko, Z. Kalinowska, J. Dostal, A. Zaras-Szydlowska, S. Borodziuk, L. Juha, J. Cikhardt, J. Krasa, D. Klir, B. Cikhardtova, P. Kubes, E. Krousky, M. Krus, J. Ullschmied, K. Jungwirth, J. Hrebicek, T. Medrik, J. Golasowski, M. Pfeifer, O. Renner, S. Singh, S. Kar, H. Ahmed, J. Skala, and P. Pisarczyk, *Kinetic magnetization by fast electrons in laser-produced plasmas at sub-relativistic intensities*, Physics of Plasmas **24**, 10, ISSN: 1070-664X 2017.
5. J. Cikhardt, D. Klir, K. Rezac, A. V. Shishlov, R. K. Cherdizov, B. Cikhardtova, G. N. Dudkin, F. I. Fursov, V. A. Kokshenev, J. Kravarik, P. Kubes, N. E. Kurmaev, A. Yu. Labetsky, V. N. Padalko, N. A. Ratakhin, O. Sila, K. Turek, V. A. Varlachev, *Neutron Spectrum Measured by Activation Diagnostics in Deuterium Gas-Puff Experiments on the 3 MA GIT-12 Z pinch*, IEEE Transactions on Plasma Science **45**, 12, ISSN: 0093-3813, 2017.

6. D. Klir, A. V. Shishlov, V. A. Kokshenev, P. Kubes, K. Rezac, J. Cikhardt, B. Cikhardtova, J. Kravarik, O. Sila, *Deuterium z-pinch as a powerful source of multi-MeV ions and neutrons for advanced applications* **23**, 3, 2016.

7. D. Klir, A. V. Shishlov, V. A. Kokshenev, P. Kubes, A. Yu. Labetsky, K. Rezac, R. K. Cherdizov, J. Cikhardt, B. Cikhardtova, G. N. Dudkin, F. I. Fursov, A. A. Garapatsky, V. M. Kovalchuk, J. Kravarik, N. E. Kurmaev, H, Orcikova, V. N. Padalko, N. A. Ratakhin,O. Sila, K. Turek, V. A. Varlachev: *Efficient generation of fast neutrons by magnetized deuterons in an optimized deuterium gas-puff z-pinch,*Plasma Physics and Controlled Fusion **57**, 4, ISSN: 0741-3335, 2015.

8. O. Sila, D. Klir, K. Rezac, J. Cikhardt, B. Cikhardtova, *MCNP calculations of neutron emission anisotropy caused by the GIT-12 hardware*, Nukleonika **60**, 2, 323–326 2015.

9. J. Cikhardt, J. Krása, M. De Marco, M. Pfeifer, A. Velyhan, E. Krouský, B. Cikhardtová, D. Klír, K. Řezáč, J. Ullschmied, J. Skála, P. Kubeš, J. Kravárik, *Measurement of the target current by inductive probe during laser interaction on terawatt laser system PALS*, Review of Scientific Instruments **85**, 103507, 2014.

10. J. Cikhardt, B. Batobolotova, P. Kubes, J. Kravarik, D. Klir, K. Rezac, *Influence of an external magnetic field on the dynamics of a modified plasma focus*, Physica Scripta **T161**, 014042, 2014.

Appendix C

List of Conference Contributions

List of poster presentations on international conferences. We note that, in some publications, maiden name B. Batobolotova is used.

1. B. Cikhardtova, P. Kubes, J. Cikhardt, M. Paduch, A. Pavlat, E. Zielinska, J. Kravarik, K. Rezac, J. Kortanek, *Closed currents as the possible explanation of the ball-like structures in the plasma focus discharge*, 27th Symposium on Plasma Physics and Technology, 20-23 June 2016 in Prague, Czech Republic.
2. B. Cikhardtova, P. Kubes, J. Cikhardt, M. Paduch, E. Zielinska, J. Kravarik, K. Rezac, J. Kortanek, *Evolution of the small ball-like strucures in the plasma focus discharge*, Plasma-2015: International Conference on Research and Applications of Plasmas, 7-11 September 2015, Warsaw, Poland.
3. B. Batobolotova, P. Kubes, M. Paduch, J. Kravarik, K. Rezac, J. Cikhardt, J. Kortanek, *Evolution of the small ball-like structures in the plasma focus discharge*, 26th Symposium on Plasma Physics and Technology, 16-19 June 2014 in Prague, Czech Republic.

Oral presentation on the international summer school:

B. Batobolotova, P. Kubes, J. Cikhardt, M. Paduch, J. Kravarik, K. Rezac, J. Kortanek, *Side-on and temporal distribution of linear densities in plasma focus discharge*, 12th Kudowa Summer School “Towards Fusion Energy”, 9-13th June 2014 in Kudowa Zdrój, Poland.

Appendix D

List of Internships

The list of active experimental internships is as follows.

1. Institute of Plasma Physics and Laser Microfusion, Hery Street 23, 01-497 Warsaw, Poland, 8-19 February 2016 (2 weeks).

2. Institute of Plasma Physics and Laser Microfusion, Hery Street 23, 01-497 Warsaw, Poland, 13-26 October 2015 (2 weeks).

3. Institute of High Current Electronics, Siberian Branch, Russian Academy of Sciences, 2/3 Akademichesky Avenue Tomsk 634055, Russia, May 2015 (3 weeks).

4. Institute of Plasma Physics and Laser Microfusion, Hery Street 23, 01-497 Warsaw, Poland, 1-14 February 2015 (2 weeks).

5. Institute of High Current Electronics, Siberian Branch, Russian Academy of Sciences, 2/3 Akademichesky Avenue Tomsk 634055, Russia, April 2014 (3 weeks).

6. Institute of Plasma Physics and Laser Microfusion, Hery Street 23, 01-497 Warsaw, Poland, 2-15 February 2014 (2 weeks).

7. Institute of Plasma Physics and Laser Microfusion, Hery Street 23, 01-497 Warsaw, Poland, 8-21 September 2013 (2 weeks).

8. Institute of High Current Electronics, Siberian Branch, Russian Academy of Sciences, 2/3 Akademichesky Avenue Tomsk 634055, Russia, June 2013 (3 weeks).
9. Institute of Plasma Physics and Laser Microfusion, Hery Street 23, 01-497 Warsaw, Poland, 14-27 April 2013 (2 weeks).

Bibliography

[1] J.D. Huba. *NRL Plasma Formulary*. Naval Research Laboratory, 2018.

[2] M. Scholz. *PLASMA-FOCUS AND CONTROLLED NUCLEAR FUSION*. Institute of Nuclear Physics PAN, Krakow, 2014.

[3] M. G. Haines. Fifty years of controlled fusion research. *Plasma Physics and Contorlled Fusion*, 34:643–656, 1996.

[4] United Nations. *Proceedings of the Second United Nations International Conference on the Peaceful Uses of Atomic Energy*, volume 31, Geneva, Switzerland, 1 September - 13 September 1958 1958.

[5] N.V. Filippov, T.I. Filippova, and V.P. Vinogradov. Dense high-temperature plasma in a non-cylindrical z-pinch compression. *Nucl. Fusion, Suppl.*, Jan 1962.

[6] J. W. Mather. Formation of a high-density deuterium plasma focus. *The Physics of Fluids*, 8(2):366–377, 1965.

[7] Filippov, Nikolai Vasilievich, 2018.
`https://ru.wikipedia.org/`.

[8] O. Zucker, W. Bostick, R. Gullickson, J. Long, J. Luce, and H. Sahlin. Design of a repetitively pulsed megajoule dense-plasma focus. *Lawrence Livermore Laboratory Report*, (UCRL-51872), 1975.

[9] O. Zucker, W. Bostick, J. Long, J. Luce, and H. Sahlin. The plasma focus as a large fluence neutron source. *Nuclear Instruments and Methods*, 145(1):185 – 190, 1977.

[10] M. Krishnan. The dense plasma focus: A versatile dense pinch for diverse applications. *IEEE Transactions on Plasma Science*, 40(12):3189–3221, Dec 2012.

[11] H. Herold, A. Jerzykiewicz, M. Sadowski, and H. Schmidt. Comparative analysis of large plasma focus experiments performed at ipf, stuttgart, and ipj, swierk. *Nuclear Fusion*, 29(8):1255, 1989.

[12] S. Lee. Neutron yield saturation in plasma focus: A fundamental cause. *Applied Physics Letters*, 95(151503), 2009.

[13] A. Bernard, H. Bruzzone, P. Choi, H. Chacqui, Vladimir Gribkov, J. Herrera, K. Hirano, A. Krejci, S. Lee, Ch. Luo, F. Mezzetti, M.J. Sadowski, H. Schmidt, K. Ware, Ch. S. Wong, and V. Zoita. Scientific status of plasma focus research. *Moscow University Physics Bulletin*, 8:93–170, JAN 1998.

[14] P. Kubes, J. Kravarik, D. Klir, K. Rezac, M. Bohata, M. Scholz, M. Paduch, K. Tomaszewski, I. Ivanova-Stanik, L. Karpinski, and M. J. Sadowski. Determination of deuteron energy distribution from neutron diagnostics in a plasma-focus device. *IEEE Transactions on Plasma Science*, 37(1):83–87, Jan 2009.

[15] P. Kubes, M. Paduch, M. J. Sadowski, J. Cikhardt, B. Cikhardtova, D. Klir, J. Kravarik, V. Munzar, K. Rezac, E. Zielinska, E. Skladnik-Sadowska, A. Szymaszek, K. Tomaszewski, and D. Zaloga. Characterization of fast deuterons involved in the production of fusion neutrons in a dense plasma focus. *PHYSICS OF PLASMAS*, 25(1), JAN 2018.

[16] Eric J. Lerner, Syed M. Hassan, Ivana Karamitsos, and Fred Von Roessel. Confined ion energy ¿ 200 keV and increased fusion yield in a DPF with monolithic tungsten electrodes and pre-ionization. *PHYSICS OF PLASMAS*, 24(10), OCT 2017.

[17] K. N. Mitrofanov, S. S. Anan'ev, D. A. Voitenko, V. I. Krauz, G. I. Astapenko, A. I. Markoliya, and V. V. Myalton. Localization of the magnetic field in a plasma flow in laboratory simulations of astrophysical jets at the KPF-4-PHOENIX installation. *ASTRONOMY REPORTS*, 61(9):775–782, SEP 2017.

[18] S. A. Danko, S. S. Ananyev, Yu G. Kalinin, V. I. Krauz, and V. V. Myalton. Spectroscopic studies of the parameters of plasma jets during their propagation in the background plasma on the PF-3 facility. *Plasma Phys. Control. Fusion*, 59(4), APR 2017.

[19] J. Paju B. Vali, T. Laas, V. Shirokova, K. Laas, M. Paduch V. A. Gribkov, E.V. Demina, M.D. Prusakova, V.N. Pimenov, V.A. Makhlaj, and M. Antonov. Generation and development of damage in double forged tungsten in different combined regimes of irradiation with extreme heat loads. *JOURNAL OF NUCLEAR MATERIALS*, 495:91–102, NOV 2017.

[20] M. Vilemova, Z. Pala, A. Jaeger, J. Matejicek, M. Chernyshova, E. Kowalska-Strzeciwilk, D. Tonarova, and V. A. Gribkov. Evaluation of surface, microstructure and phase modifications on various tungsten grades induced by pulsed plasma loading. *PHYSICA SCRIPTA*, 91(3), MAR 2016.

[21] O. Gemishev, S. Zapryanov, A. Blagoev, M. Markova, and V. Savov. Effect of multiple short highly energetic X-ray pulses on the synthesis of endoglucanase by a mutant strain of Trichoderma reesei-M7. *BIOTECHNOLOGY & BIOTECHNOLOGICAL EQUIPMENT*, 28(5):850–854, SEP 3 2014.

[22] J. Cikhardt. *High Energy Density Plasma Diagnostics Using Neutron and Gamma Detectors.* PhD thesis, Faculty of Electrical Engineering, Czech Technical University in Prague, 2017.

[23] R. Petr, D. Reilly, J. Freshman, N. Orozco, D. Pham, L. Ngo, and J. Mangano. Solid-state pulser development for high power dense plasma focus x-ray sources. *Japanese Journal of Applied Physics*, 39(2R):607, 2000.

[24] G. Decker, W. Kies, M.Malzig, C. van Calker, and G.Ziethen. High performance 300 kv driver speed 2 for ma pinch discharges. *Nuclear Instruments and Methods in Physics Research Section A: Accelerators, Spectrometers, Detectors and Associated Equipment*, 249(2):473 – 483, 1986.

[25] G. Decker, W. Kies, R. Nadolny, P. Röwekamp, F. Schmitz, G. Ziethen, K. N. Koshelev, Yu. V. Sidelnikov, and Yu. V. Sopkin. Micropinch actuation in the speed 2 plasma focus. *Plasma Sources Science and Technology*, 5(1):112, 1996.

[26] L. Soto. New trends and future perspectives on plasma focus research. *Plasma Phys. Control. Fusion*, 47:A361–A381, 2005.

[27] A. S. Richardson, S. Jackson, J. R. Angus, J. L. Giuliani, J. W. Schumer S. B. Swanekamp, and D. D. Mosher. Overview of the nrl dpf program: Experiment and modeling. In *APS Division of Plasma Physics Meeting 2016*, 2016.

[28] A. Beresnyak, J. Giuliani, S. Jackson, S. Richardson, S. Swanekamp, J. Schumer, R. Commisso, D. Mosher, B. Weber, and A. Velikovich. Simulations of a dense plasma focus on a high impedance generator. In *APS Division of Plasma Physics Meeting 2017*, 2017.

[29] N.V. Filippov, T.I. Filippova, I.V. Khutoretskaia, V.V. Mialton, and V.P. Vinogradov. Megajoule scale plasma focus as efficient x-ray source. *Physics Letters A*, 211(3):168 – 171, 1996.

[30] G. Basque, A. Jolas, and J. P. Watteau. Comparison of a two-dimensional snowplough model with experiment. *Physics of Fluids*, 11(6):1384–1386, 1968.

[31] P. Kulhanek. *Úvod do teorie plazmatu*. Aldebaran Group for Astrophysics, 2011.

[32] M. Akel, S. Ismael, S. Lee, S. H. Saw, and H. J. Kunze. Pf1000 high-energy plasma focus device operated with neon as a copious soft x-ray source. *IEEE Transactions on Plasma Science*, 45(11):2979–2983, Nov 2017.

[33] D. Attwood. *Soft X-Rays and Extreme Ultraviolet Radiation: Principles and Applications*. Cambridge University Press, 1999.

[34] R. Verma, M. V. Roshan, F. Malik, P. Lee, S. Lee, S. V. Springham, T. L. Tan, M. Krishnan, and R. S. Rawat. Compact sub-kilojoule range fast miniature plasma focus as portable neutron source. *PLASMA SOURCES SCIENCE & TECHNOLOGY*, 17(4), NOV 2008.

[35] M. Vilemova, Z. Pala, A. Jager, J. Matejicek, M. Chernyshova, E. Kowalska-Strzeciwilk, V. A. Gribkov, and M. Janata. Behavior and microstructural changes in different tungsten-based materials under pulsed plasma loading. *NUCLEAR MATERIALS AND ENERGY*, 9:123–127, DEC 2016.

[36] M. Chernyshova, V. A. Gribkov, E. Kowalska-Strzeciwilk, M. Kubkowska, R. Miklaszewski, M. Paduch, T. Pisarczyk, E. Zielinska, E. V. Demina, V. N. Pimenov, S. A. Maslyaev, G. G. Bondarenko, M. Vilemova, and J. Matejicek. Interaction of powerful hot plasma and fast ion streams with materials in dense plasma focus devices. *FUSION ENGINEERING AND DESIGN*, 113:109–118, DEC 2016.

[37] V. A. Gribkov, L. Karpinski, P. Strzyzewski, M. Scholz, and A. Dubrovsky. New efficient low-energy dense plasma focus in ipplm. *Czechoslovak Journal of Physics*, 54(3):C191, Mar 2004.

[38] M. A. Liberman, J.S. De Groot, A. Toor, and R.B. Spielman. *Physics of High-Density Z-Pinch Plasmas.* Springer New York, 1998.

[39] M. G. Haines. A review of the dense z-pinch. *Plasma Physics and Controlled Fusion*, 53, Mar 2011.

[40] D. D. Ryutov, M. S. Derzon, and M. K. Matzen. The physics of fast z pinches. *Rev. Mod. Phys.*, 72:167–223, Jan 2000.

[41] Berit Vali, Tonu Laas, Jana Paju, Veroonika Shirokova, Marian Paduch, Vladimir A. Gribkov, Elena V. Demina, Valeri N. Pimenov, Vadym A. Makhlaj, and Maksim Antonov. The experimental and theoretical investigations of damage development and distribution in double-forged tungsten under plasma irradiation-initiated extreme heat loads. *NUKLEONIKA*, 61(2):169–177, JUN 2016. International Conference on Research and Applications of Plasmas (PLASMA), Warsaw, POLAND, SEP 07-11, 2015.

[42] L. Rapezzi, M. Angelone, M. Pillon, M. Rapisarda, E. Rossi, M. Samuelli, and F. Mezzetti. Development of a mobile and repetitive plasma focus. *Plasma Sources Science and Technology*, 13(2):272, 2004.

[43] M. Krishnan, B. Bures, R. Madden, F. Blobner, and K. Wilson Elliott. A fast pulse, high intensity neutron source based upon the dense plasma focus. *AIP Conference Proceedings*, 1194(1):56–68, 2009.

[44] P. Silva, J. Moreno, L. Soto, L. Birstein, R.E. Mayer, and W. Kies. Neutron emission from a fast plasma focus of 400 joules. *Applied Physics Letters*, 83(16):3269–3271, 2003.

[45] B. L. Bures, M. Krishnan, and C. James. A plasma focus electronic neutron generator. *IEEE Transactions on Plasma Science*, 40(4):1082–1088, April 2012.

[46] R. Shukla, A. Shyam, R. Verma, E. Mishra, M. Meena, K. Sagar, and P. Dhang. Results of ultracompact plasma focus operating in repetitive burst-mode. *IEEE Transactions on Plasma Science*, 43(8):2354–2358, Aug 2015.

[47] P. Kubes, M. Paduch, M. J. Sadowski, J. Cikhardt, B. Cikhardtova, D. Klir, J. Kravarik, V. Munzar, K. Rezac, E. Zielinska, E. Skladnik-Sadowska, A. Szymaszek, K. Tomaszewski, and D. Zaloga. Characterization of fast deuterons involved in the production of fusion neutrons in a dense plasma focus. *PHYSICS OF PLASMAS*, 25(1), JAN 2018.

[48] J. Zebrowski, M.J. Sadowski, and L. Jakubowski. Correlation of neutron emission with other corpuscular and x-ray pulses in different plasma-focus experiments. In Sadowski, MJ and Dudeck, M and Hartfuss, HJ and Pawelec, E, editor, *PLASMA 2005*, volume 812 of *AIP Conference Proceedings*, pages 229+. Zarzad Wojewodztwa Opolskiego; Komitet Fizyki PAN; Uniwersytet Opolski, 2006. International Conference on Research and Applications of Plasmas (PLASMA 2005), Opole Univ, Opole Turawa, POLAND, SEP 06-09, 2005.

[49] L. Soto, C. Pavez, A. Tarifeno, J. Moreno, and F. Veloso. Studies on scalability and scaling laws for the plasma focus: similarities and differences in devices from 1 MJ to 0.1 J. *Plasma Sources Science and Technology*, 19(5):055017, 2010.

[50] E.J. Lerner, S.K. Murali, D. Shannon, A.M. Blake, and F. Van Roessel. Fusion reactions from ¿ 150 keV ions in a dense plasma focus plasmoid. *PHYSICS OF PLASMAS*, 19(3), MAR 2012.

[51] S.L. Jackson, J.T. Engelbrecht, A.S. Richardson, A. Beresnyak, B.V. Weber, J.L. Giuliani, I.M. Rittersdorf, J.W. Schumer, D. Klir, K. Rezac, J. Cikhardt,

Y. Maron, E. Stambulchik, and J W. Luginsland. Initial results from a dense plasma focus driven by a high-inductance generator. The 45th IEEE International Conference on Plasma Science (ICOPS 2018) will be held from June 24-28, 2018 in Denver, CO, USA., 2018.

[52] E. Huttener. The bomb without the boom. *1663, Los Alamos Scienece and Technology Magazine*, pages 18–25, October 2017.

[53] T. A. Mehlhorn. National security research in plasma physics and pulsed power: Past, present, and future. *IEEE Transactions on Plasma Science*, 42(5):1088–1117, May 2014.

[54] The Comprehensive Nuclear-Test-Ban Treaty websites. `https://www.ctbto.org/`, 2018.

[55] R.T. Olson, T.E. Beller, M. Boswell, T.E. Cutler, A. DeYoung, D.R. Dinwiddie, T.M. Dugan, M.M. Fowler, J.A. Gomez, and et al J.T. Goorley. Primary assessment technologies fy2017 milestone report: Ndse development using dpf. Technical report, Los Alamos National Lab.(LANL), Los Alamos, NM (United States), 2018.

[56] V. Yuan, M. Boswell, A. DeYoung, M.M. Fowler, J.T. Goorley, R.M. Malone, G.L. Morgan, A. Obst, and R.S. Rundberg. (u) detector systems and data analysis for ndse experiments at the dense plasma focus (dpf). Technical report, Los Alamos National Lab.(LANL), Los Alamos, NM (United States), 2018.

[57] C. Hagen. Dense plasma focus fusion neutron sources progress at nstec. `https://www.ctbto.org/`, July 2011.

[58] C. Hagen, D. Lowe, F. Cverna, S. Goldstein, and D. Pacheco. Pulsed Neutron Capabilities Developed for Experiments at Nevada National Security Site. *Stockpile Stewardship Quarterly*, 4(3):10–13, 2014.

[59] H. A. Bender. Site-directed research and development fy 2014 annual report. 4 2015.

[60] F.E. Merrill. Neutron radiography of thick dynamic systems. 6 2013.

[61] Specialised imaging, simx - ultra high speed framing camera. `http://specialised-imaging.com/products/simx-ultra-high-speed-framing-camera`.

[62] B. A. Remington, R. P. Drake, and D. D. Ryutov. Experimental astrophysics with high power lasers and z pinches. *Rev. Mod. Phys.*, 78:755–807, Aug 2006.

[63] J. Kane, D. Arnett, B. A. Remington, S. G. Glendinning, J. Castor, R. Wallace, A. Rubenchik, and B. A. Fryxell. Supernova-relevant hydrodynamic instability experiments on the nova laser. *The Astrophysical Journal Letters*, 478(2):L75, 1997.

[64] V. S. Beskin, Ya. N. Istomin, A. M. Kiselev, V. I. Krauz, K. N. Mitrofanov, V. V. Myalton, E. E. Nokhrina, D. N. Sob'yanin, and A. M. Kharrasov. Simulation of nonrelativistic jet ejections during the laboratory studies. *Radiophysics and Quantum Electronics*, 59(11):900–910, Apr 2017.

[65] V.I. Krauz. Poslednie dostizheniya v issledovaniyah i primenenii plazmennogo fokusa. *XXXIV International Conferention on Plasma Physics and Controlled Termonuclear Fusion*, 2007.

[66] K. N. Mitrofanov, V. I. Krauz, V. V. Myalton, V. P. Vinogradov, A. M. Kharrasov, and Yu. V. Vinogradova. Properties of the distribution of azimuthal magnetic field in a plasma flow during laboratory simulations of astrophysical jets in a plasma-focus installation. *Astronomy Reports*, 61(2):138–152, Feb 2017.

[67] D. Ryutov, R. P. Drake, J. Kane, E. Liang, B. A. Remington, and W. M. Wood-Vasey. Similarity criteria for the laboratory simulation of supernova hydrodynamics. *The Astrophysical Journal*, 518(2):821, 1999.

[68] G. Chabrier, D. Saumon, and C. Winisdoerffer. Hydrogen and helium at high density and astrophysical implications. *Astrophysics and Space Science*, 307(1):263–267, Jan 2007.

[69] V. S. Beskin. Magnetohydrodynamic models of astrophysical jets. *Physics-Uspekhi*, 53(12):1199, 2010.

[70] Lebedev S. V., editor. *High Energy Density Laboratory Astrophysics*. Springer, 2007.

[71] S. S. Ananyev, S. A. Dan'ko, and Yu. G. Kalinin. A spectroscopic complex for time-resolved registration of plasma-jet parameters at the pf-3 facility. *Instruments and Experimental Techniques*, 59(6):810–815, Nov 2016.

[72] S. S. Ananyev, S. A. Dan'ko, V. V. Myalton, A. I. Zhuzhunashvili, Yu. G. Kalinin, V. I. Krauz, M. S. Ladygina, and A. K. Marchenko. Spectroscopic measurements of the parameters of the helium plasma jets generated in the plasma focus discharge at the pf-3 facility. *Plasma Physics Reports*, 42(3):269–277, Mar 2016.

[73] K. N. Mitrofanov, V. I. Krauz, E. V. Grabovski, V. V. Myalton, M. Paduch, and A. N. Gritsuk. Features of the application of the magnetic-probe method for diagnostics of high-temperature plasma. *Instruments and Experimental Techniques*, 61(2):239–259, Mar 2018.

[74] I. Yu. Kalashnikov, V. I. Krauz, and V. M. Chechetkin. The mathematical model of an astrophysical jet simulation by the laboratory facility "plasma focus". *Journal of Physics: Conference Series*, 798(1):012008, 2017.

[75] D. A. Voitenko, S. S. Ananyev, G. I. Astapenko, A. D. Basilaia, A. I. Markolia, K. N. Mitrofanov, V. V. Myalton, A. P. Timoshenko, A. M. Kharrasov, and V. I. Krauz. Study of plasma flows generated in plasma focus discharge in different regimes of working gas filling. *Plasma Physics Reports*, 43(12):1132–1146, Dec 2017.

[76] V. I. Tereshin. Quasi-stationary plasma accelerators (qspa) and their applications. *Plasma Physics and Controlled Fusion*, 37(11A):A177, 1995.

[77] D.G. Solyakov. High-power plasma dynamic systems of quasi-stationary type in ipp nsk kipt: results and prospects. (1):104–109, 2015.

[78] I.E. Garkusha, V.A. Makhlaj, N.N. Aksenov, O.V. Byrka, S.V. Malykhin, A.T. Pugachov, B. Bazylev, I. Landman, G. Pinsuk, J. Linke, M. Wirtz, M.J. Sadowski, and E. Skladnik-Sadowska. High power plasma interaction with

tungsten grades in iter relevant conditions. *Journal of Physics: Conference Series*, 591(1):012030, 2015.

[79] I.E. Garkusha, N.N. Aksenov, O.V. Byrka, V.A. Makhlaj, S.S. Herashchenko, S.V. Malykhin, Yu.V. Petrov, V.V. Staltsov, S.V. Surovitskiy, M. Wirtz, J. Linke, M.J. Sadowski, and E. Skladnik-Sadowska. Simulation of plasma–surface interactions in a fusion reactor by means of qspa plasma streams: recent results and prospects. *Physica Scripta*, 91(9):094001, 2016.

[80] I.E. Garkusha, V.V. Chebotarev, S.S. Herashchenko, V.A. Makhlaj, N.V. Kulik, M.S. Ladygina, A.K. Marchenko, Yu.V. Petrov, V.V. Staltsov, P.V. Shevchuk, D.G. Solyakov, and D.V. Yelisyeyev. Novel test-bed facility for psi issues in fusion reactor conditions on the base of next generation qspa plasma accelerator. *Nuclear Fusion*, 57(11):116011, 2017.

[81] R.S. Rawat, V. Aggarwal, M. Hassan, P. Lee, S.V. Springham, T.L. Tan, and S. Lee. Nano-phase titanium dioxide thin film deposited by repetitive plasma focus: Ion irradiation and annealing based phase transformation and agglomeration. *Applied Surface Science*, 255(5, Part 2):2932 – 2941, 2008.

[82] Chhaya R. Kant, M.P. Srivastava, and R.S. Rawat. Thin carbon film deposition using energetic ions of a dense plasma focus. *Physics Letters A*, 226(3):212 – 216, 1997.

[83] M.T. Hosseinnejad, M. Ghoranneviss, G.R. Etaati, M. Shirazi, and Z. Ghorannevis. Deposition of tungsten nitride thin films by plasma focus device at different axial and angular positions. *Applied Surface Science*, 257(17):7653 – 7658, 2011.

[84] R.S. Rawat, T. Zhang, K.S. Thomas Gan, P. Lee, and R.V. Ramanujan. Nanostructured fe thin film deposition using plasma focus device. *Applied Surface Science*, 253(3):1611 – 1615, 2006.

[85] A. Buffler. Contraband detection with fast neutrons. *Radiation Physics and Chemistry*, 71(3):853 – 861, 2004. 9th International Symposium on Radiation Physics (ISRP-9).

[86] G. Vourvopoulos. Accelerator based techniques for contraband detection. *Nuclear Instruments and Methods in Physics Research Section B: Beam Interactions with Materials and Atoms*, 89(1):388 – 393, 1994.

[87] E.M.A. Hussein and E.J. Waller. Review of one-side approaches to radiographic imaging for detection of explosives and narcotics. *Radiation Measurements*, 29(6):581 – 591, 1998.

[88] C. Bruschini. Commercial systems for the direct detection of explosives for explosive ordnance disposal tasks. *Subsurface Sensing Technologies and Applications*, 2(3):299–336, Jul 2001.

[89] V.A. Gribkov, S.V. Latyshev, R.A. Miklaszewski, M. Chernyshova, K. Drozdowicz, U. Wiacek, K. Tomaszewski, and B.D. Lemeshko. A dense plasma focus-based neutron source for a single-shot detection of illicit materials and explosives by a nanosecond neutron pulse. *Physica Scripta*, 81(3):035502, 2010.

[90] A.A. Kaloyan, E.S. Kovalenko, A.V. Pakhnevich, and K.M. Podurets. The contrast scale of minerals for neutron tomography of paleontologic and geologic objects. *Russian Geology and Geophysics*, 58(11):1435 – 1440, 2017.

[91] J. Vlassenbroeck, V. Cnudde, B. Masschaele, M. Dierick, L. van Hoorebeke, and P. Jacobs. A comparative and critical study of x-ray ct and neutron ct as non-destructive material evaluation techniques. *Geological Society, London, Special Publications*, 271(1):277–285, 2007.

[92] S. Jednorog, A. Szydlowski, B. Bienkowska, and R. Prokopowicz. The application of selected radionuclides for monitoring of the d-d reactions produced by dense plasma-focus device. *Journal of Radioanalytical and Nuclear Chemistry*, 301:23–31, 2014.

[93] C. A. Coverdale, C. Deeney, A. L. Velikovich, R. W. Clark, Y. K. Chong, J. Davis, J. Chittenden, C. L. Ruiz, G. W. Cooper, A. J. Nelson, J. Franklin, P. D. LePell, J. P. Apruzese, J. Levine, J. Banister, and N. Qi. Neutron production and implosion characteristics of a deuterium gas-puff z pinch. *Physics of Plasmas*, 14(2):022706, 2007.

[94] T. Clayson, S. V. Lebedev, F. Suzuki-Vidal, G. C. Burdiak, J. W. D. Halliday, J. D. Hare, J. Ma, L. G. Suttle, and E. R. Tubman. Inverse liner z-pinch: An experimental pulsed power platform for studying radiative shocks. *IEEE Transactions on Plasma Science*, pages 1–7, 2018.

[95] P. W. L. de Grouchy, B. R. Kusse, J. Banasek, J. Engelbrecht, D. A. Hammer, N. Qi, S. Rocco, and S. N. Bland. Observations of the magneto-rayleigh-taylor instability and shock dynamics in gas-puff z-pinch experiments. *Physics of Plasmas*, 25(7):072701, 2018.

[96] S. Rocco, J. Banasek, W. Potter, B. Kusse, D. Hammer, and N. Qi. Instabilities and the implosion dynamics of gas-puff z-pinch experiments*. In *2017 IEEE International Conference on Plasma Science (ICOPS)*, May 2017.

[97] T. J. Awe, R. D. McBride, C. A. Jennings, D. C. Lamppa, M. R. Martin, D. C. Rovang, S. A. Slutz, M. E. Cuneo, A. C. Owen, D. B. Sinars, K. Tomlinson, M. R. Gomez, S. B. Hansen, M. C. Herrmann, J. L. McKenney, C. Nakhleh, G. K. Robertson, G. A. Rochau, M. E. Savage, D. G. Schroen, and W. A. Stygar. Observations of modified three-dimensional instability structure for imploding z-pinch liners that are premagnetized with an axial field. *Phys. Rev. Lett.*, 111:235005, Dec 2013.

[98] T. J. Awe, C. A. Jennings, R. D. McBride, M. E. Cuneo, D. C. Lamppa, M. R. Martin, D. C. Rovang, D. B. Sinars, S. A. Slutz, A. C. Owen, K. Tomlinson, M. R. Gomez, S. B. Hansen, M. C. Herrmann, M. C. Jones, J. L. McKenney, G. K. Robertson, G. A. Rochau, M. E. Savage, D. G. Schroen, and W. A. Stygar. Modified helix-like instability structure on imploding z-pinch liners that are pre-imposed with a uniform axial magnetic field. *Physics of Plasmas*, 21(5):056303, 2014.

[99] M.E. Cuneo, M.C. Herrmann, D.B. Sinars, S.A. Slutz, W.A. Stygar, .R.A Vesey, A.B. Sefkow, G.A. Rochau, G.A. Chandler, J.E. Bailey, et al. Magnetically driven implosions for inertial confinement fusion at sandia national laboratories. *IEEE Transactions on Plasma Science*, 40(12):3222–3245, 2012.

[100] D. Klir, P. Kubes, K. Rezac, J. Cikhardt, J. Kravarik, O. Sila, A. V. Shishlov, B. M. Kovalchuk, N. A. Ratakhin, V. A. Kokshenev, A. Yu. Labetsky, R. K.

Cherdizov, F. I. Fursov, N. E. Kurmaev, G. N. Dudkin, B. A. Nechaev, V. N. Padalko, H. Orcikova, and K. Turek. Efficient neutron production from a novel configuration of deuterium gas-puff z-pinch. *Phys. Rev. Lett.*, 112:095001, Mar 2014.

[101] D. Klir, A. V. Shishlov, V. A. Kokshenev, P. Kubes, A. Yu Labetsky, K. Rezac, R. K. Cherdizov, J. Cikhardt, B. Cikhardtova, G. N. Dudkin, F. I. Fursov, A. A. Garapatsky, B. M. Kovalchuk, J. Kravarik, N. E. Kurmaev, H. Orcikova, V. N. Padalko, N. A. Ratakhin, O. Sila, K. Turek, and V. A. Varlachev. Efficient generation of fast neutrons by magnetized deuterons in an optimized deuterium gas-puff z-pinch. *Plasma Phys. Control. Fusion*, 57(4), APR 2015.

[102] D. Klir, A.V. Shishlov, V.A. Kokshenev, P. Kubes, A.Yu. Labetsky, K. Rezac, R. Cherdizov, J. Cikhardt, B. Cikhardtova, G. N. Dudkin, F. I. Fursov, A. A. Garapatsky, B.M. Kovalchuk, J. Krása, J. Kravarik, N.E. Kurmaev, H. Orcikova, V. N. Padalko, N. A. Ratakhin, O. Sila, K. Turek, V.A. Varlachev, A. Velyhan, and R. Wagner. Deuterium z-pinch as a powerful source of multi-mev ions and neutrons for advanced applications. *Physics of Plasmas*, 23(032702), 2016.

[103] D. Klir, A. Shishlov, V, V. A. Kokshenev, P. Kubes, K. Rezac, R. K. Cherdizov, J. Cikhardt, B. Cikhardtova, G. N. Dudkin, F. Fursov, I, T. Hyhlik, J. Kaufman, B. M. Kovalchuk, J. Krasa, J. Kravarik, N. E. Kurmaev, A. Yu Labetsky, V Munzar, H. Orcikova, V. N. Padalko, N. A. Ratakhin, O. Sila, J. Stodulka, K. Turek, V. A. Varlachev, and R. Wagner. Ion acceleration mechanism in mega-ampere gas-puff z-pinches. *NEW JOURNAL OF PHYSICS*, 20, MAY 31 2018.

[104] V. Munzar, D. Klir, J. Cikhardt, B. Cikhardtova, J. Kravarik, P. Kubes, and K. Rezac. Investigation of magnetic fields in z-pinches via multi-mev proton deflectometry. *IEEE Transactions on Plasma Science*, pages 1–10, 2018.

[105] A. Beresnyak, J. L. Giuliani, S. L. Jackson, A. S. Richardson, S. Swanekamp, J. Schumer, B. Weber, and D. Mosher. Simulations of a dense plasma focus on a high-impedance generator. *IEEE Transactions on Plasma Science*, pages 1–5, 2018.

[106] M. Scholz, R. Miklaszewski, M. Paduch, M.J. Sadowski, A. Szydlowski, and K. Tomaszewski. Preliminary neutron experiments with the pf-1000 plasma-focus facility. *IEEE transactions on plasma science*, 30(2):476–481, 2002.

[107] A.E. Gurei, V.Ya. Nikulin, S.N. Polukhin, I.V. Volobuev, J.A. Kakutina, and L.A. Dushina, June 2011.

[108] A Cicuttin, ML Crespo, VA Gribkov, J Niemela, C Tuniz, C Zanolli, M Chernyshova, EV Demina, SV Latyshev, VN Pimenov, et al. Experimental results on the irradiation of nuclear fusion relevant materials at the dense plasma focus 'Bora'device. *Nuclear Fusion*, 55(6):063037, 2015.

[109] V.Ya. Nikulin, L.I. Ivanov, G.N. Mikhailova, B.P. Mikhailov, O.N. Krokhin, A.V. Troitskii, E.I. Demikhov, L.Kh. Antonova, I.V. Borovitskaja, P.V. Gorshkov, E.N. Peregudova, S.V. Poicrovskij, I.A. Rudnev, L.A. Dushina, and J.A. Kakutina, June 2011.

[110] P Kubes, D Klir, J Kravarik, E Litseva, and K Rezac. Research of the small plasma focus with an auxiliary electrode at deuterium filling. *Plasma physics reports*, 35(10):824, 2009.

[111] M. Scholz, J. Bielecki, A. Wojcik-Gargula, U. Wiacek, K. Drozdowicz, A. Igielski, A. Kulinska, G. Tracz, U. Woznicka, J. Dankowski, B. Gabanska, A. Igielski, and A. Kurowski. Research of plasma and material's interaction at Tallinn University. `http://www.icdmp.pl/images/2016/Laas.pdf`, October 2016.

[112] C. Deeney, M. R. Douglas, R. B. Spielman, T. J. Nash, D. L. Peterson, P. L'Eplattenier, G. A. Chandler, J. F. Seamen, and K. W. Struve. Enhancement of X-ray Power from a Z Pinch Using Nested-Wire Arrays. *Phycal Review Letters*, 81(22):4883–4886, NOV 1998.

[113] S.P. Bugaev, A.M. Volkov, A.A. Kim, V.N. Kiselev, B.M. Koval'chuk, N.F. Kovsharov, V.A. Kokshenev, N.E. Kurmaev, S.V. Loginov, G.A. Mesyats, F.I. Fursov, and A.P. Khuzeev. GIT16: A megajoule pulse generator with plasma switch for a Z-pinch load. *Russian Physics Journal*, 40(12):1154–1161, 1997.

[114] David L Smith, Mark E Savage, Gerold R Ziska, and Robert L Starbird. Zr marx capacitor vendor evaluation and lifetime test results. *IEEE transactions on plasma science*, 33(4):1273–1281, 2005.

[115] B Stoltzfus, K LeChien, M Savage, and W Stygar. High voltage insulator improvements made in the oil and water sections of the z machine at sandia national laboratories in 2008. In *Pulsed Power Conference, 2009. PPC'09. IEEE*, pages 425–430. IEEE, 2009.

[116] JH Degnan, WL Baker, KE Hackett, DJ Hall, JL Holmes, JB Kriebel, DW Price, RE Reinovsky, JD Graham, EA Lopez, et al. Experimental results from shiva star vacuum inductive store/plasma flow switch drven implosions. *IEEE transactions on plasma science*, 15(6):760–765, 1987.

[117] J. Deng, W. Xie, S. Feng, M. Wang, H. Li, S. Song, M. Xia, A. He, Q. Tian, Y. Gu, et al. Initial performance of the primary test stand. *IEEE Transactions on Plasma Science*, 41(10):2580–2583, 2013.

[118] Jianjun Deng, Jinshui Shi, Weiping Xie, Linwen Zhang, Suping Feng, Jin Li, Meng Wang, Lianshen Xia, Zhiyong Dai, Hongtao Li, et al. Overview of pulsed power researches at caep. In *Plasma Sciences (ICOPS) held with 2014 IEEE International Conference on High-Power Particle Beams (BEAMS), 2014 IEEE 41st International Conference on*, pages 1–6. IEEE, 2014.

[119] F Lassalle, C Mangeant, B Roques, A Georges, A Loyen, JF Cambonie, S Laspalles, D Cadars, G Rodriguez, JM Delchie, et al. Reliability and performances improvements of the sphinx machine based on the 1 microsecond ltd technology. In *14th Symp. on High Current Electronics, Tomsk*. Citeseer, 2006.

[120] H Calamy, F Lassalle, A Loyen, F Zucchini, JP Chittenden, F Hamann, P Maury, A Georges, JP Bedoch, and A Morell. Use of microsecond current prepulse for dramatic improvements of wire array z-pinch implosion. *Physics of Plasmas*, 15(1):012701, 2008.

[121] Juan J Ramirez, KR Prestwich, DL Johnson, JP Corley, GJ Denison, JA Alexander, TL Franklin, PJ Pankuch, TWL Sanford, TJ Sheridan, et al. Performance of the hermes-iii gamma ray simulator. In *Pulsed Power Conference, 1989. 7th*, pages 26–31. IEEE, 1989.

[122] Z. A. Albikov, E. P. Velikhov, A. I. Veretennikov, V. A. Glukhin, E. V. Grabovski, G. M. Gryaznov, O. A. Gusev, G. N. Zhemchuznikov, V. I. Zaitsev, O. A. Zolotoskii, Yu. A. Istomin, O. V. Kozlov, I. S. Krashneninnikov, S. S. Kurochkin, G. M. Latmanizova, V. V. Matveev, G. V. Mineev, V. N. Mikhailov, S. L. Nedoseev, G. M. Oleinik, V. P. Pevchev, A. S. Perlin, O. P. Pecherskii, V. D. Piśmennyi, L. I. Rudakov, V. P. Smirnov, V. Ya. Tsarfin, I. R. Yampolskii. Angara-5-1 experimental complex. *Atomic Energy*, 68(1):26–35, January 1990.

[123] RB Spielman, RJ Dukart, DL Hanson, BA Hammel, WW Hsing, MK Matzen, and JL Porter. Z-pinch experiments on saturn at 30 tw. In *AIP Conference Proceedings CONF- 8904107*, volume 195, pages 3–16. AIP, 1989.

[124] RJ Allen, PF Ottinger, RJ Commisso, JW Schumer, TA Holt, P Hoppe, I Smith, and DL Johnson. Electrical modeling of mercury for optimal machine design and performance estimation. In *Pulsed Power Conference, 2003. Digest of Technical Papers. PPC-2003. 14th IEEE International*, volume 2, pages 887–890. IEEE, 2003.

[125] AV Luchinskii, Nikolay Alexadrovich Ratakhin, VF Fedushchak, and AN Shepelev. Multipurpose transformer-type pulse generator. *Russian physics journal*, 40(12):1178–1184, 1997.

[126] IH Mitchell, JM Bayley, JP Chittenden, JF Worley, AE Dangor, MG Haines, and P Choi. A high impedance mega-ampere generator for fiber z-pinch experiments. *Review of Scientific Instruments*, 67(4):1533–1541, 1996.

[127] Ph Romary, P Eyl, and JM Angles. Performances of ambiorix [pulsed power generator]. In *Pulsed Power Conference, 1995. Digest of Technical Papers., Tenth IEEE International*, volume 2, pages 1074–1079. IEEE, 1995.

[128] Xu Rong-Kun, Li Zheng-Hong, Yang Jian-Lun, Xu Ze-Ping, Ding Ning, Guo Cun, Jiang Shi-Lun, Ning Jia-Ming, Xia Guang-Xin, Li Lin-Bo, et al. Study of tungsten wire array z-pinch implosion on qiang-guang i facility. *Chinese Physics*, 14(8):1613, 2005.

[129] LS Levine and IM Vitkovitsky. Pulsed power technology for controlled thermonuclear fusion. *IEEE Transactions on Nuclear Science*, 18(4):255–264, 1971.

[130] Victor L Kantsyrev, Alla S Safronova, Dmitry A Fedin, Vladimir V Ivanov, Andrey A Esaulov, Vidya Nalajala, Ishor Shrestha, Shivaji Pokala, Kenneth Williamson, Nicholas D Ouart, et al. Radiation properties and implosion dynamics of planar and cylindrical wire arrays, asymmetric and symmetric, uniform and combined x-pinches on the unr 1-ma zebra generator. *IEEE transactions on plasma science*, 34(2):194–212, 2006.

[131] Alexandre S Chuvatin, Viktor L Kantsyrev, Leonid I Rudakov, Michael E Cuneo, AL Astanovitskiy, Radu Presura, Alla S Safronova, W Cline, Kenneth M Williamson, Ishor Shrestha, et al. Operation of a load current multiplier on a nanosecond mega-ampere pulse forming line generator. *Physical Review Special Topics-Accelerators and Beams*, 13(1):010401, 2010.

[132] Cornell University Laboratory of Plasma Studies Websites. `https://www.lps.cornell.edu/project/cobra/`, 2018.

[133] Guiji Wang, Binqiang Luo, Xuping Zhang, Jianheng Zhao, Chengwei Sun, Fuli Tan, Tao Chong, Jianjun Mo, Gang Wu, and Yanhui Tao. A 4 ma, 500 ns pulsed power generator cq-4 for characterization of material behaviors under ramp wave loading. *Review of Scientific Instruments*, 84(1):015117, 2013.

[134] Guiji Wang, Xuemiao Chen, Jintao Cai, Xuping Zhang, Tao Chong, Binqiang Luo, Jianheng Zhao, Chengwei Sun, Fuli Tan, Cangli Liu, et al. A high current pulsed power generator cq-3-mmaf with co-axial cable transmitting energy for material dynamics experiments. *Review of Scientific Instruments*, 87(6):065110, 2016.

[135] Boris Mikhaylovich Kovalchuk, AV Kharlov, VN Kiselev, EV Kumpyak, VB Zorin, VV Chupin, and AV Morozov. Mega-ampere submicrosecond generator git-32. *Review of scientific instruments*, 78(3):033501, 2007.

[136] Plasma Laboratory - Weizmann Institute of Science Websites. `http://plasma-gate.weizmann.ac.il/projects/experiments/z-pinch/`, 2018.

[137] PC Campbell, JM Woolstrum, F Antoulinakis, TM Jones, DA Yager-Elorriaga, SM Miller, Nicholas M Jordan, YY Lau, Ronald M Gilgenbach, and Ryan D McBride. Diagnostic and power feed upgrades to the maize facility. *IEEE Transactions on Plasma Science*, (99):1–9, 2018.

[138] M. Scholz, J. Bielecki, A. Wojcik-Gargula, U. Wiacek, K. Drozdowicz, A. Igielski, A. Kulinska, G. Tracz, U. Woznicka, J. Dankowski, B. Gabanska, A. Igielski, and A. Kurowski. The plasma-focus device at ifj krakow. `http://www.icdmp.pl/images/2015/Scholz_ICDMP%2015.pdf`, September 2015.

[139] D.R. Zaloga. *Badania emisji promieniowania widzialnego i rentgenowskiego oraz oceny temperatury elektronowej w wyladowaniach typu Plasma-Focus.* PhD thesis, National Centre for Nuclear Research, Swierk, 2017.

[140] W.L. Baker, P.J. Turchi, and J.H. Degnan. 30 years of pulsed power rd in afrl kirtland's building 322. `https://en.wikipedia.org/wiki/Shiva_Star`, October 2003.

[141] E.V. Grabovski and V.V. Aleksandrov and V.A. Afanasyev and G.S. Volkov and A.N. Gribov and A.N. Gritsuk and N.I. Efremov and L.V. Zagryadski and V.I. Zaytsev and G.G. Zukakishvili, M.K. Krylov and Ya.N. Laukhin and A.P. Lototski and S.F. Medovshikov and K.N. Mitrofanov and S.L. Nedoseev and A.A. Nikolashin and G.M. Oleynik and I.Yu. Profeev and A.A. Samokhin and P.V. Sasorov and V.P. Smirnov and I.N. Frolov and M.V. Fedulov and G.N. Khomutinnikov. Issledovaniya Izluchayushikh Z-Pinchei i Proekt Baikal. `www.fpl.gpi.ru/Zvenigorod/XXXIV/R/ru/EV-Grabovskii.doc`, February 2007.

[142] Nuclear Weapons Engineering, Sandia National Laboratories Website. `https://www.sandia.gov/news/publications/lab_accomplishments/articles/2016/nuclear-weapons-engineering.html`.

[143] Bc-400,bc-404,bc-408,bc-412,bc-416 premium plastics scintillators data sheet. `http://www.crystals.saint-gobain.com/sites/imdf.crystals.com/files/documents/sgc-bc400-404-408-412-416-data-sheet.pdf`, 2016.

[144] Photomultiplier tubes r1828-01, r2059. `https://www.hamamatsu.com/resources/pdf/etd/R1828-01_R2059_TPMH1259E.pdf`, 2016.

[145] D Klir, J Kravarik, P Kubes, K Rezac, E Litseva, K Tomaszewski, L Karpinski, M Paduch, and M Scholz. Fusion neutron detector for time-of-flight measurements in z-pinch and plasma focus experiments. *Review of Scientific Instruments*, 82(3):033505, 2011.

[146] M. Vlad. A time resolving spectrometry method for particles emitted in intense bursts. *Nuclear Instruments and Methods in Physics Research*, 227:327–334, 1985.

[147] I. Tiseanu, G. Deckerb, and Kies W. A monte-carlo technique for the reconstruction of time dependent spectra of short-pulse neutron sources. *Nuclear Instruments and Methods in Physics Research A*, 373:73–80, 1996.

[148] K. Rezac. *Reconstruction of Neutron Energy Spectra in Z-pinch Fusion Experiments*. PhD thesis, Czech Technical University in Prague, Faculty of Electrical Engineering, 2011.

[149] K. Rezac, D. Klir, P Kubes, and J. Kravarik. Improvement of time-of-flight methods for reconstruction of neutron energy spectra from d(d,n)3he fusion reactions. *Plasma Phys. Control. Fusion*, 54, 2012.

[150] Nudat 2.6, national nuclear data center, brookhaven national laboratory. `http://www.nndc.bnl.gov/nudat2/chartNuc.jsp`.

[151] Hans-Joachim Kunze. *Introduction to plasma spectroscopy*, volume 56. Springer Science & Business Media, 2009.

[152] E Zielińska, M Paduch, and M Scholz. Sixteen-frame interferometer for a study of a pinch dynamics in pf-1000 device. *Contributions to Plasma Physics*, 51(2-3):279–283, 2011.

[153] M.I. Pergament. *Methods of Experimental Physics*. Graduate Student Series in Physics. Taylor & Francis, 2014.

[154] F.F. Chen. *Úvod do fyziky plazmatu*. Academia, Prague, 1984.

[155] A. Kasperczuk. *Badanie interferometryczne procesów powstawania i rozpadu sznura plazmowego w urzadzeniu plasma-focus PF-150*. PhD thesis, Military University of Technology in Warsaw, 1984.

[156] T. Chodukowski. *Badanie parametrów i dynamiki plazmy w urzadzeniu PF-1000 w fazach formowania i rozpadu kolumny plazmowej metoda wielokadrowej interferometrii laserowej.* PhD thesis, Instytut Fizyki Plazmy i Laserowej Mikrosyntezy, Warsaw, 2012.

[157] P. Kubeš. *Impulsní silnoproudé výboje a jejich diagnostika.* ČVUT FEL, Prague, Czech Republic, 2004.

[158] P Kubes, M Paduch, J Cikhardt, J Kortanek, B Cikhardtova, K Rezac, D Klir, J Kravarik, and E Zielinska. Filamentary structure of plasma produced by compression of puffing deuterium by deuterium or neon plasma sheath on plasma-focus discharge. *Physics of Plasmas*, 21(12):122706, 2014.

[159] J. Cikhardt. Elektromagnetický ventil pro napouštění plynu a jeho testování. Master's thesis, Bachelor thesis, Czech Technical University in Prague, 2010.

[160] D. Klir, J. Kravarik, P. Kubes, K. Rezac, J. Cikhardt, E. Litseva, T. Hyhlik, S. S. Ananev, Yu L. Bakshaev, V. A. Bryzgunov, A. S. Chernenko, Yu G. Kalinin, E. D. Kazakov, V. D. Korolev, G. I. Ustroev, A. A. Zelenin, L. Juha, J. Krasa, A. Velyhan, L. Vysin, J. Sonsky, and I. V. Volobuev. Efficient Production of 100 keV Deuterons in Deuterium Gas Puff Z-pinches at 2 MA Current. *Plasma Physics and Controlled Fusion*, 52(6), JUN 2010.

[161] B. Cikhardtova, P. Kubes, J. Cikhardt, M. Paduch, E. Zielinska, J. Kravarik, K. Rezac, J. Kortanek, and O. Sila. Temporal distribution of linear densities of the plasma column in a plasma focus discharge. *Nukleonika*, 60(2):315–318, 2015.

[162] B. Cikhardtova, P. Kubes, J. Cikhardt, M. Paduch, E. Zielinska, J. Kravarik, K. Rezac, and J. Kortanek. Evolution of the small ball-like structures in the plasma focus discharge. *Nukleonika*, 61(2):155–159, 2016.

[163] P. Kubes, M. Paduch, J. Cikhardt, D.l Klir, K. Rezac, J. Kravarik, B. Cikhardtova, J. Kortanek, and E. Zielinska. Puffing deuterium compressed by a neon plasma sheath at the initial poloidal magnetic field in plasma focus discharge. *IEEE Transactions on Plasma Science*, 43(8):2532–2538, 2015.

[164] P. Kubes, M. Paduch, J. Cikhardt, D. Klir, J. Kravarik, K. Rezac, J. Kortanek, B.. Cikhardtova, and E. Zielinska. Existence of a return direction for plasma escaping from a pinched column in a plasma focus discharge. *Physics of Plasmas*, 22(5):052706, 2015.

[165] P. Kubes, M. Paduch, J. Cikhardt, D. Klir, J. Kravarik, K.. Rezac, B Cikhardtova, J. Kortanek, and E. Zielinska. The evolution of the plasmoidal structure in the pinched column in plasma focus discharge. *Plasma Physics and Controlled Fusion*, 58(4):045005, 2016.

[166] P. Kubes, M. Paduch, B. Cikhardtova, J. Cikhardt, D. Klir, J. Kravarik, K. Rezac, J. Kortanek, E. Zielinska, M.J. Sadowski, et al. The influence of the nitrogen admixture on the evolution of a deuterium pinch column. *Physics of Plasmas*, 23(8):082704, 2016.

[167] P. Kubes, M. Paduch, J. Cikhardt, B. Cikhardtova, D. Klir, J. Kravarik, K. Rezac, E. Zielinska, M.J. Sadowski, A. Szymaszek, et al. Filamentation in the pinched column of the dense plasma focus. *Physics of Plasmas*, 24(3):032706, 2017.

[168] P. Kubes, M. Paduch, J. Cikhardt, B. Cikhardtova, D. Klir, J. Kravarik, K. Rezac, E. Zielinska, M.J. Sadowski, A. Szymaszek, et al. Transformation of the ordered internal structures during the acceleration of fast charged particles in a dense plasma focus. *Physics of Plasmas*, 24(7):072706, 2017.

[169] N. Bennett, M. Blasco, K. Breeding, D. Constantino, A. DeYoung, V. DiPuccio, J. Friedman, B. Gall, S. Gardner, J. Gatling, E. C. Hagen, A. Luttman, B. T. Meehan, M. Misch, S. Molnar, G. Morgan, R. O'Brien, L. Robbins, R. Rundberg, N. Sipe, D. R. Welch, and V. Yuan. Development of the dense plasma focus for short-pulse applications. *Physics of Plasmas*, 24(1):012702, 2017.

[170] P. Kubes, M. Paduch, J. Cikhardt, B. Cikhardtova, D. Klir, J. Kravarik, K. Rezac, E. Zielinska, M.J. Sadowski, A. Szymaszek, et al. Increase in the neutron yield from a dense plasma-focus experiment performed with a conical tip placed in the centre of the anode end. *Physics of Plasmas*, 24(9):092707, 2017.

[171] Dmitri D Ryutov. Characterizing the plasmas of dense z-pinches. *IEEE Transactions on Plasma Science*, 43(8):2363–2384, 2015.

[172] W. A. Stygar, T. J. Awe, J. E. Bailey, N. L. Bennett, E. W. Breden, E. M. Campbell, R. E. Clark, R. A. Cooper, M. E. Cuneo, J. B. Ennis, D. L. Fehl, T. C. Genoni, M. R. Gomez, G. W. Greiser, F. R. Gruner, M. C. Herrmann, B. T. Hutsel, C. A. Jennings, D. O. Jobe, B. M. Jones, M. C. Jones, P. A. Jones, P. F. Knapp, J. S. Lash, K. R. LeChien, J. J. Leckbee, R. J. Leeper, S. A. Lewis, F. W. Long, D. J. Lucero, E. A. Madrid, M. R. Martin, M. K. Matzen, M. G. Mazarakis, R. D. McBride, G. R. McKee, C. L. Miller, J. K. Moore, C. B. Mostrom, T. D. Mulville, K. J. Peterson, J. L. Porter, D. B. Reisman, G. A. Rochau, G. E. Rochau, D. V. Rose, D. C. Rovang, M. E. Savage, M. E. Sceiford, P. F. Schmit, R. F. Schneider, J. Schwarz, A. B. Sefkow, D. B. Sinars, S. A. Slutz, R. B. Spielman, B. S. Stoltzfus, C. Thoma, R. A. Vesey, P. E. Wakeland, D. R. Welch, M. L. Wisher, and J. R. Woodworth. Conceptual designs of two petawatt-class pulsed-power accelerators for high-energy-density-physics experiments. *Physical Review Special Topics-Accelerators and Beams*, 18(11), NOV 30 2015.